Alma Mater Studiorum – Università di Bologna

DOTTORATO DI RICERCA IN

Ingegneria Elettronica, Telecomunicazioni e Tecnologie dell'Informazione

Ciclo XXVI

Settore Concorsuale di afferenza: 09/F2

Settore Scientifico disciplinare: ING-INF/03

Code Synchronization and Interference Management techniques for Satellite Navigation and Communications

Presentata da: **Giulio Gabelli**

Coordinatore Dottorato	**Relatore**
Prof. Alessandro Vanelli-Coralli	**Prof. Giovanni E. Corazza**

Esame finale anno 2014

GIULIO GABELLI

CODE SYNCHRONIZATION AND INTERFERENCE MANAGEMENT TECHNIQUES FOR SATELLITE NAVIGATION AND COMMUNICATIONS

Ph.D. Programme in Electronics Engineering, Telecommunications and Information Technology - XXVI Cycle
Department of Electrical, Electronic and Information Engineering - DEI
Alma Mater Studiorum - Università di Bologna

CODE SYNCHRONIZATION AND INTERFERENCE MANAGEMENT TECHNIQUES FOR SATELLITE NAVIGATION AND COMMUNICATIONS

GIULIO GABELLI

Ph.D. Programme in Electronics Engineering, Telecommunications and Information Technology - XXVI Cycle

Coordinator: Prof. Alessandro Vanelli-Coralli
Supervisor: Prof. Giovanni E. Corazza

SC: 09/F2
SSD: ING-INF/03

Department of Electrical, Electronic and Information Engineering - DEI
Alma Mater Studiorum - Università di Bologna

March 2014

Giulio Gabelli: *Code Synchronization and Interference Management techniques for Satellite Navigation and Communications*, Department of Electrical, Electronic and Information Engineering - DEI, Alma Mater Studiorum - Università di Bologna, © March 2014

È da un mese che naviga a vuoto quell'Atlantico amaro,
ma continua a puntare l'ignoto con lo sguardo corsaro;
sarà forse un'assurda battaglia ma ignorare non puoi
che l'Assurdo ci sfida per spingerci ad essere fieri di noi.
— Francesco Guccini, *Cristoforo Colombo*

ABSTRACT

This thesis collects the outcomes of a Ph.D. course in Telecommunications engineering and it is focused on enabling techniques for Spread Spectrum (SS) navigation and communication satellite systems. It provides innovations for both interference management and code synchronization techniques. These two aspects are still very critical for modern navigation and communication systems and constitute the common denominator of the whole work.

The thesis is organized in two parts: the former deals with interference management. In particular, we have proposed a novel technique for the enhancement of the sensitivity level of an advanced interference detection and localization system operating in the Global Navigation Satellite System (GNSS) bands, which allows the identification of interfering signals received with power even lower than the GNSS signals. Moreover, we have introduced an effective cancellation technique for signals transmitted by jammers, exploiting their particular repetitive characteristics, which strongly reduces the interference level at the receiver.

The second part, deals with code synchronization. More in details, we have designed the code synchronization circuit for a Telemetry, Tracking and Control (TT&C) system operating during the Launch and Early Orbit Phase (LEOP); the proposed solution allows to cope with the very large frequency uncertainty and dynamics characterizing this scenario, and performs the estimation of the code epoch, of the carrier frequency and of the carrier frequency variation rate. Furthermore, considering a generic pair of circuits performing code acquisition, we have proposed a comprehensive framework for the design and the analysis of the optimal cooperation procedure, which minimizes the time required to accomplish the synchronization. The study results particularly interesting since it leads to solutions to reduce the time needed to perform code acquisition without increasing the computational complexity. Finally, considering a network of collaborating navigation receivers, we have proposed an innovative cooperative code acquisition scheme, which allows exploit the shared code epoch information between neighbor nodes, according to the Peer-to-Peer (P2P) paradigm.

INTRODUCTION

In March 1903, Nikola Tesla was granted a patent for a system envisaging frequency hopping between two or more channels. He had the idea after presenting a radio controlled robot boat, when it became clear that the control signals needed to be protected against any disturbance. In order to prevent communications with the boat being disrupted, he proposed a signaling system whereby transmitter and receiver are synchronized and hop between different channels by altering the carrier frequency in a predetermined sequence to avoid disturbance: this was the first example of Spread Spectrum. During the years, SS transmissions proved their effectiveness for multiple functions: they have been used in order to allow multiple access, to carry timing information, to decrease potential interference and to achieve privacy. Different spreading techniques have been introduced: frequency-hopping SS, direct-sequence SS, time-hopping SS, chirp SS, and combinations of these techniques are forms of spread spectrum.

Nowadays, SS is a consolidated asset for satellite navigation and communication systems. Accordingly, even though it has been a well-investigated topic for many years, important research activities are being carried out in order to face with the new challenges raised by the recent development of the GNSSs and of the systems that use the navigation services, and by the introduction of novel concepts in the satellite communication area.

As a matter of fact, on the one hand, the wide adoption of the GNSS has made their reliability and robustness a mandatory requirement which needs to be guaranteed. Since satellite navigation signals are very weak signals, they are relatively vulnerable to interference, which can cause reduced accuracy, or even the complete inability of the receiver to calculate position; at the same time, applications increasingly rely on the localization and timing services provided by the GNSS, therefore a denial of service could be harmful for many human activities. The scientific community has recognized that interference is and will be a main threat to satellite navigation, and nowadays a multitude of activities are being carried out in order to develop countermeasures.

On the other hand, the development of the satellite technologies and of the terrestrial equipments has raised new challenges for the signal processing community, also in the field of code synchronization. Brand new synchronization strategies have to be designed when taking into account the adoption of SS transmissions in different communication systems, like for TT&C systems operating in LEOP, the modernization of the satellite signal structures (which foresee hierarchical codes, and multiple open signals present on the same band), and the advancements of the receiver capabilities.

In summary, SS systems still present open challenges due to the wide application arena and to the growing technological develop-

ments. In this dissertation we present the advancements and the results of the research carried out during my Ph.D. activity, in the context of interference management and code synchronization for satellite navigation and communication systems. An interesting aspect of this activity is that it has been characterized by the continuous interaction with industrial partners within the framework of international research projects [Pr2] [Pr1] [Pr4] [Pr3] [Pr5]. Most of the results presented in this dissertation are the solutions to the problems encountered within the aforementioned projects. The interaction with industrial partners has allowed the identification of the requirement and of the trade-offs due to practical implementation, and has provided the proof of the applicability of the designed solutions.

ORIGINAL CONTRIBUTIONS

In this dissertation, innovative techniques and methodologies aimed to enhance the performance and availability of the satellite SS systems are presented. The main contributions of this thesis are in the context of interference management and of code synchronization.

The countermeasures adopted in order to limit the problems due to interference, usually consist of detection and localization systems. In the context of project [Pr5], we have introduced a novel algorithm which is able to strongly enhance the sensitivity of a detection and localization system, enabling the detection/localization of signals received with a power lower than the navigation signals, leading to performance similar to the GNSS free case. Results of the analysis carried out, and the description of the algorithm design are presented in [P1], [P2] and [P3].

Furthermore, working within the framework of the DETECTOR project [Pr1], we have proposed a completely new approach for interference mitigation. The classic mitigation methods present in the literature are usually targeted for a small subset of interference signals. Exploiting the results of recent measurement campaigns, which have put in evidence that most of the interfering signals present quasi-periodic characteristics, a comprehensive cancellation algorithm has been introduced. The design of the algorithm and the results obtained for synthesized and actual signals are presented in [P4].

On the other hand, regarding code synchronization, we have designed a novel code synchronization algorithm able to perform the estimation of code epoch, carrier frequency and of its variation rate. The designed solution has been developed within the framework of a European project [Pr2], and it is intended for next generation TT&C systems operating during the LEOP phase, a scenario in which classic code acquisition approaches are not suitable. The design and the results have been published in [P5].

Furthermore, we have developed a comprehensive framework for the design and analysis of the code synchronization procedure for complex systems, consisting of pairs of acquisition circuits. As a matter of fact, the problem of pairs of Finite State Machines (FSMs) per-

forming code acquisition is often encountered. The study provides the means to optimize the overall mean acquisition time of pairs of circuits performing the code acquisition of signals with correlated time delays. Moreover, an interesting application of the proposed framework has been carried out, for the case of the acquisition of two navigation signals transmitted by a single satellite vehicle. The analysis and the results of this work are also presented in [P6].

Finally, within the framework of project [Pr4], considering a network of communicating peers localized within a limited area, a tight cooperative code acquisition technique has been designed, which envisages the exchange of the likelihood evaluations carried out by different nodes in order to increase the code acquisition capabilities. This solution allows to improve the code acquisition capabilities of the cooperating nodes, thus minimizing the mean acquisition time and reducing the computational complexity. The design and the results are also presented in [P7].

PERSONAL PUBLICATIONS

[P1] Gabelli, G.; Ediz, C.; Dempster, A.G.; Corazza G.E.; , "Cross-correlation Analysis for GNSS Interference Detection and Localization", submitted to IEEE Transactions on Aerospace and Electronic Systems.

[P2] Gabelli, G.; Ediz, C.; Dempster, A.G.; Corazza G.E.; , "GNSS Clutter Cancellation for GNSS Interference Detection and Localization", submitted to IEEE Transactions on Aerospace and Electronic Systems.

[P3] Gabelli, G.; Cetin, E.; Thompson, R.J.R.; Dempster, A.G.; Corazza, G.E.; , "GNSS Signal Cancellation for Enhanced Interference Detection and Localization", *International Global Navigation Satellite Systems Society IGNSS Symposium 2013, Proceedings of*, 2013, **Best Peer Reviewed Paper**.

[P4] Gabelli, G.; Casile, R.; Guidotti, A.; Corazza, G.E.; "GNSS Jamming Interference: Characterization and Cancellation," *Proceedings of the 2013 International Technical Meeting of The Institute of Navigation,* January 2013.

[P5] Gabelli, G.; Corazza, G.E.; Deambrogio, L.; Casile, R.; , "Code acquisition under strong dynamics: The case of TT&C for LEOP," *Advanced Satellite Multimedia Systems Conference (ASMS) and 12th Signal Processing for Space Communications Workshop (SPSC)*, 2012.

[P6] Deambrogio, L.; Gabelli, G.; Corazza, G.E.; , "Dyadic Cooperation in Code-Acquisition: a theoretical framework", to be submitted to IEEE Transactions on Vehicular Technology.

[P7] Gabelli, G.; Deambrogio, L.; Palestini, C.; Bastia, F.; Corazza, G.E.; Samson, J.; "Cooperative Code Acquisition Based on the P2P Paradigm," *Proceedings of the 2012 International Technical Meeting of The Institute of Navigation,* 2012.

[P8] Deambrogio, L.; Palestini, C.; Bastia, F.; Gabelli, G.; Corazza, G.E.; Samson, J.; , "Impact of high-end receivers in a peer-to-peer cooperative localization system," *IEEE Ubiquitous Positioning Indoor Navigation and Location Based Service (UPINLBS),* 2010.

[P9] Gabelli, G.; Palestini, C.; Cioni, S.; Vanelli-Coralli, A.; Corazza, G.E.; , "A performance and complexity optimization of joint code and frame synchronization for DVB-S2/RCS mobile," *IEEE Advanced satellite multimedia systems conference (ASMS) and the 11th signal processing for space communications workshop (SPSC),* 2010.

PROJECTS

[Pr1] "Detection, Evaluation and Characterization of Threats to Road Applications (DETECTOR)," FP7 Grant Agreement: 277619-2 - in collaboration with Nottingham Scientific Limited (NSL), SANEF, ARIC, Black Holes B.V. and IPSC.

[Pr2] "Spread Spectrum Codes Suitable for Mono-mode TT&C Transponder (TT&C)," ESA Contract: AO/1-5384/07/NL/JD - in collaboration with Thales Alenia Space France and the European Space Agency (ESA).

[Pr3] "Galileo Receiver for Mass Market Applications in the Automotive Area (GAMMA-A)," FP7 Grant Agreement: 228339 - in collaboration with Fraunhofer-Institut fur Integrierte Schaltungen IIS, IMST, Bosch, OECON, TeleConsult Austria, EADS Secure Networks, InPosition, Tele+ Italia, Thales Alenia Space and EPFL.

[Pr4] "P2P Positioning," ESA contract: 22868/09/NL/AT - in collaboration with Politecnico di Torino and Istituto Superiore Mario Boella (ISMB).

[Pr5] "GNSS Environmental Monitoring System (GEMS) II," Australian Research Council (ARC) Linkage grant LP0882191 - led by the University of New South Wales with partners University of Adelaide and GPSat Systems.

CONTENTS

I INTERFERENCE MANAGEMENT TECHNIQUES 1

1 GNSS INTERFERENCE DETECTION AND LOCALIZATION 3
- 1.1 Introduction 3
- 1.2 System Model 5
- 1.3 Signal Cross-Correlation analysis 6
  - 1.3.1 Evaluation of $G_{i,j}(n,\tau)$ 7
  - 1.3.2 Evaluation of $I_{i,j}(n,\tau)$ 8
  - 1.3.3 Evaluation of $W_{i,j}(n,\tau)$, $SW_{i,j}(n,\tau)$ and $IW_{i,j}(n,\tau)$ 9
  - 1.3.4 Equivalent Signal-to-Noise Ratio 10
- 1.4 Scenario Analysis 10
  - 1.4.1 Satellite parameters domain evaluation 10
- 1.5 Model Accuracy 13
- 1.6 GNSS Signal Detection and Cancellation 16
  - 1.6.1 GNSS Signals Cross-Correlation Detection 16
  - 1.6.2 GNSS Signals Cross-Correlation Tracking, Cancellation and Interference Detection 19
  - 1.6.3 Efficient Implementation 20
- 1.7 Scenario and System Description 24
- 1.8 Performance Evaluation 25
  - 1.8.1 GNSS Satellite Cross-Correlation Detection performance 26
  - 1.8.2 Parameters Estimation Accuracy 27
  - 1.8.3 GNSS Cross-Correlation Cancellation Error 29
  - 1.8.4 Interference Detection 33
- 1.9 Conclusions 35

2 GNSS INTERFERENCE CANCELLATION 37
- 2.1 Introduction 37
- 2.2 System Model 38
- 2.3 Algorithm Description 39
  - 2.3.1 Waveform Acquisition 39
  - 2.3.2 Waveform Tracking and Cancellation 39
- 2.4 Numerical Results 40
  - 2.4.1 Simulations 42
  - 2.4.2 Emulation 45
  - 2.4.3 Complexity Evaluations 45
- 2.5 Conclusions 47

II CODE SYNCHRONIZATION TECHNIQUES 51

3 CODE-SYNCHRONIZATION FOR COMMUNICATIONS: THE CASE OF TT&C 53
- 3.1 Introduction 53
- 3.2 System model 54
  - 3.2.1 Working scenario: Launch and Early Orbit Phase 54
- 3.3 Synchronization subsystem 55

3.3.1 Code acquisition: coarse synchronization 56
3.3.2 Decision criterion 59
3.3.3 Frequency and Doppler rate estimation 60
3.4 Numerical results 62
3.4.1 System Optimization 63
3.4.2 Performance Evaluation 63
3.4.3 Complexity Evaluation 66
3.5 Conclusions 67
4 DYADIC COOPERATION IN CODE-ACQUISITION 69
4.1 Introduction 69
4.2 Single FSM Code Acquisition 70
4.3 Dyadic code acquisition strategies 72
4.3.1 Unidirectional Flow Dyadic Code Acquisition 72
4.3.2 Bidirectional Flow Dyadic Code Acquisition 73
4.4 Analytical Acquisition Time Evaluation 76
4.4.1 Single FSM Code Acquisition 77
4.4.2 Unidirectional Information Exchange 78
4.4.3 Bi-directional Information Exchange 80
4.5 Study case: Dual Band Galileo Aided Acquisition 81
4.5.1 Signal Structure 82
4.5.2 Receiver Architecture 83
4.6 Numerical Results 84
4.7 Conclusions 90
5 CODE-ACQUISITION IN P2P NAVIGATION NETWORKS 91
5.1 Introduction 91
5.2 Introduction 91
5.3 System Model 92
5.4 Code Acquisition in a P2P network 94
5.4.1 Rationale 94
5.4.2 Maximum Likelihood Cooperative Delay Detection 95
5.5 Performance Evaluation 97
5.5.1 Costs characterization 98
5.5.2 Simulation Scenario 99
5.6 Numerical Results 99
5.7 Conclusions 103
BIBLIOGRAPHY 109

LIST OF FIGURES

Figure 1 Analyzed System 11
Figure 2 Delay difference $\tilde{\zeta}(t)$ as a function of time 12
Figure 3 Doppler frequency difference $\tilde{\varphi}(t)$ behavior in time 13
Figure 4 Model accuracy for the case of high delay dynamics 14
Figure 5 Model accuracy for the case of high frequency dynamics 15
Figure 6 Model accuracy for high frequency dynamics: improved model. 16
Figure 7 Probability of false alarm, missed detection and error 27
Figure 8 CRB of the GNSS signal parameter estimations vs. equivalent signal to noise ratio. One satellite ($N_s = 1$) is considered in order to evaluate the performance. 28
Figure 9 MSE @ different C/N values in case of absence of Doppler rate uncertainty 30
Figure 10 MSE @ different C/N values in case of absence of Doppler rate uncertainty 30
Figure 11 MSE @ different C/N values in case of absence of Doppler rate uncertainty 31
Figure 12 MSE @ different C/N values: 100m baseline 31
Figure 13 MSE @ different C/N values: 1000m baseline 32
Figure 14 MSE @ different C/N values: 5000m baseline 32
Figure 15 Interference Detection ROCs. 100m baseline 34
Figure 16 Interference Detection ROCs. 1000m baseline 34
Figure 17 Interference Detection ROCs. 5000m baseline 35
Figure 18 Chirp Signal: residual power after cancellation 43
Figure 19 Single-tone: residual power after cancellation 44
Figure 20 Spread Spectrum Signal: residual power after cancellation 44
Figure 21 L1 band: received, estimated and residual signal spectra 45
Figure 22 L2 band: received, estimated and residual signal spectra 46
Figure 23 L5 band: received, estimated and residual signal spectra 46
Figure 24 General receiver code acquisition sub-system block diagram 56
Figure 25 Detector block diagram 57
Figure 26 Swiveling filter block diagram 58
Figure 27 Receiver operating characteristics 64
Figure 28 Mean Acquisition Time, $C/N_0 = 37$dBHz 64

Figure 29 Flow graph of the overall acquisition procedure in the case of single FSM code acquisition. 77
Figure 30 Flow graph of the overall acquisition procedure in the case of a fast Master 79
Figure 31 Flow graph of the overall acquisition procedure, in case of a slow Master case and MAX decision Slave. 81
Figure 32 E1-E5 signal relation 83
Figure 33 E5-E1 signal relation 83
Figure 34 MAT vs L_S: system optimization 85
Figure 35 MAT dependance on the ξ_M and ξ_S thresholds 86
Figure 36 Mean Acquisition Time versus C/N_0 dB 88
Figure 37 Cumulative Density Function: $C/N_{0,E_5} = 40$, $C/N_{0,E_1} = 35$ 89
Figure 38 Cumulative Density Function: $C/N_{0,E_5} = 42$, $C/N_{0,E_1} = 37$ 89
Figure 39 Cumulative Density Function: $C/N_{0,E_5} = 45$, $C/N_{0,E_1} = 40$ 90
Figure 40 Graphic representation of time references and measures. 94
Figure 41 Markov Chain associated to the Cooperative Code Acquisition (CCA) procedure 97
Figure 42 Comparison between classical acquisition and CCA - Soft Combining (CCA-SC) acquisition procedure with M0=50 100
Figure 43 Comparison between classical acquisition and CCA-SC acquisition procedure with M0=10 101
Figure 44 Comparison between classical and CCA-SC performance with varying numbers of aiding peers 101
Figure 45 Comparison between classical acquisition and CCA - Hard Combining (CCA-HC) strategies 102
Figure 46 Comparison between classical acquisition and CCA-SC strategies MATs 102
Figure 47 Comparison between classical acquisition and CCA-SC strategies MCs 103

LIST OF TABLES

Table 1 Ranges of the possible values of $\zeta_{i,j}^{(k)} T_s$ and $\varphi_{i,j}^{(k)}/T_s$ 13
Table 2 Maximum observation period guaranteeing $L > 0.8$ 15

Table 3 Maximum absolute values for ζ, φ for different baselines 25
Table 4 Algorithm parameters 25
Table 5 peak to peak cancelation figure [dB] 33
Table 6 Interfering Signal Parameters 42
Table 7 Acquisition Algorithm Parameters 42
Table 8 Tracking Algorithm Parameters 43
Table 9 Parameters used in numerical simulations 63
Table 10 Swiveling Filter: Frequency estimation RMSE 65
Table 11 LSE: Frequency estimation RMSE (C/N_0 =37 dBHz) 65
Table 12 Reduced MLE: Frequency estimation RMSE (C/N_0 =37 dBHz) 66
Table 13 Complexity Evaluation: Coarse Code Synchronization 66
Table 14 Complexity Evaluation: Frequency and Doppler rate estimation 67
Table 15 Galileo E1 and E5 main signal characteristics 82
Table 16 Optimum thresholds 87
Table 17 Arithmetic operation complexity in terms of basic operations 98

ACRONYMS

A-GNSS Assisted GNSS

AWGN Additive White Gaussian Noise

ADC Analog to Digital Converter

A-LLF Average Log-Likelihood Function

AGC Automatic Gain Control

ANPA Alternating Notch-Periodogram Algorithm

AOA Angle Of Arrival

BD Bi-Directional

CAS Coarse Acquisition Stage

CC Cross-Correlation

CCA Cooperative Code Acquisition

CCA-HC CCA - Hard Combining

CCA-SC CCA - Soft Combining

CDF Cumulative Density Function

CDM Code Division Multiplexing

CDMA Code Division Multiple Access

CRB Cramer Rao Bound

CUR Complete Uncertainty Region

CW Continuous Wave

DS-SS Direct Sequence Spread Spectrum

FFT Fast Fourier Transform

FM Frequency Modulated

FSM Finite State Machine

FW Frequency Window

GLLR Generalized Log-Likelihood Ratio

GNSS Global Navigation Satellite System

ICI Inter-Chip Interference

IFFT Inverse FFT

IoT Internet of Thing

LEOP Launch and Early Orbit Phase

LR Likelihood Ratio

LSE Least Square Estimator

MAI Multiple Access Interference

MAT Mean Acquisition Time

MC Mean Complexity

ML Maximum Likelihood

MLE Maximum Likelihood Estimator

MPU Master Processing Unit

MRC Maximal Ratio Combining

MSE Mean Square Error

NAV-COM Navigation-Communication

P2P Peer-to-Peer

PCA Principal Component Analysis

pdf probability density function

PM Phase Modulated

PN Pseudo-Noise

PSD Power Spectral Density

RFI Radio Frequency Interference

RMLE Reduced MLE

RMSE Root Mean Square Error

RNSS Regional Navigation Satellite Systems

ROC Receiver Operating Characteristics

RS Refinement Stage

RUR Reduced Uncertainty Region

SN Sensor Node

SNR Signal-to-Noise Ratio

SS Spread Spectrum

STFT Short-Time Fourier Transform

TC Threshold Crossing

TDOA Time Difference Of Arrival

TT&C Telemetry, Tracking and Control

TRMP Total Received Minimum Power

UD Uni-Directional

WAVE Wireless Access for Vehicular Environments

WA Waveform Acquisition

WT Wavelet Transform

Part I

INTERFERENCE MANAGEMENT TECHNIQUES

Modern infrastructures increasingly rely on the positioning and timing capabilities provided by the GNSS [31]. The weak power of the received GNSS signals makes them vulnerable to Radio Frequency Interference (RFI), which can deteriorate or even disrupt the provided services. In particular, in recent years the reliability of the GNSS systems is facing the problem of interfering signals transmitted by jammers and spoofers [6], [P4], and of other non-intentional sources of interference, like malfunctioning antennas [5]. Therefore, the GNSS itself has become a critical infrastructure which must be protected to function accurately and reliably.

The aim of part I of this thesis is to study and analyze techniques able to detect the presence of interfering signals, to determine the position of their sources, and to mitigate the effects of the interference.

1 GNSS INTERFERENCE DETECTION AND LOCALIZATION

1.1 INTRODUCTION

Due to the importance of GNSSs, systems able to detect and manage interference signals and sources are being deployed in order to guarantee the reliability of their services. As a matter of fact, by modifying the correlation function evaluated by the receivers, interference signals deteriorate localization and timing performance, possibly leading to complete service interruption. Disturbance due to interference signals increases with the received power: interferers become more and more dangerous as their sources approach to the GNSS receivers, and as the transmitted power increases. Therefore it is important to develop techniques able to identify the presence of eventual interference sources and to limit the received interference power. Accordingly, detection techniques have been proposed, based on the analysis of the gain of the receiver Automatic Gain Control (AGC), Carrier to Noise Ratio (C/N_0) level or Cross-Correlation (CC) of signals received at spatially separated nodes [24][30][54], which are able to detect very weak interference signals [46]. Moreover, interference source localization systems are being developed [12][60], mostly based on Angle Of Arrival (AOA) and Time Difference Of Arrival (TDOA) algorithms [19].

In this work, a system is considered, consisting of a network of spatially separated and time synchronized Sensor Nodes (SNs), connected to a central processing unit to estimate quickly the location of an interferer through TDOA measurements between nodes [12],[60],[59].

One factor which limits the performance of TDOA based RFI localization is the presence of GNSS signals in the received data. These create an undesired “clutter" due to the correlation peaks that can be mistaken for RFI or could affect the RFI TDOA estimation process by biasing or completely impeding the measurements [P4],[59]. This limits the power at which RFI can be detected and localized. This situation is expected to get worse as the number of GNSSs and Regional Navigation Satellite Systems (RNSS) increases [60].

In [P3] a simple description of the GNSS CC function is proposed and a simple non-coherent algorithm is introduced in order to limit the effects of the satellite signals on interference detection/localization. The results show that the GNSS CC is highly variable in time and that, in order to eliminate the effects of the satellite signals on interference detection/localization, the GNSS signals CC must be coherently estimated and canceled.

In this chapter an accurate analysis of the behavior of the CC of the signals received at different nodes in the presence of GNSS satellite signals, interference signal and thermal noise is carried out: a closed form model for the GNSS “clutter" is proposed and the ranges

of the values that the parameters can assume are determined, the interference peak level is evaluated considering the interference signal energy, and an ad-hoc figure of merit for the evaluation of the GNSS CC signal to noise is proposed. The analysis carried out is particularly interesting since it can be effectively exploited in order to describe the behavior of all the received signals CC: in particular it provides a description of the GNSS CC clutter, which is valid for any GNSS system, and for any of their signals, independently on the particular spreading codes. The described analysis is also presented in [P1]

Moreover, an algorithm is designed, to enhance the sensitivity of the RFI detection and localization techniques proposed in [12]. In [59] a simple solution for the detection of the interference in the presence of GNSS signals CC is proposed, which uses a mean-change detection technique that tries to characterize the behavior of the cross-correlation peaks in each delay bin over time and looks for any unusual change over time. The solution is able to improve the detection performance, but in order to approach the GNSS signal free case the GNSS clutter must be strongly mitigated. In [P3] an algorithm that aims to eliminate the GNSS clutter operating non-coherently is proposed. It entails calculating the mean absolute value of the CC function at successive delay bins and in subtracting the result from the CC squared absolute value.

Following on from this, an algorithm which is able to track and cancel the satellite CC contributions, and to detect interference is proposed. This approach works without the need of any GNSS receiver signal processing (only the RF front-end, capable of receiving GNSS signals is required). The approach consists of detecting the number of CC components, estimating their characteristic parameters and performing cancellation by subtracting the estimated clutter components from the numerically evaluated CC function. The problem of the detection and estimation of the different components is not straightforward, since a model selection problem must be solved in order to identify the number of different CC peaks which are generated by different signals. Moreover, the number of signals is in general variable given the fact that the number of visible satellites changes over time. Furthermore, a joint estimation problem for a number of parameters depending on the number of detected signals must be carried out.

These two linked problems have been widely studied in the literature. In [32] the detection/estimation problem for a number of sinusoidal signals was tackled, and a theoretical framework describing the Maximum Likelihood (ML) solution was provided. In [26][27] and [43], an iterative solution called Alternating Notch-Periodogram Algorithm (ANPA) is proposed, for the detection/estimation of sinusoidal signals. The proposed algorithm consists in decomposing the original multidimensional ML problem into simple mono-dimensional problems of detection of the periodogram peaks [32]. At each iteration, only one single sinusoidal frequency is detected/estimated while the other frequencies are notched. If the notching operation is successful, at each iteration, the detection/estimation operation can be as accurate as the conventional periodogram for the single-sinusoid

case. In this work, the ANPA is applied to the problem of detection/estimation of GNSS CC components in order to able to reconstruct the behavior of the GNSS contributions and to detect the interference signal. The described algorithm is also presented in [P2].

The rest of this chapter is structured as follows: in section 1.2 the system model considered for the received satellite signals is presented; in section 1.3 a theoretical analysis of the CC function is carried out; in section 1.4 an evaluation of the parameters characterizing the GNSS CC function in the worst case scenario is performed and numerical results showing the accuracy of the proposed analytical model are reported in section 1.5. Section 1.6 describes the interference detection sensitivity enhancement algorithm based on the notch-periodogram and the relative efficient implementation. In Section 1.7, the description of a realistic scenario is provided and the performance evaluation is presented in Section 1.8. Concluding remarks are given in Section 1.9.

1.2 SYSTEM MODEL

As discussed, numerous interference detection and localization techniques have been developed and are well known in the literature. Exploiting a network of spatially separated and time-synchronized nodes, it is possible to exploit the CC between the signals received at pairs of nodes in order to carry out both the detection and the localization tasks. In the following, a description of the considered signals is carried out.

Assuming that two spatially separated SNs receive the same number N_s of satellite signals $s_k(t)$ $(k = 1, \dots, N_s)$ and the same interfering signal $s_I(t)$, the base-band equivalent received signal at the i-th receiver can be written as:

$$\begin{aligned} r_i(t) \;=\; & \sum_{k=1}^{N_s} \sqrt{P_i^{(k)}}\, s_k(t-\xi_i^{(k)})\, e^{j(\theta_i^{(k)}+2\pi f_i^{(k)} t)} + \\ & + \sqrt{P_i^{(I)}}\, s_I(t-\xi_i^{(I)})\, e^{j(\theta_i^{(I)}+2\pi f_i^{(I)} t)} + w_i(t) \end{aligned} \tag{1}$$

where $P_i^{(k)}$ ($P_i^{(I)}$) is the k-th signal (Interference signal) received power at the i-the receiver, $\xi_i^{(k)}$, $f_i^{(k)}$, ($\xi_i^{(I)}$, $f_i^{(I)}$) are the time delay and frequency offset respectively, and $w_i(t)$ is the Additive White Gaussian Noise (AWGN) with power spectral density N_0. Defining the operators $\lfloor i \rfloor_A = \lfloor \frac{i}{A} \rfloor$ and $|i|_A = i \bmod A$, the k-th satellite signal can be written as

$$s_k(t) = \sum_{l=-\infty}^{+\infty} D_k(\lfloor l \rfloor_{L_S})\, a_k(|l|_{L_S})\, g(t - lT_c) \tag{2}$$

where $D_k(l)$ and $a_k(l)$ are the data sequence and the pseudo-random spreading sequence transmitted by the k-th satellite, L_S is the spreading sequence length, and $g(t)$ is the response of the pulse-shaping filter, which for the case of GNSS signals is a rectangular function with the support limited to $[0, T_c]$, where T_c is the chip period.

In the time discrete domain the received signal is transformed into succession of samples, which can be written as

$$\begin{aligned} r_i(u) = \\ = \sum_{k=1}^{N_s} \sqrt{E_i^{(k)}} s_k(uT_s - \xi_i^{(k)}) e^{j(\theta_i^{(k)} + 2\pi\phi_i^{(k)}u} + \\ + \sqrt{E_i^{(I)}} s_I(uT_s - \xi_i^{(I)}) e^{j(\theta_i^{(I)} + 2\pi\phi_i^{(I)}u)} + w_i(u) \end{aligned} \tag{3}$$

where T_s is the sampling period, E_i^k (E_i^I) is the mean signal (and interference) energy per sample, $\phi_i^{(k)} = f_i^{(k)} T_s$ ($\phi_i^{(I)} = f_i^{(I)} T_s$) is the normalized frequency offset, and $w_i(u)$ are the noise samples distributed as i.i.d. Gaussian random variables with zero mean and variance equal σ^2. In the following the time-discrete signal expression will be considered.

1.3 SIGNAL CROSS-CORRELATION ANALYSIS

In order to perform interference detection and localization the CC between signals received at two SNs, i and j, must be evaluated at different lags τ and for successive time instants. Assuming to calculate it periodically (with period $T_R = \Delta T_s = 1/f_R$), the CC can be efficiently estimated according to the following:

$$R_{i,j}(n,\tau) = \frac{1}{\sqrt{N_{cc}}} \sum_{u=n\Delta}^{n\Delta+N_{cc}} r_i(u) r_j^*(u+\tau) \tag{4}$$

where N_{cc} is the length (in samples) of the CC window. Note that τ could be in general a time continuous variable, but since we operate in the digital signal processing domain, only time discrete values τ are considered. By substituting the second term of (3) into (4), and by means of a simple algebric manipulations, we find

$$\begin{aligned} R_{i,j}(n,\tau) \quad = \quad & G_{i,j}(n,\tau) + I_{i,j}(n,\tau) + GI_{i,j}(n,\tau) + \\ & + W_{i,j}(n,\tau) + GW_{i,j}(n,\tau) + IW_{i,j}(n,\tau) \end{aligned} \tag{5}$$

The $G_{i,j}(n,\tau)$ term is the cross-correlation between the GNSS signals received at the two SNs, $I_{i,j}(n,\tau)$ is the correspondent for the interference signals, and $GI_{i,j}(n,\tau)$ is the crossed GNSS-interference contribution. Similarly, the terms in the second row of (5) are the random noise-noise, GNSS-noise and interference-noise cross-correlation terms.

As discussed at the beginning of this chapter, the knowledge of the behavior of (5) is of primary importance in order to guarantee the reliability and the effectiveness of the interference related operations. In the following a complete description of the GNSS CC behavior $G_{i,j}(n,\tau)$ is carried out by evaluating, as well as an evaluation of the deterministic level of the peak of $I_{i,j}(n,\tau)$ (which is the measure used in the interference detection/localization process [19]) and of the overall noise level.

1.3.1 *Evaluation of* $G_{i,j}(n,\tau)$

Assuming the GNSS signals to be perfectly orthogonal to each other, the GNSS component cross-correlation can be written as:

$$\begin{aligned} G_{i,j}(n,\tau) &= \\ &= \frac{1}{\sqrt{N_{cc}}}\sum_{k=1}^{N_s}\left[\sum_{u=n\Delta}^{n\Delta+N_{cc}}\left(\sqrt{E_i^{(k)}}\sum_{l=-\infty}^{+\infty}D_k(\lfloor l\rfloor_{L_S})a_k(|l|_{L_S})\cdot\right.\right. \\ &\quad \left.\cdot g(uT_s-lT_c-\xi_i^{(k)})e^{j[2\pi\phi_i^{(k)}u+\theta_i^{(k)}]}\right)\cdot \\ &\quad \cdot\left(\sqrt{E_j^{(k)}}\sum_{m=-\infty}^{+\infty}D_k(\lfloor m\rfloor_{L_S})a_k(|m|_{L_S})\cdot\right. \\ &\quad \left.\left.\cdot g\left((u+\tau)T_s-mT_c-\xi_j^{(k)}\right)e^{j[2\pi\phi_j^{(k)}(u+\tau)+\theta_j^{(k)}]}\right)^*\right] \end{aligned}$$

where $()^*$ is the complex conjugate operator. Let us define the time difference of arrival $\zeta_{i,j}^{(k)}$ of the signals received at the pair of receivers i and j as,

$$\zeta_{i,j}^{(k)} = \frac{\xi_j^{(k)}-\xi_i^{(k)}}{T_s} \tag{6}$$

Since for both detection and localization purposes we are interested in analyzing the behavior of the CC function for τ belonging to the set of the possible values of $\zeta_{i,j}^{(k)}$, and being $\zeta_{i,j}^{(k)}$ limited by the distance d between the sensor nodes to the range

$$\zeta_{i,j}^{(k)} \in \left[-\frac{d}{cT_s},\frac{d}{cT_s}\right] \tag{7}$$

where c is the speed of light, considering $d < 10^4$m and assuming the auto-correlation of the spreading sequences to be negligible when the time offset is larger than one chip period, the only terms of equation (6) leading to a significant result are those with $m = l$, and the CC can be written as

$$\begin{aligned} &G_{i,j}(n,\tau) \\ &\simeq \sum_{k=1}^{N_s}\left(\sqrt{E_i^{(k)}E_j^{(k)}}\sqrt{N_{cc}}\,\mathrm{sinc}(\varphi_{i,j}^{(k)}N_{cc})R_g(\tau-\zeta_{i,j}^{(k)})\right. \\ &\quad \left.\cdot\exp\left\{j[\theta_{i,j}^{(k)}+2\pi\varphi_{i,j}^{(k)}n]\right\}\right) \end{aligned}$$

where

$$\begin{aligned} \varphi_{i,j}^{(k)} &= \phi_i^{(k)}-\phi_j^{(k)} \\ \theta_{i,j}^{(k)} &= \theta_i^{(k)}-\theta_j^{(k)}+2\pi\varphi_{i,j}^{(k)}N_{cc}/2-2\pi\phi_j^{(k)}\tau \end{aligned} \tag{8}$$

and $R_g(\tau)$ is the transmitted pulse auto-correlation function, with support $[-T_g,T_g]$.

At this point it must be noted that the parameters defined in (8) depend on τ; however, since for each satellite the support of the CC in the τ domain is not greater than $2T_g$ and centered around $\zeta_{i,j}^{(k)}$, considering that for base-band signals $\phi_i^{(k)} < 5$ kHz [31], it is possible to approximate the parameters defined in (8) with

$$\begin{aligned} \varphi_{i,j}^{(k)} &= \phi_i^{(k)} - \phi_j^{(k)} \\ \theta_{i,j}^{(k)} &= \theta_i^{(k)} - \theta_j^{(k)} + 2\pi\varphi_{i,j}^{(k)} N_{cc}/2 - 2\pi\phi_j^{(k)}\zeta_{i,j}^{(k)} \end{aligned} \tag{9}$$

which eliminates the dependance on τ. Finally, by defining

$$\begin{aligned} A_k &= \sqrt{E_i^{(k)} E_j^{(k)}}\sqrt{N_{cc}}\,\mathrm{sinc}(\varphi_{i,j}^{(k)} N_{cc}) e^{j\theta_{i,j}^{(k)}} \\ \omega_{i,j}^{(k)} &= [\zeta_{i,j}^{(k)}, \varphi_{i,j}^{(k)}] \\ S_{i,j}(n,\tau;\omega_{i,j}^{(k)}) &= R_g(\tau - \zeta_{i,j}^{(k)}) E^{j2\pi\varphi_{i,j}^{(k)} n} \end{aligned} \tag{10}$$

we obtain

$$\begin{aligned} G_{i,j}(n,\tau) &\simeq \sum_{k=1}^{N_s} A_k R_g(\tau - \zeta_{i,j}^{(k)}) e^{j2\pi\varphi_{i,j}^{(k)} n} \\ &= \sum_{k=1}^{N_s} A_k S_{i,j}(n,\tau;\omega_{i,j}^{(k)}) \end{aligned} \tag{11}$$

1.3.2 *Evaluation of* $I_{i,j}(n,\tau)$

Similarly to the satellite signal case, the interference CC function $I_{i,j}(n,\tau)$ is defined as

$$\begin{aligned} &I_{i,j}(n,\tau) \\ &= \frac{1}{\sqrt{N_{cc}}} \sum_{u=n\Delta}^{n\Delta+N_{cc}} \left(\sqrt{E_i^{(I)}} s_I(uT_s - \xi_i^{(I)}) e^{j(\theta_i^{(I)} + 2\pi\phi_i^{(I)} u)} \right) \\ &\quad \cdot \left(\sqrt{E_j^{(I)}} s_I\left((u+\tau)T_s - \xi_j^{(I)}\right) e^{j(\theta_j^{(I)} + 2\pi\phi_j^{(I)}(u+\tau))} \right)^* \end{aligned} \tag{12}$$

Since the interference signal is not known a-priori, it is not possible to carry out a complete evaluation of the CC function over the whole time and lag domain. A description of the behavior is possible only for $\tau = \zeta_{i,j}^{(I)} = (\xi_j^{(I)} - \xi_i^{(I)})/T_s$. As a matter of facts, for $\tau = \zeta_{i,j}^{(I)}$ the interfering signals received at two nodes are perfectly aligned, and the CC results to be equal to

$$I_{i,j}(n,\zeta_{i,j}^{(I)}) \simeq A_I e^{j2\pi\varphi_{i,j}^{(I)} n} \tag{13}$$

where

$$\begin{aligned} A_I &= \sqrt{E_i^{(I)} E_j^{(I)}}\sqrt{N_{cc}}\,\mathrm{sinc}(\varphi_{i,j}^{(I)} N_{cc}) e^{j\theta_{i,j}^{(I)}} \\ \varphi_{i,j}^{(I)} &= \phi_i^{(I)} - \phi_j^{(I)} \\ \theta_{i,j}^{(I)} &= \theta_i^{(I)} - \theta_j^{(I)} + 2\pi\varphi_{i,j}^{(I)} N_{cc}/2 \end{aligned}$$

This means that, similarly to the GNSS CC contributions, the peak of the interference CC presents a sinusoidal behavior in the time domain.

1.3.3 *Evaluation of* $W_{i,j}(n,\tau)$, $SW_{i,j}(n,\tau)$ *and* $IW_{i,j}(n,\tau)$

The term $W_{i,j}(n,\tau)$ is the CC of the noise realizations $w_i(u)$ and $w_j(u)$. Assuming to have an equal noise level at the two SNs, the noise CC $W_{i,j}(n,\tau)$ samples can still be described as Gaussian random variables with zero mean and variance equal to

$$\sigma_W^2 = \sigma^4 \tag{14}$$

On the other hand, the terms $SW_{i,j}(n,\tau)$ and $IW_{i,j}(n,\tau)$ are due to the cross-product between the GNSS signals and the noise processes, and between the interference signal and the noise processes, respectively. Also in this case, by observing that the CC is obtained as a sum of a number of products, the probability density function (pdf) of the $GW_{i,j}(n,\tau)$ and $IW_{i,j}(n,\tau)$ samples is still complex Gaussian with zero mean and variance equal to

$$\sigma_{GW}^2 = \sum_{k=1}^{N_s} \left(E_i^{(k)} + E_j^{(k)} \right) \sigma^2 \tag{15}$$

and

$$\sigma_{IW}^2 = \left(E_i^{(I)} + E_j^{(I)} \right) \sigma^2 \tag{16}$$

respectively.

For the sake of simplicity we define the overall CC random noise as

$$N_{i,j}(n,\tau) = W_{i,j}(n,\tau) + GW_{i,j}(n,\tau) + IW_{i,j}(n,\tau) \tag{17}$$

Since $N_{i,j}(n,\tau)$ is obtained as the sum of products of a number of random terms, the samples are modeled as Gaussian random variables with zero mean and variance equal to σ_N^2

$$\sigma_N^2 = \sigma_W^2 + \sigma_{GW}^2 + \sigma_{IW}^2 \tag{18}$$

This result allows to describe the noise level after the evaluation of the correlation and plays a central role in the evaluation of the performance of any detection/localization technique.

In the following we will identify as $ICR = |A_I|^2/|A|^2$ the ratio between the interference and the GNSS signals amplitudes, and as $INR = |A_I|^2/\sigma_N^2$ the interference to noise ratio. It is interesting to note that ICR and INR are the two parameters that determine the performance of the interference detection/localization performance. Since the objective of the considered system is detecting and tracking the CC component due to the interference signal, in the following a technique allowing to estimate the behavior and remove the $G_{i,j}(n,\tau)$ component is proposed.

1.3.4 *Equivalent Signal-to-Noise Ratio*

Considering the previous results, it is useful to define a new figure of merit, which is the equivalent signal to noise ratio of the CC function. In particular, let us consider a single satellite signal received at the two sensor nodes with the same signal to noise level C/N_0; we define the equivalent CC to noise ratio as

$$\begin{aligned} \frac{E_{cc}}{\sigma_N^2} &= \left(\frac{C}{N_0 B}\right)^2 N_{cc}\mathrm{sinc}^2(\varphi_{i,j}N_{cc})\frac{1}{1+2\frac{C}{N_0 B}}\|\mathbf{R}_g\|^2 \\ &\simeq \left(\frac{C}{N_0 B}\right)^2 N_{cc}\mathrm{sinc}^2(\varphi_{i,j}N_{cc})\|\mathbf{R}_g\|^2 \end{aligned} \tag{19}$$

where

$$\|\mathbf{R}_g\| = \sqrt{\sum_{i=1}^{N_\tau}|R_g(\tau_i)|^2} \tag{20}$$

and B is the bandwidth of the receivers front-end. It is interesting to note that the defined value is the ratio of the observed GNSS cross-correlation total energy over the mean noise samples variance.

Equation (19) clearly shows that the CC to noise ratio depends on the correlation length N_{cc}. As discussed in [14], an closed form expression for the optimum value of N_{cc} (the value which maximizes the signal to noise ratio) cannot be found, but it can be efficiently approximated as

$$N_{cc} \simeq \frac{3}{8\varphi}$$

The importance of this result lies in the fact that, since the maximum frequency error affecting the system can be known, the coherent correlation length that maximizes N_{cc} can be simply determined.

1.4 SCENARIO ANALYSIS

The closed form expression derived in the previous section for the GNSS CC has been obtained under the assumption of constant time-delay and frequency difference. In general, these parameters depend on the geometry of the system, i.e. on the relative position and velocity of the satellite vehicles transmitting the GNSS signals with respect to the SNs. In this section, an evaluation of the ranges and of the dynamics of the time-delay and frequency parameters $\zeta_{i,j}^{(k)}, \varphi_{i,j}^{(k)}$ is carried out, by considering different baselines, i.e. different distances between the pair of receivers, and the satellite dynamics.

1.4.1 *Satellite parameters domain evaluation*

In order to perform the aforementioned characterization, let us refer to Fig. 1, representing two sensor nodes R_i and R_j lying on the Earth surface, and a satellite S having a trajectory parallel to the represented plan. This particular scenario has been selected as the worst

case scenario, representing the case in which the parameters assume the maximum absolute values. Let us define the delay difference as

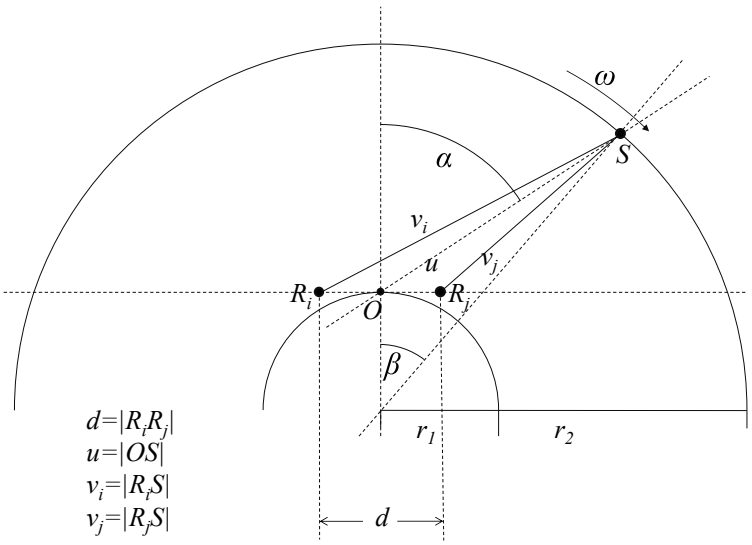

Figure 1: Analyzed System

the function of time $\tilde{\zeta}(t)$:

$$\tilde{\zeta}(t) = \frac{\nu_j(t) - \nu_i(t)}{c}$$

where $\nu_j(t)$ and $\nu_i(t)$ are the distances between the satellite and the sensor nodes R_j and R_i, respectively, at time t. The behavior of the delay difference $\tilde{\zeta}(t)$ can be evaluated assuming the satellite S to be moving with a constant angular velocity ω. Considering the represented system, the delays $\nu_i(t)$ and $\nu_j(t)$ can be expressed as

$$\nu_i(t) = \sqrt{\left(\frac{d}{2}\right)^2 + u(t)^2 - u(t)d\cos\left(\frac{\pi}{2} - \alpha(t)\right)}$$

$$\nu_j(t) = \sqrt{\left(\frac{d}{2}\right)^2 + u(t)^2 - u(t)d\cos\left(\frac{\pi}{2} + \alpha(t)\right)}$$

where

$$\begin{aligned} u(t) &= \sqrt{r_1^2 + r_2^2 - 2r_1 r_2 \cos(\beta(t))} \\ \alpha(t) &= \arcsin\left(\frac{r_2 \sin(\beta(t))}{u(t)}\right) \end{aligned}$$

and with $\beta(t) = \omega t$. Considering $r_1 = 6.37 \cdot 10^6$m, $r_2 = 26.6 \cdot 10^6$m and $\omega = 2\pi/(12 \cdot 60 \cdot 60)$, the behavior of $\tilde{\zeta}(t)$ is shown in Fig. 2 for four different baselines characterized by receivers separated by d=100m, 500m, 1000m, and 5000m and considering t variable between 0 and 7200s (corresponding to $\alpha = 0$ and $\alpha = \pi/2$, which are the maximum and minimum altitude positions, respectively). It is possible to observe that $\tilde{\zeta}(t)$ assumes the maximum value when the satellite is in low visibility, since in this case the difference between

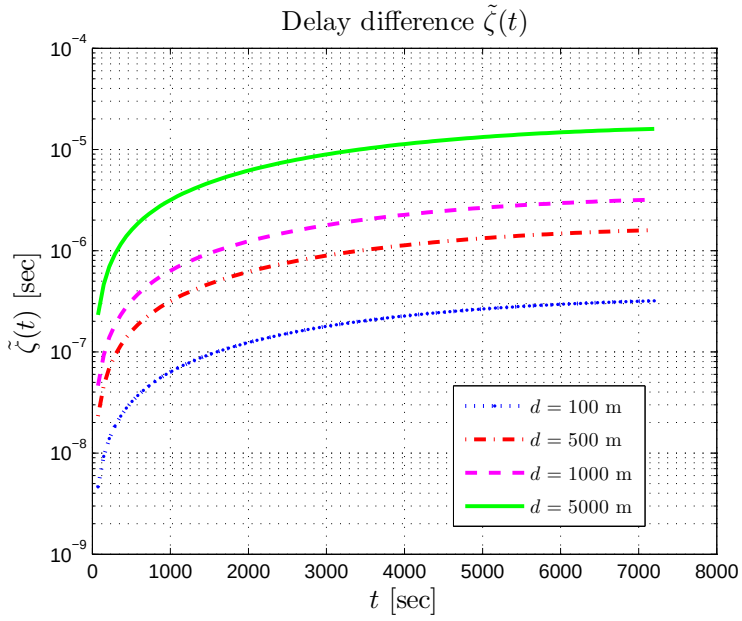

Figure 2: Delay difference $\tilde{\zeta}(t)$ as a function of time

the delays converges to d. Moreover, the delay difference rapidly increases with the baseline. Accordingly, it is possible to conclude that the possible values of the parameter $\zeta_{i,j}^{(k)}$ belong to the range

$$\zeta_{i,j}^{(k)} \in \left[-\frac{\max(\tilde{\zeta}(t))}{T_s}, \frac{\max(\tilde{\zeta}(t))}{T_s}\right] = \left[-\frac{d}{cT_s}, \frac{d}{cT_s}\right] \tag{21}$$

The maximum absolute values for $\zeta_{i,j}^{(k)}$ are reported in the first column of Table 1 for the four considered baselines. Moreover, it is interesting observing that the delay difference $\tilde{\zeta}(t)$ is weakly variable in time for low altitudes, but changes rapidly when the satellite is at maximum altitudes. Since in equation (11) a constant value for the parameter $\zeta_{i,j}^{(k)}$ has been considered, in the following section an evaluation of the accuracy of the proposed approximation will be carried out.

On the other hand, in order to evaluate the frequency characteristics, we define the Doppler frequency difference function as

$$\tilde{\varphi}(t) = \tilde{\phi}_i(t) - \tilde{\phi}_j(t)$$

where

$$\tilde{\phi}_i(t) = \left(\frac{c}{c + v_{S,i}(t)}\right) f_0$$
$$\tilde{\phi}_j(t) = \left(\frac{c}{c + v_{S,j}(t)}\right) f_0$$

with c being the velocity of the wave in the medium, $v_{S,i}(t)$ ($v_{S,j}(t)$) the velocity of the satellite relative to the i-th (j-th) receiver and f_0 the frequency of the transmitted signal. Considering GPS L1 signals ($f_0 = 1575.42$ MHz), we obtain the results shown in Fig. 3. From the figure we can observe that $\tilde{\varphi}(t)$ assumes the maximum absolute values when the satellite is at high altitudes and decreases with decreasing altitude; in the following section an evaluation of the accuracy

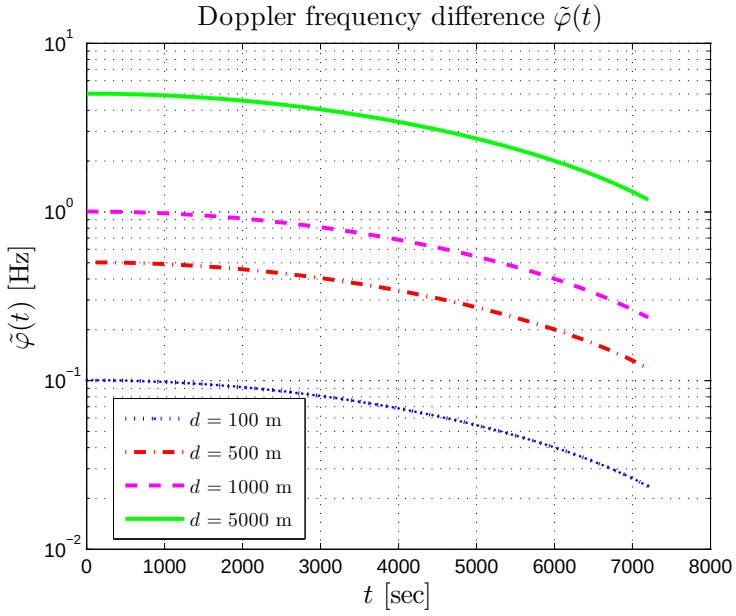

Figure 3: Doppler frequency difference $\tilde{\varphi}(t)$ behavior in time

of the proposed fixed parameters model will be provided. Finally, by substituting the values of $\tilde{\varphi}(t)$ into equation (9) the maximum possible absolute values for $\varphi_{i,j}^{(k)}$ (still normalized to the sampling period) are reported in Table 1.

Table 1: Ranges of the possible values of $\zeta_{i,j}^{(k)} T_s$ and $\varphi_{i,j}^{(k)}/T_s$

d [m]	$\max(\zeta_{i,j}^{(k)} T_s)$ [s]	$\max(\varphi_{i,j}^{(k)}/T_s)$ [Hz]
100	$3.33 \cdot 10^{-7}$	0.1
500	$1.67 \cdot 10^{-6}$	0.5
1000	$3.33 \cdot 10^{-6}$	1.0
5000	$1.67 \cdot 10^{-5}$	5.0

1.5 MODEL ACCURACY

In this section an evaluation of the accuracy of the closed form approximation provided in eq. (11) is carried out, considering the system configuration analyzed in Section 1.4.

In order to evaluate the accuracy of the proposed model, for a single satellite signal, the following figure of merit is used

$$L = \frac{\left| \mathbf{G}_{i,j}^{A} \times \mathbf{G}_{i,j}^{N\,*} \right|^2}{\|\mathbf{G}_{i,j}^{A}\|^2 \|\mathbf{G}_{i,j}^{N}\|^2} \tag{22}$$

where $\mathbf{G}^{K}_{i,j}$ ($K \in \{A, N\}$) is the CC matrix

$$\mathbf{G}^{K}_{i,j} = \begin{bmatrix} G_{i,j}(n_0,\tau_0) & \dots & G_{i,j}(n_0,\tau_1) \\ G_{i,j}(n_0+1,\tau_0) & \dots & G_{i,j}(n_0+1,\tau_1) \\ \vdots & \ddots & \\ G_{i,j}(n_1,\tau_0) & \dots & G_{i,j}(n_1,\tau_1) \end{bmatrix}$$

calculated by means of the proposed analytical model ($K = A$), and by numerically cross-correlating satellite signals with delay and frequency evaluated according to the model shown in the previous section ($K = N$), and where

$$\begin{aligned} \|\mathbf{G}\| &= \sqrt{\sum_{n=n_0}^{n_1}\sum_{\tau=\tau_0}^{\tau_1} |G(n,\tau)|^2} \\ \mathbf{G}^{A} \times \mathbf{G}^{N} &= \sum_{n=n_0}^{n_1}\sum_{\tau=\tau_0}^{\tau_1} G^{A}(n,\tau) G^{N*}(n,\tau) \end{aligned}$$

It can be noted that L measures the likelihood between the analytical and the numerical CCs, thus it is equal to 1 when the two functions are exactly identical.

A sampling frequency $f_s = 16 \cdot 1.023\text{Hz}$, a fixed number of time samples $N_n = n_1 - n_0 + 1 = 65$, and different CC sampling periods T_R (corresponding to different durations of the observation period $T_0 = N_n T_R$) are considered, and the initial lag τ_0 and final lag τ_1 are set to -300 and 300 samples, respectively (the number of lags $N_\tau = \tau_1 - \tau_0 + 1$ is equal to 601). The performance is evaluated in case of high altitude satellites (corresponding to $n_0 T_R = 0\text{s}$) and in case of low altitude satellites (corresponding to $n_1 T_R = 6500\text{s}$). The results are shown in Fig. 4 and 5 respectively. In the first case (high altitude)

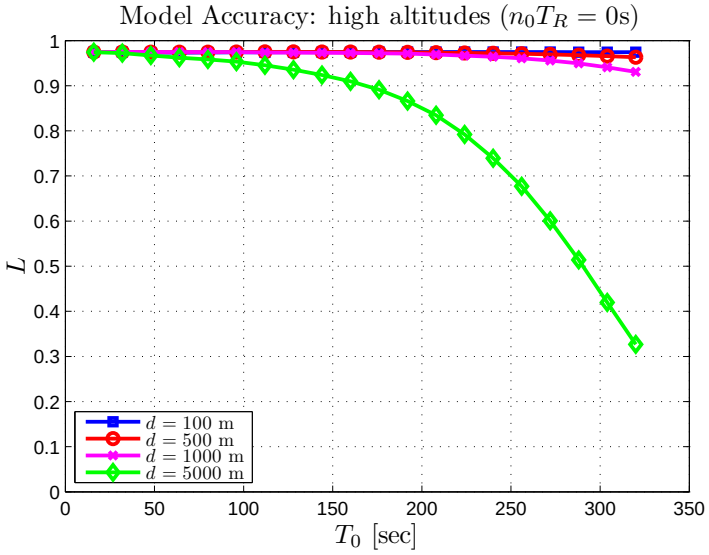

Figure 4: Model accuracy for the case of high delay dynamics

it is possible to observe that for the $d = 100, 500, 1000$m baselines the accuracy of the model is always high ($L \approx 0.976$) over the whole

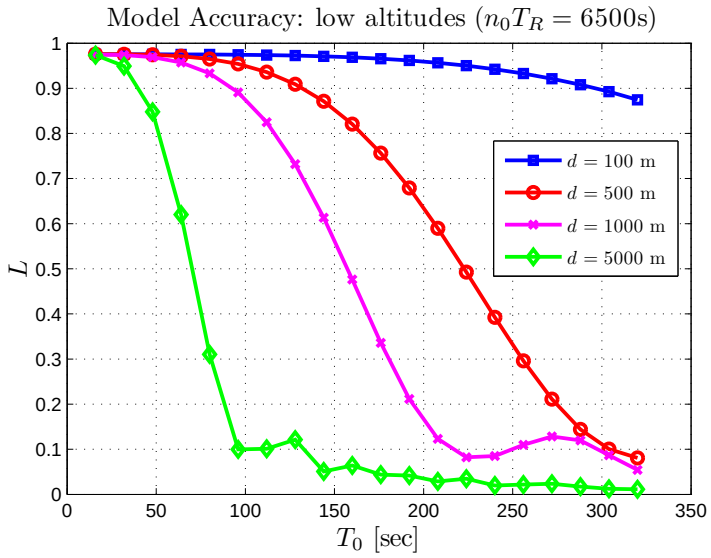

Figure 5: Model accuracy for the case of high frequency dynamics

Table 2: Maximum observation period guaranteeing $L > 0.8$

d [m]	$T_{0,MAX}$ [s]
100	350
500	175
1000	130
5000	55

range of the considered T_0, due to the fact that the parameters of the actual signals vary slowly in time. On the other hand, for the large $d = 5000$m baseline L remains larger than 0.9 only for $T_0 < 170$s, and degrades rapidly to $L = 0.32$ with T_0 increasing to 320s. This behavior is mostly due to the delay variation, which moves the position of the peak in the τ domain.

In the second case, it is possible to observe form Figure 5 that the fast variation of the frequency parameter strongly affects the accuracy of the model. For the short $d = 100$m baseline the model remains accurate over the whole range of considered periods, but for the other baselines the accuracy decreases rapidly: identifying as $T_{0,MAX}$ the maximum period duration according to which L remains larger than 0.8 the values collected in table 2 have been found.

Since the model is strongly affected by variation of the frequency, the accuracy of an improved model considering a linearly varying frequency has been evaluated. The proposed model comprises a constant frequency-rate term ρ and can be written according to:

$$G_{i,j}(n,\tau) = \sum_{k=1}^{N_s} \left(A_k R_g(\tau - \zeta_{i,j}^{(k)}) e^{j2\pi\varphi_{i,j}^{(k)} n + \pi\rho n^2} \right) \tag{23}$$

The results are shown in Fig. 6. Comparing these results with those of Fig. 5 makes clear that the main reason leading to the accuracy degradation is the variation of the frequency parameter. The improved

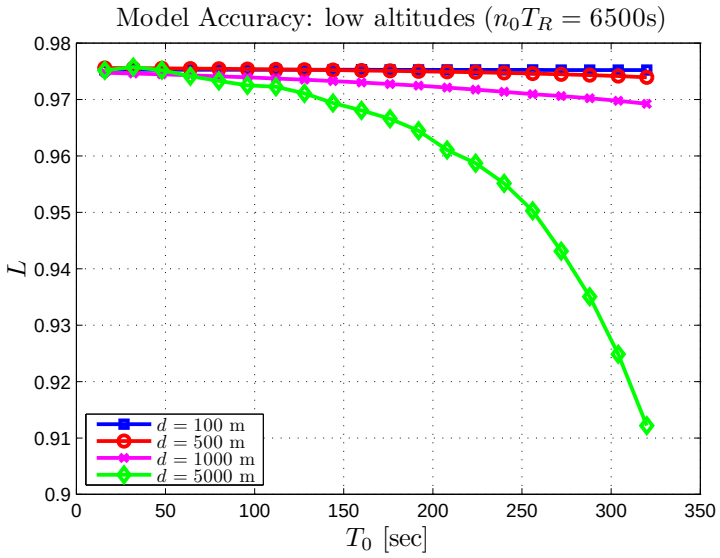

Figure 6: Model accuracy for high frequency dynamics: improved model.

model can thus be efficiently exploited in cases where T_0 larger than the identified $T_{0,MAX}$ is required, i.e. in case very long observations need to be used.

1.6 GNSS SIGNAL DETECTION AND CANCELLATION

The usual solution for the detection and TDOA localization of interference signals consists of detecting and tracking the interference CC peak [19]. Nevertheless, when the interference signal is masked between GNSS signals, it becomes impossible to distinguish the contribution due to interference from the contributions due to the satellite signals. In order to separate the two contributions, a solution is proposed, consisting of detecting, estimating and canceling the cross-correlation term due to the GNSS signals, and performing the detection and the TDOA estimation using the residual CC function after removal. In the following, an algorithm working in two successive steps is proposed: in the first step, the detection of the GNSS signals is performed, based on the notch periodogram approach, which determines the model order of the considered observable. In the second step, using the evaluated model order, the GNSS signal CC contributions are tracked and removed, leaving only the CC contributions due to the interference signal and to the overall random noise.

1.6.1 *GNSS Signals Cross-Correlation Detection*

The problem of detecting the number of GNSS satellite signals and of estimating their parameters can be solved by exploiting different approaches [32], which can be distinguished between decomposed detection and estimation approaches, and joint detection and estimation approaches. In this work a joint detection and estimation approach is selected, based on the application of the ML criterion.

For the sake of simplicity, in the following the matrix notation is used. Considering the GNSS CC function (11), observed over a finite set of N_n time instants $\{n_0T_R, (n_0+1)T_R, \ldots, n_1T_R\}$ $(N_n = n_1 - n_0 + 1)$ separated by the period T_R, and a finite sets of N_τ lags $\{\tau_0T_s, (\tau_0 + 1)T_s \ldots, \tau_1T_s\}$ $(N_\tau = \tau_1 - \tau_0 + 1)$, and removing the subscripts i, j, we introduce the CC array notation $\mathbf{R}$

$$\mathbf{R} = \sum_{k=1}^{N_s} A_k \mathbf{e}(\omega^{(k)}) + \mathbf{N} = \mathbf{E}(\Omega)\mathbf{A} + \mathbf{N} \tag{24}$$

where

$$\mathbf{R} = [\mathbf{r}_1, \ldots, \mathbf{r}_{N_\tau}]^T$$

is the $M = N_n \cdot N_\tau$ element array of the measurements, with

$$\begin{aligned} \mathbf{r}_\tau &= [R(n_0, \tau_0 + \tau - 1), \ldots, R(n_1, \tau_0 + \tau - 1)] \\ \mathbf{e}(\omega^{(k)}) &= \left[\mathbf{s}(1; \omega^{(k)}), \ldots, \mathbf{s}(N_\tau; \omega^{(k)})\right]^T \\ \mathbf{s}(\tau; \omega^{(k)}) &= \Big[S(n_0, \tau_0 + \tau - 1; \omega^{(k)}), \ldots, \\ &\qquad S(n_0, \tau_0 + \tau - 1; \omega^{(k)})\Big] \end{aligned} \tag{25}$$

and

$$\begin{aligned} \mathbf{E}(\Omega) &= [\mathbf{e}(\omega^{(1)}), \ldots, \mathbf{e}(\omega^{(N_s)})] \\ \Omega &= [\omega^{(1)}, \ldots, \omega^{(N_s)}] \\ \mathbf{A} &= [A_1, \ldots, A_{N_s}]^T \end{aligned} \tag{26}$$

and where

$$\mathbf{N} = [\mathbf{n}_1, \ldots, \mathbf{n}_{N_\tau}]^T$$

with

$$\mathbf{n}_\tau = [N(n_0, \tau_0 + \tau - 1), \ldots, N(n_1, \tau_0 + \tau - 1)]$$

It is interesting to note that the different $\mathbf{e}(\omega^{(k)})$ are in general linearly independent but non-orthogonal. The parameter M determines the complexity of the algorithm which increases with the dimension of the observable matrix $\mathbf{R}$.

By neglecting the presence of the interference signal, and under the assumption that the $N_{i,j}(n, \tau)$ terms are independent Gaussian random variables, the probability density function (pdf) of the observables conditioned to the parameters $\mathbf{A}, \Omega$ is

$$p(\mathbf{R}|\mathbf{A}, \Omega) = \left(\frac{1}{\pi\sigma_N^2}\right)^M \exp\left\{-\frac{\|\mathbf{R} - \mathbf{E}(\Omega)\mathbf{A}\|^2}{2\sigma_N^2}\right\} \tag{27}$$

The model order estimation problem can be considered as a multiple hypotheses decision problem. Exploiting the ML criterion, the decision problem consists in finding the number of satellites, N_S, which minimizes the Generalized Log-Likelihood Ratio (GLLR) $J(\Omega, \mathbf{A})$ [33], i.e.

$$(\hat{N}_S, \hat{\mathbf{A}}, \hat{\Omega}) = \min_{N_s} \min_{\mathbf{A}, \Omega} J(\Omega, \mathbf{A}) \equiv \|\mathbf{R} - \mathbf{E}(\Omega)\mathbf{A}\|^2 \tag{28}$$

For given Ω, the optimum $\mathbf{A}$ is given by [32]

$$\hat{\mathbf{A}} = \left(\mathbf{E}(\Omega_a)^H \mathbf{E}(\Omega_a)\right)^{-1} \mathbf{E}(\Omega_a)^H \mathbf{R} \tag{29}$$

Hence, the problem reduces to the minimization of a function $J(\Omega)$ of the only parameter Ω. This approach implicitly leads to the solution of both the problems of detection and estimation of the satellite signal parameters. Nevertheless, an unconstrained ML approach does not work for estimation of dimensionality, since it will always lead to the selection of the highest possible dimension. A complete discussion of this phenomena for generic model order estimation problems are given in [2] [51], [66] and [53]. In order to solve this problem, in each work a solution is proposed, consisting in minimizing a test function which is the sum of the GLLR and of a penalty function growing with the tested model order. The penalty function has the objective of avoiding the ML approach to overestimate the model order.

In [26], an approach which allows to minimize the test function by iteratively testing an increasing model order is presented. The procedure builds upon the observation that, assuming that the set Ω_v of the first $(k-1)$ parameters is known, the k-th parameter $\omega^{(k)}$ can be estimated by minimizing $J(\Omega_a) = J([\omega, \Omega_v])$ w.r.t ω. Accordingly, at the k-th iteration, the set $\Omega_v = (\omega_1, \omega_2, \ldots, \omega_{k-1})$ is defined, and the k-th parameter can be estimated. At each iteration, the model order is increased only if [66]

$$J(\Omega_a) + f(k) < J(\Omega_v) + f(k-1) \tag{30}$$

where $f(k)$ is a linear function of the tested model order k. By observing that [26][27]

$$J(\Omega_a) = J(\Omega_v) - \gamma(\omega; \Omega_v) \tag{31}$$

where

$$\gamma(\omega; \Omega_v) = \frac{|\mathbf{e}^H(\omega) \mathbf{P}^{\perp}_{\mathbf{E}_v} \mathbf{R}|^2}{\|\mathbf{P}^{\perp}_{\mathbf{E}_v} \mathbf{e}(\omega)\|^2} \tag{32}$$

and where

$$\begin{aligned} \mathbf{P}_{\mathbf{E}_v} &= \mathbf{E}_v (\mathbf{E}_v^H \mathbf{E}_v)^{-1} \mathbf{E}_v^H \\ \mathbf{P}^{\perp}_{\mathbf{E}_v} &= \mathbf{I} - \mathbf{P}_{\mathbf{E}_v} = \mathbf{I} - \mathbf{E}_v (\mathbf{E}_v^H \mathbf{E}_v)^{-1} \mathbf{E}_v^H \end{aligned}$$

are the projection matrix onto $\mathrm{Span}(\mathbf{E}_v)$ ($\mathbf{E}_v = \mathbf{E}(\Omega_v)$) and onto its orthogonal complement, respectively, condition (30) can be rewritten as

$$\gamma(\omega; \Omega_v) > f(k) - f(k-1) = \xi \tag{33}$$

that is, the notch periodogram $\gamma(\omega; \Omega_v)$ must be larger than a constant threshold ξ.

This observation leads to the detection algorithm summarized in Algorithm 1. At the k-th iteration, a single signal estimation and detection problem is solved: first, the ML estimation of ω_k is performed

by minimizing the GLLR $J([\omega, \Omega_v])$, or, equivalently, by maximizing $\gamma(\omega; \Omega_v)$ with respect to ω; since no closed form solution for the estimation problem exists, the maximization can be performed by explicitly evaluating the value of $\gamma(\omega; \Omega_v)$ for a discrete set of values. Subsequently, $\gamma(\omega; \Omega_v)$ is compared with a threshold $\xi = C\sigma_N^2$, and, if it is larger, the estimated $\hat{N}_S$ and Ω_v are updated. Accordingly, the number of signals detected as present is equal to the largest model order for which the test is true. It is interesting to note that ξ is a tuning parameter which can be used in order to optimize the trade-off between probability of false-alarm P_{fa}, and probability of detection P_d.

Detection & Estimation;
$\Omega_v = \{\}$;
$\hat{N}_s = 0$;
while $F == 0$ **do**
  $\omega_k = \max_\omega \gamma(\omega; \Omega_v)$;
  $\Omega_a = \{\Omega_v, \omega_k\}$;
  if $\gamma(\omega_k; \Omega_v) > \xi$ **then**
    $\Omega_v = \Omega_a$;
    $\hat{N}_s = \hat{N}_s + 1$;
  else
    $F = 1$;
  end
end

Algorithmus 1 : GNSS Detection algorithm

1.6.2 *GNSS Signals Cross-Correlation Tracking, Cancellation and Interference Detection*

Once the model order has been chosen, the tracking of the GNSS CC components must be performed, which has the objective of refining the estimation of the CC parameters and of updating their values with time. The tracking algorithm is detailed in Algorithm 2.

Since the parameters are initially estimated by explicitly testing a discrete set of values of ω, the accuracy of the estimation is limited by the discretization of the parameters domain. Accordingly, a refinement of the coarse estimations previously carried out is necessary. In this work the estimation is performed by maximizing the parabolic interpolation of the values of $\gamma(\omega, \Omega_v)$ evaluated for three different values of ω. In particular, by defining the set Ω_u, of the updated estimations, and the complementary sets

$$\bar{\Omega}_{u,j} = \{\omega^{(1)}, \ldots, \omega^{(j-1)}, \omega^{(j+1)}, \ldots, \omega^{(k)}\}$$

the evaluation of ω_k, for each k-th satellite ($k = 1, \ldots, N_S$), is performed by maximizing the curve interpolating $\gamma(\omega, \bar{\Omega}_{u,k})$ evaluated at $\omega_k - \delta_\omega, \omega_k, \omega_k + \delta_\omega$. The procedure is repeated until the values of the updated set Ω_u and of the original set Ω_a converge to the same value (within a certain accuracy threshold ϵ).

Once the parameters of the GNSS signals have been accurately estimated, the cancellation of the GNSS signals can be performed by evaluating

$$\mathbf{X} = \mathbf{R} - \mathbf{E}_a \mathbf{A}$$

It is interesting to note that $\mathbf{X}$ is the matrix representation of the signal in which the GNSS components have been canceled, and thus can be efficiently used in order to perform the detection of interference signals and the TDOA parameters estimation.

According to the notation already used, we can write $\mathbf{X}$ as

$$\mathbf{X} = [\mathbf{x}_1, \ldots, \mathbf{x}_{N_\tau}]^T$$

with

$$\mathbf{x}_\tau = [X(n_0, \tau_0 + \tau - 1), \ldots, X(n_1, \tau_0 + \tau - 1)]$$

where $X(n, \tau)$ are the elements of the CC in which the GNSS components have been removed. As it will be shown in Section 1.8, the performance of the cancellation is not uniform, but depends on the value of the time index n_i; in particular, it will be shown that the cancellation error presents a global minimum. Accordingly, by defining $\bar{n}$ as the time index leading to the minimum cancellation error, interference detection is carried out by performing the test

$$\max_\tau X(\bar{n}, \tau) \lessgtr \eta$$

The algorithm is continuously repeated, after updating the observation $\mathbf{R}$ with new measurements, and evaluating the number of detected signals. The number of satellite signal CCs depends on the number of visible satellites which changes over time. The evaluation of the number of satellites can be easily carried out by using the procedure already described for the detection algorithm, described in Section II.A.

It can be observed that the performance of the tracking and cancellation phase strongly depends on the result of the detection phase. In particular, three different cases which lead to different behaviors can be identified: the first is the case in which the detection phase performs correctly and only detects and all the satellite signals: in this case the tracking algorithm can efficiently estimate and cancel all of the GNSS contributions. The second is the case when the detection algorithm detects only some of the satellite signals: accordingly, the tracking algorithm can estimate and cancel only some of the GNSS contributions, thus the interference detection remains affected by the presence of residual GNSS CC peaks. The last case is where the detection algorithm detects at least a component which is not actually present: this case could avoid the convergence of the tracking algorithm, thus reducing the efficacy of the GNSS contribution cancellation.

1.6.3 *Efficient Implementation*

Due to the fact that a bi-dimensional parameter space must be tested (for each satellite signal, $\omega = [\zeta, \varphi]$ must be estimated) and $\gamma(\omega, \Omega_\nu)$

Tracking Cancellation & Interference detection;
while *1* **do**
  Tracking;
  $\Omega_u = \Omega_a$;
  for $k = 1, \ldots, \hat{N}_s$ **do**
    $\omega_k = \arg\max_\omega(\text{Interp}(\gamma(\omega; \bar{\Omega}_{u,k})))$;
    $\Omega_u = \{\bar{\Omega}_{u,k}, \omega_k\}$;
  end
  while $\|\Omega_u - \Omega_a\| > \epsilon$ **do**
    $\Omega_a = \Omega_u$;
    for $k = 1, \ldots, \hat{N}_s$ **do**
      $\omega_k = \arg\max_\omega(\text{Interp}(\gamma(\omega; \bar{\Omega}_{u,k})))$;
      $\Omega_u = \{\bar{\Omega}_{u,k}, \omega_k\}$;
    end
  end
  $\Omega_a = \Omega_u$;

  GNSS cancellation;
  $\mathbf{X} = \mathbf{R} - \mathbf{E}_a\mathbf{A}$;

  Interference Detection;
  if $\max_\tau X(\bar{n}, \tau) > \eta$ **then**
    Interference detected
  end

  update**(R)**;

  Update GNSS signals;
  $\Omega_v = \Omega_a$;
  for $k = 1, \ldots, \hat{N}_s$ **do**
    if $\gamma(\omega_k; \bar{\Omega}_{v,k}) < \xi$ **then**
      $\Omega_v = \bar{\Omega}_{v,k}$;
      $\hat{N}_s = \hat{N}_s - 1$;
    end
  end
  $\omega_k = \max_\omega \gamma(\omega; \Omega_v)$;
  if $\gamma(\omega_k; \Omega_v) > \xi$ **then**
    $\Omega_a = \{\Omega_v, \omega_k\}$;
    $\hat{N}_s = \hat{N}_s + 1$;
  end
end

Algorithmus 2 : GNSS Tracking and Interference Detection algorithm

must be evaluated for a number of discrete hypotheses ω, the computational complexity required in order to execute the proposed algorithm is high. In this section we will detail approaches for efficient, reduced computational implementation of the propsed algorithm. It is worth observing that an efficient implementation for the case of signals characterized by a mono-dimensional parameter $\omega = \varphi$ was proposed in [26]. In this work, the analysis of [26][27] is extended to the case of $\omega = [\zeta, \varphi]$.

1.6.3.1 *Detection & Estiamtion Algorithm*

The detection and estimation algorithm is the most complex part of the proposed algorithm, since, for each satellite signal, a number of different hypotheses must be explicitly tested. The complexity can be reduced by exploiting the Fast Fourier Transform (FFT) algorithm, to calculate in parallel part of the test hypotheses. In the following, a detailed description of the implementation is provided.

At the first iteration ($k = 1$) the calculation of $\gamma(\omega; \Omega_v)$ (with $\Omega_v = \{\cdot\}$) consists of the evaluation of (32) with $\mathbf{P}^{\perp}_{\mathbf{E}_v} = \mathbf{I}$. Therefore, the following calculation must be carried out:

$$\begin{aligned}\gamma(\omega;\Omega) &= \frac{|\mathbf{e}^H(\omega)\mathbf{R}|^2}{\|\mathbf{e}(\omega)\|^2} \\ &= \sum_{n=n_0}^{n_1}\sum_{\tau=\tau_0}^{\tau_1} R(n,\tau)S^*(n,\tau;\omega) \\ &= \sum_{n=n_0}^{n_1}\sum_{\tau=\tau_0}^{\tau_1}\left(R(n,\tau)R_g(\tau-\zeta)\exp\{-j2\pi\varphi n\}\right)\end{aligned} \tag{34}$$

for all the possible values of ω. Noting that the denominator is always equal to 1, since all the $\mathbf{e}(\omega)$ have unitary energy, and observing that some of the terms in [26][27] only depend on the τ variable, the sum can be written as

$$\gamma(\omega;\Omega_v) = \sum_{n=n_0}^{n_1}\left(e^{-j2\pi\varphi n}\sum_{\tau=\tau_0}^{\tau_1} R(n,\tau)R_g(\tau-\zeta)\right) \tag{35}$$

It can be noted that the evaluation of the sum in τ for all the possible values of the variable ζ, corresponds to evaluating the cross-correlation between the two arrays of values. This can be efficiently calculated using the FFT of the two arrays, calculated for the τ variable, i.e.

$$\mathcal{F}_{(\tau)}\{R\}(f,n) = \sum_{\tau} R(n,\tau)e^{-j2\pi f\tau/N_\tau}$$

Exploiting the properties of the Fourier transform, the sum can be evaluated for all the desired values of ζ according to

$$\begin{aligned}Z(\zeta,n) &= \sum_{\tau=\tau_0}^{\tau_1} R(n,\tau)R_g(\tau-\zeta) \\ &= \mathcal{F}^{-1}_{(f)}\left\{\mathcal{F}_{(\tau)}\{R\}(f,n)\mathcal{F}_{(\tau)}\{R_g\}^*(f,n)\right\}(\zeta,n)\end{aligned} \tag{36}$$

Substituting 36 into (35) we obtain

$$\gamma(\omega;\Omega) = \sum_{n=n_0}^{n_1} Z(\zeta,n)e^{-j2\pi\varphi n}$$

and the result can still be calculated in parallel for the hypotheses φ by means of the Fourier transform as

$$\gamma(\omega;\Omega) = \mathcal{F}_{(n)}\{Z(\zeta,n)\}(\zeta,\varphi) \tag{37}$$

The presented procedure allows the parallel computation of all of the values of $\gamma(\omega,\Omega)$ for all the required ζ and φ hypotheses. Therefore, the maximization of the evaluated values with respect to the two parameters can be carried out and the ω_k ($k=1$) value is assigned.

In the following iterations ($k>1$), the calculation of $\gamma(\omega,\Omega)$ imply the calculation of both the numerator and the denominator of (32). The numerator can be evaluated according to procedure similar to the one already described. The only difference is that for $k>1$, $\mathbf{P}^{\perp}_{\mathbf{E}_v} \neq \mathbf{I}$, thus $\mathbf{P}^{\perp}_{\mathbf{E}_v}\mathbf{R}$ must be evaluated, and its result can be used in order to perform the previously described procedure.

On the other hand, it is possible to observe that the denominator of (32) can be written as

$$\|\mathbf{P}^{\perp}_{\mathbf{E}_v}\mathbf{e}(\omega)\|^2 = \|\mathbf{e}(\omega)\|^2 - (\mathbf{E}^H\mathbf{e}(\omega))^H(\mathbf{E}^H\mathbf{E})^{-1}(\mathbf{E}^H\mathbf{e}(\omega))$$

The first term of the difference is the energy of $\mathbf{e}(\omega)$ which is uniformly equal to 1. The second term, instead, depends on ω and must be evaluated for all the possible values of the parameters. It is possible to observe that, at the k-th iteration, we have

$$\mathbf{E}^H\mathbf{e}(\omega) = [\mathbf{e}^H(\omega_1)\mathbf{e}(\omega), \mathbf{e}^H(\omega_2)\mathbf{e}(\omega), \ldots, \mathbf{e}^H(\omega_{k-1})\mathbf{e}(\omega)]^T$$

and that the products until the $(k-2)$-th term have already been calculated at the $(k-1)$-th iteration, for all the values of ω. Therefore, it is possible to iteratively calculate the result, by just evaluating, at the k-th iteration, the values of $\mathbf{e}^H(\omega_{k-1})\mathbf{e}(\omega)$, and by adding them to the previously calculated $(k-2)$ sequences. The evaluation of $\mathbf{e}^H(\omega_{k-1})\mathbf{e}(\omega)$, for all the possible values of ω, can be carried out in parallel by adopting the same procedure proposed for the numerator. That is, an Inverse FFT (IFFT) and two FFTs are used in order to test all the values of ζ, and then an FFT is used in order to test all the values of φ. Once all the the products for all the values of $\omega = [\zeta,\varphi]$ are evaluated, it is possible to calculate the ratio between the numerator and the denominator and to obtain the desired result.

1.6.3.2 *Tracking algorithm*

As shown, the complexity of the detection algorithm is mainly due to the fact that for each signal, the parameters (ζ,φ) must be explicitly tested with a number of different hypothesis values. The tracking algorithm, on the other hand, does not require to test a large number of different hypotheses. At each iteration, for each satellite signal k, the

maximization is performed by maximizing the curve interpolating $\gamma(\omega, \bar{\Omega}_{u,k})$ evaluated at $(\omega_k - \delta_\omega, \omega_k, \omega_k + \delta_\omega)$. In particular, since ω is itself an array of three parameters, three successive maximization of interpolating curves are performed: first, $\gamma(\omega, \bar{\Omega}_{u,k})$ is evaluated for $(\zeta_k - \delta_\zeta, \zeta_k, \zeta_k + \delta_\zeta)$, and the maximization of the interpolating curve leads to the new estimation of ζ_k; subsequently, $\gamma(\omega, \bar{\Omega}_{u,k})$ is evaluated for $(\varphi_k - \delta_\varphi, \varphi_k, \varphi_k + \delta_\varphi)$, and the maximization of the interpolating curve leads to the new estimation of φ_k. Since only three values are evaluated for each maximization, there is no need for parallel implementation, thus, the values can be obtained as simple sums of products.

1.7 SCENARIO AND SYSTEM DESCRIPTION

In this section, a realistic scenario in which the Algorithm can be efficiently applied is described. The scenario consists of a pair of time-synchronized sensor nodes, which receive the GNSS and interference signals, and of a Master Processing Unit (MPU) which performs the described algorithm. In particular we consider:

- three different baselines characterized by receivers separated by a distance $d = 100$, 1000, and 5000m, respectively.
- different values of signal to noise ratio for the GNSS signals. Considering the CC domain, and exploiting the definition given in 1.3 for the equivalent CC to noise ratio, we consider $\left(\frac{E_{cc}}{\sigma_N^2}\right)_{eq}$ ranging from -3 to 3 dB. For each satellite signal CC the same equivalent CC to noise ratio value has been considered. These values have been obtained by considering a Carrier-to-Noise (C/N_0) ratio of 40 dBHz for each satellite signal at each receiver ([31]), a bandwidth equal to 2.7 MHz (from the RF system specifications), and integration periods $T_{cc} = N_{cc}T_s$ ranging from 20ms to 100ms.
- a fixed number of satellite signals $N_S = 10$.
- lag $\zeta_{i,j}^{(k)}$ ranges from $[-\zeta_{MAX}, \zeta_{MAX}]$ and frequency difference $\varphi_{i,j}^{(k)}$ ranges from $[\varphi_{MAX}, \varphi_{MAX}]$; the values of ζ_{MAX} and φ_{MAX} can be derived from Table 3.
- two different values for $ICR = |A_I|^2/|A|^2 = 0, -3$ dB; accordingly, we consider interference CC peaks equal or lower than the GNSS CC peaks, i.e. peaks which could not be detected without the GNSS CC cancellation.
- two different values for $INR = |A_I|^2/\sigma_N^2 = 16, 18$ dB.

Considering the different scenarios, and with the aim of keeping the algorithm complexity unchanged, the following parameters have been selected:

Table 3: Maximum absolute values for ζ, φ for different baselines

Baseline	$\zeta_{MAX} T_s$ [s]	φ_{MAX}/T_s [Hz]
100m	$3.33 \cdot 10^{-7}$	0.1
1000m	$3.33 \cdot 10^{-6}$	1
5000m	$1.67 \cdot 10^{-5}$	5

- $M = N_\tau \cdot N_n = 75 \cdot 65 = 4875$ ($\tau_0 = -37, \tau_1 = 37$ and ($n_0 = -32, n_1 = 32$)); the parameter sets the dimension of the observable and, accordingly, the complexity of the algorithm.
- $N_\tau = 75$ ($\tau_0 = -37, \tau_1 = 37$) and sampling frequency $f_s =$ 16.37MHz, 8.18MHz and 2.04MHz, for the 100m, 1000m and 5000m baselines, respectively: these parameters determine the range of the observable lags which satisfies $N_\tau/f_s \geqslant 2\zeta_{MAX}$.
- $N_n = 65$ ($n_0 = -32, n_1 = 32$) and $f_R = 1/T_R$= 0.2, 2 and 10 Hz, (T_R= 5, .5 and .1 sec) for the 100, 1000, and 5000m baselines, respectively: since the Fourier transform is used in order to test the different frequencies, increasing the number of observations allows decreasing the distance between two successive independent frequency hypotheses.
- $T_0 = N_n/f_R = 320$, 32 and 6.4 seconds, for the 100m, 1000m, and 500m baselines, respectively.

The presented values are collected in Table 4

Table 4: Algorithm parameters

Baseline	f_s [MHz]	f_R [Hz]	T_0 [s]
100m	16.37	0.2	320
1000m	8.18	2	32
5000m	2.04	10	6.4

In the following, the numerical results for the different case studies are shown, for the three analyzed baselines.

1.8 PERFORMANCE EVALUATION

In this section, the performance analysis of the proposed algorithm is carried out. Since the algorithm is executed in multiple successive steps, different figures of merit are used in order to characterize the performance. The GNSS CC components detection performance is evaluated in terms of probabilities of detection (P_d), false alarm (P_{fa}), and error (P_e), whereas the accuracy of the parameter estimation algorithm is evaluated considering the Mean Square Error (MSE) of the parameters. The cancellation is measured considering the power of the residual of the CC components after cancellation. Finally, the interference detection is measured in terms of probabilities of detection and false alarm. In the following, detailed results are presented.

1.8.1 *GNSS Satellite Cross-Correlation Detection performance*

Since the GNSS CC detection algorithm is performed iteratively, at each iteration either at least one satellite signal is present and can be detected, or all the satellite signals have been detected and canceled and no GNSS CC components remain. Accordingly, different probabilities can be defined, depending on the possible events happening under the two hypotheses. When at least one satellite signal is present, three disjoint events are possible:

- *correct detection*: all and only the satellite signals are detected with probability P_d;
- *missed detection*: not all, but only satellite signals are detected with probability P_{md};
- *error*: at least one non-satellite signal is detected with probability P_e;

On the other hand, when all the satellite signals have been removed, the following events are possible:

- *false alarm*: at least one signal is detected with probability P_{fa};
- *correct rejection*: no signals is detected with probability P_{cr};

It must be noted that $P_d + P_{md} + P_e = 1$ and $P_{fa} + P_{cr} = 1$. In general, a closed form expression for the described probabilities cannot be found, since the accurate detection of the GNSS signals requires a large number of hypotheses which in general are non-orthogonal. Consequently, the performance is evaluated numerically considering the scenario and the algorithm parameters described previously, and running a campaign of Monte Carlo simulations with 10^4 repetitions. In Fig. 7 the probabilities of false alarm P_{fa}, missed detection P_{md} and error P_e are shown with respect to the threshold values $C = \xi/\sigma_N^2$, for the 100m, 1000m, and 5000m baselines, and considering a worst case scenario with $E_{cc}/\sigma_N^2 = 0$. It is to note that all the GNSS CC components have been generated with the same equivalent signal to noise ratio. As can be observed from Fig. 7, in the 100m baseline P_{fa} rapidly decreases with increasing threshold, while P_{md} rapidly increases, P_e reaches $1.8 \cdot 10^{-1}$ in the low threshold region, and, accordingly, P_d is never larger than 0.82. Both the large P_e and the rapidly growing P_{md} are due to the fact that in the 100m baseline the CC components are strongly correlated, thus, at every iteration, all the GNSS CC components energies are reduced, and, consequently, the probability of being detected decreases. Furthermore, due to the presence of noise, when the CC components are erroneously (but inevitably!) removed, spurious components are detected and P_e increases.

The performance strongly improves in the 1000m baseline: in this case P_{fa} rapidly decreases with increasing threshold C, P_{md} remains low ($< 10^{-2}$) for $C < 35$, and P_e is equal to 0. This result shows that there is a large region of values of C, which guarantees P_{fa} and P_{md} to be lower than 10^{-2}. It is also possible to observe that P_{fa} is slightly

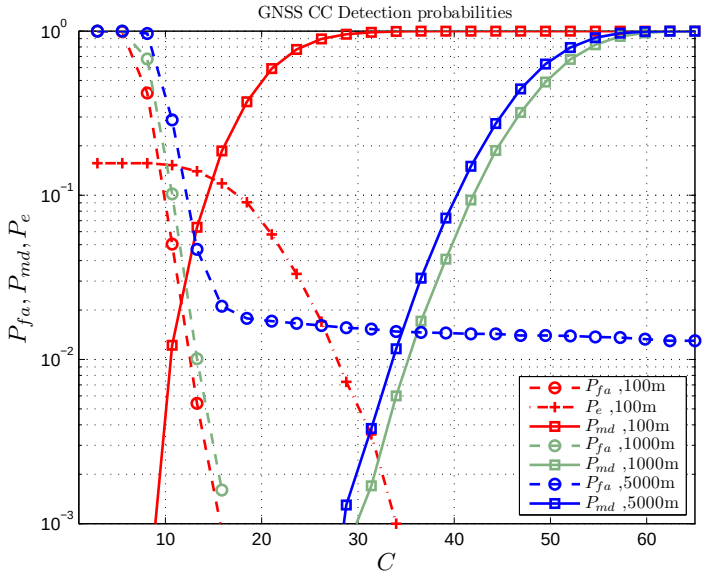

Figure 7: Probability of false alarm, missed detection and error

larger than the false alarm rate in the 100m baseline. This behavior can be justified by observing that the calculation of (36) corresponds to the application of a filter with pulse response $R_g(\tau)$ to the function $R(n,\tau)$. Since $R_g(\tau)$ is different for the three baselines (due to the considered sampling frequencies) different results are obtained. In particular $R_g(\tau)$ operates as a low-pass filter with a normalized bandwidth increasing with the baseline, which leads to noise level growing from the shortest to the longest baseline.

Accordingly, the P_{fa} performance further increases in the 5000m baseline. In this case the normalized bandwidth of $R_g(\tau)$ further increases, and, accordingly, the noise level and the P_{fa} increase. A slight difference can be observed also for P_{md} which increases with respect to the 1000m baselines, still due to increased normalized bandwidth of $R_g(\tau)$. However, a large range of values of C ($20 < C < 30$) guaranteeing P_{fa} and P_{md} in the order of 10^{-2} can still be identified, and accordingly good detection capabilities can be reached.

In conclusion, the performance of the detection algorithm depends on the trade-off between the effects of the correlation between the GNSS CC components and of the low-pass filtering due to the shape of $R_g(\tau)$. It is shown how, particularly in the case of long baselines, the reliability of the detection algorithm remains high for a large set of values of C ($P_{fa}, P_{md}, P_e \ll 10^{-1}$).

1.8.2 *Parameters Estimation Accuracy*

The capabilities of the tracking algorithm have been measured by evaluating the MSE of the parameter estimation algorithm. Since in the case where multiple GNSS CC components are present, the MSE assumes different values according to the correlation between the components, in the following the parameter estimation capability is evaluated considering the presence of only one satellite signal ($N_s = 1$). In

Fig. 8 the MSE of the estimation of the parameters ζ, ϕ and of the absolute value $|A|$ is shown with respect to the equivalent signal to noise ratio for the three different baselines, and it is compared with the corresponding Cramer-Rao Bound Cramer Rao Bound (CRB). The fig-

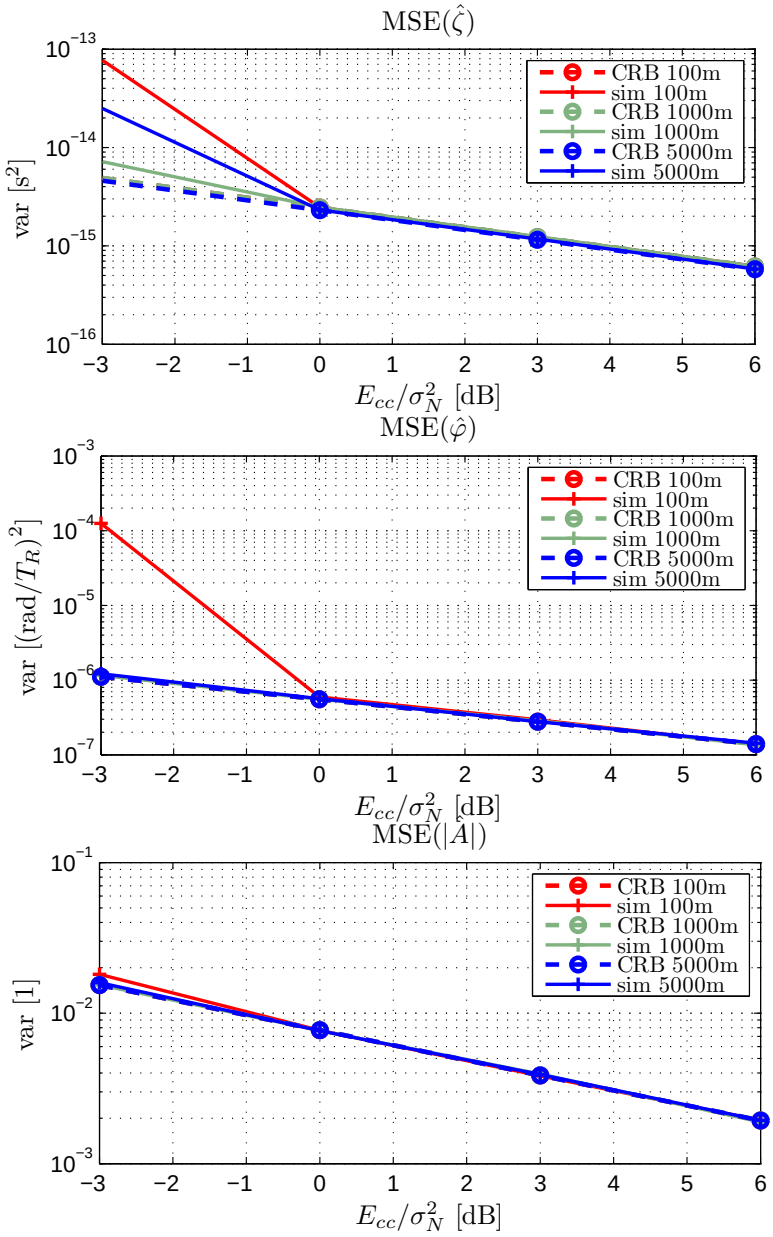

Figure 8: CRB of the GNSS signal parameter estimations vs. equivalent signal to noise ratio. One satellite ($N_s = 1$) is considered in order to evaluate the performance.

ures show that the proposed estimator is efficient, since the variance of the estimation errors converges to the CRB, for all the considered parameters. It is interesting to note that around the $E_{cc}/\sigma_N^2 = 0$ value, the threshold effect typical of the estimation problems appears. This means that for lower E_{cc}/σ_N^2 values the estimator accuracy diverges

rapidly. Looking at the variance of the $\hat{\zeta}$ estimation error in Fig. 8 it is possible to note that, for $E_{cc}/\sigma_N^2 \geqslant 0$, the values are always lower than 10^{-14}, meaning that the error is always much lower than the width of the $R_g(\tau)$ function support ($\simeq 2\mu s$ for the GPS case). The variance of the error of the $\hat{\varphi}$ and $|\hat{A}|$ estimations is limited to less than 10^{-6} and 10^{-2}, respectively, thus demonstrating the high accuracy of the proposed approach.

Since in the case of multiple signal components the estimation is affected by the linear dependence between the CC components, the performance tend to worsen. In this case, the presented curves do not describe the actual behavior of the estimation errors, but provide an effective evaluation of the performance bounds.

1.8.3 *GNSS Cross-Correlation Cancellation Error*

The performance of the cancellation algorithm is characterized considering the MSE of the estimation of the values of the GNSS CC over the considered support $[\tau_0, \tau_1] \times [n_0, n_1]$:

$$\epsilon(n,\tau) = E\left[\left|\sum_{k=1}^{\hat{N}_s}\left(\hat{A}_k S(n,\tau;\hat{\omega}^{(k)}) - A_k S(n,\tau;\omega^{(k)})\right)\right|^2\right] \quad (38)$$

where $\hat{A}_k, \hat{\omega}^{(k)}$ are the estimated values for the parameters, and $E[\cdot]$ is the statistical mean value. Also in this case, an analytical description of the behavior of the error cannot be carried out, thus the performance has been evaluated by means of numerical simulations. As for the case of the parameter estimation, the single satellite case is considered, since it shows the performance of the cancellation algorithm avoiding the effects of the linear dependence between the CC components.

The behavior of the error $\epsilon(n,\zeta)$ ($\tau = \zeta$ corresponds to the actual lag difference) is shown in Fig. 9, 10, and 11 for the three different baselines, and for different Signal-to-Noise Ratio (SNR) values. The results have been obtained by averaging the error over 10^5 iterations. The figures show that, for all the baselines, the error presents minimua iat $n = 0$ and grows symmetrically with the increasing absolute value of n. It is also worth observing that a difference is present between the curves obtained for the three different baselines. In particular it is possible to observe that the error is minimum in the 100m baseline ($\epsilon(0,\zeta) \simeq 3 \cdot 10^{-3}$, for $\bar{n} = 0$ in the $E_{cc}/\sigma_N^2 = -3$dB case) and grows for larger baselines ($\epsilon(0,\tau) \simeq 5 \cdot 10^{-3}$ and $\epsilon(0,\tau) \simeq 2 \cdot 10^{-2}$ for the 1000m and 5000m baselines, respectively). As for the the previous results, this behavior can be explained by considering the fact that, due to the different sampling frequencies, $R_g(\tau)$ strongly filters the noise in the 100m case, but the effect is weaker for longer baselines.

The position of the minima is always at $n = 0$, for all the analyzed cases, thus $n = 0$ can be chosen as the optimal time instant for the cancellation. Identifying the optimum time instant as $\bar{n} = 0$, the cancellation performance along the lag domain $\epsilon(\bar{n},\tau)$ is shown in Fig.

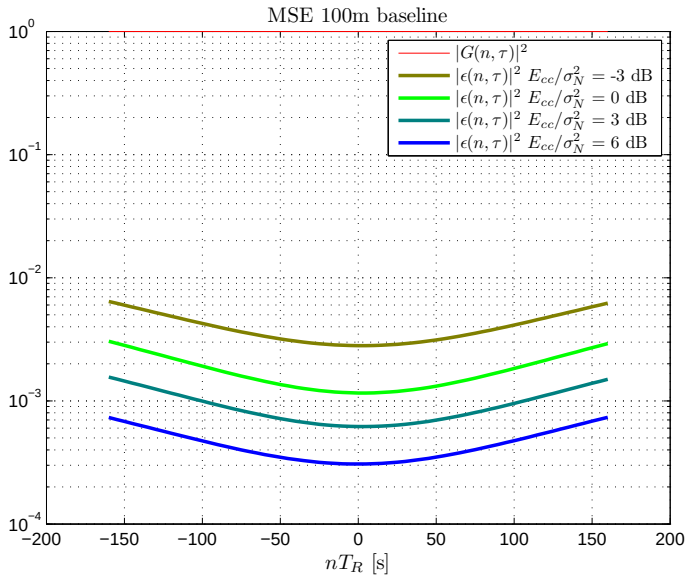

Figure 9: MSE @ different C/N values in case of absence of Doppler rate uncertainty

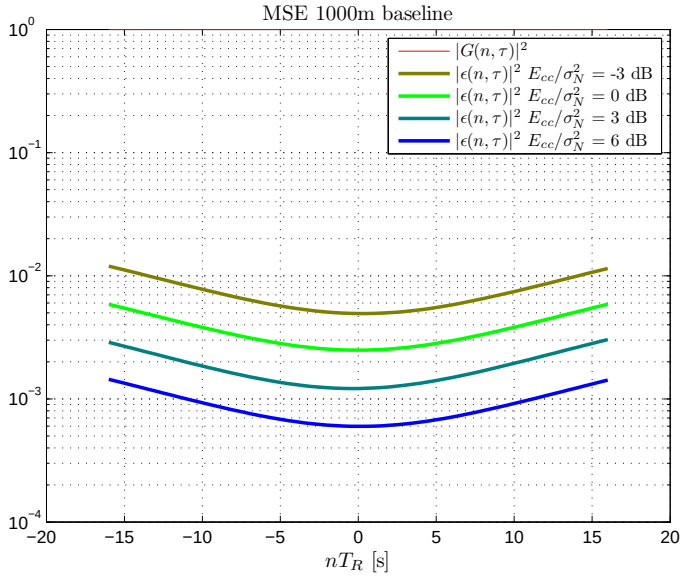

Figure 10: MSE @ different C/N values in case of absence of Doppler rate uncertainty

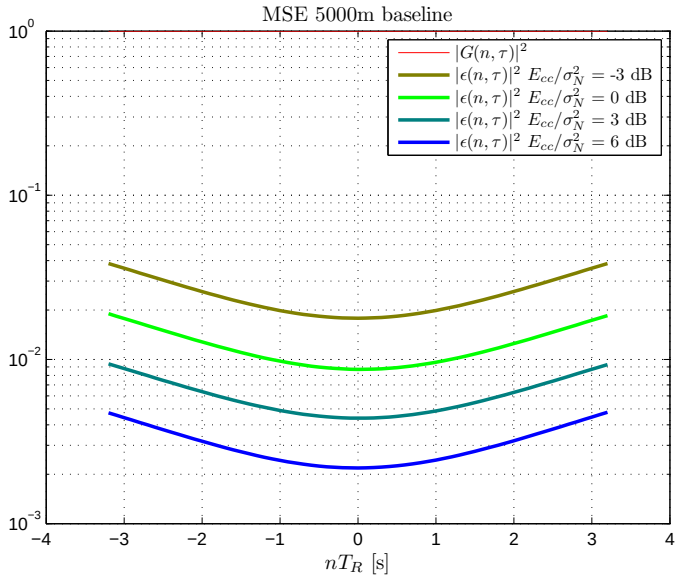

Figure 11: MSE @ different C/N values in case of absence of Doppler rate uncertainty

12, 13 and 14, for a scenario in which up to 10 satellite signals are received at the sensor nodes. The results are summarized in Table III for different baselines and E_{CC}/σ^2 No values. It is interesting to note that the residual error function is the only deterministic source of uncertainty for the interference detection task, thus good cancellation helps improving the interference identification.

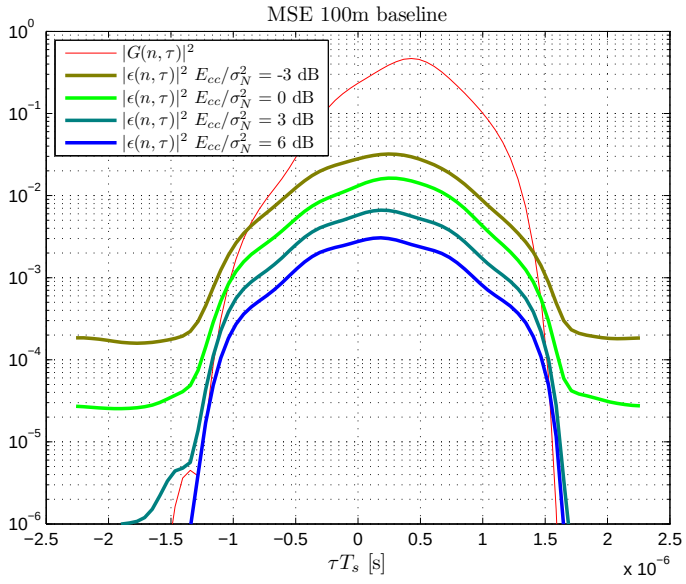

Figure 12: MSE @ different C/N values: 100m baseline

The results show that the error increases in correspondence of the actual GNSS CC peaks, and decreases when the CC decreases. In particular, in the 100m baseline, as shown in Fig. 12, the different GNSS CC components give origin to a unique peak which is effectively canceled, leading to a residual which is more than one order of magni-

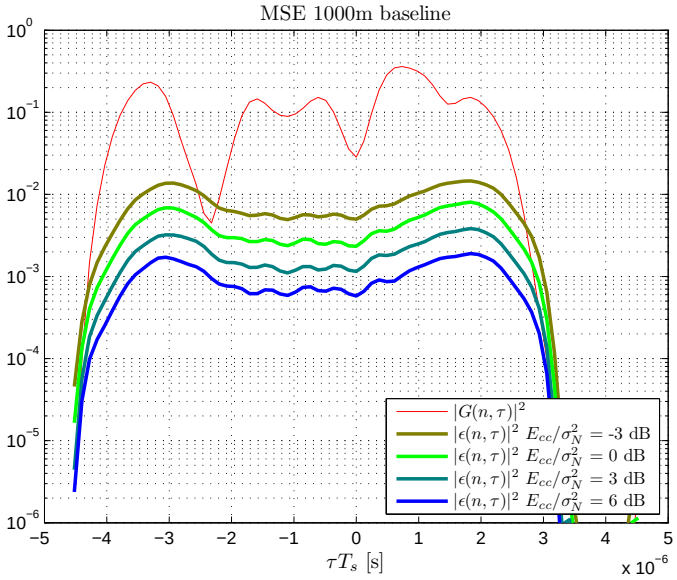

Figure 13: MSE @ different C/N values: 1000m baseline

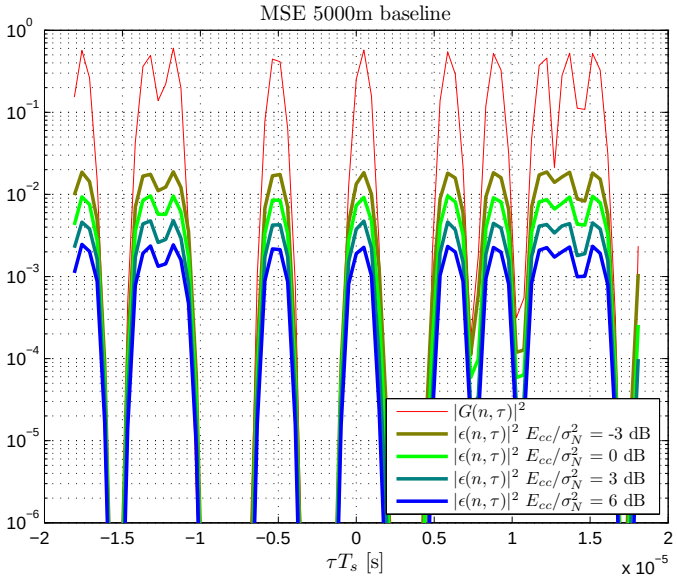

Figure 14: MSE @ different C/N values: 5000m baseline

tude lower than the actual CC in the worst case ($E_{cc}/\sigma_N^2 = -3$dB), as reported in Table 5, as well. The decrease of the cancellation performance w.r.t the single satellite case is evident, and it is due to the linear dependence between the CC components, which being non-orthogonal, worsen the estimation accuracy. The cancellation performance improves in the 1000m and 5000m baselines, since in these cases the CC components are less correlated (as can be observed from Fig. 13, the different peaks become distinguishable, and in Fig. 14 they completely resolve). Accordingly, in the worst case, the ratio between the residual peak and the CC peak reduces to -14dB and -15dB, in the 1000m and 5000m baselines respectively. According to the shown cancellation performance, the power at which interference signals can be detected can be lowered by more than 10dB.

Table 5: peak to peak cancelation figure [dB]

	E_{cc}/σ_N^2 [dB]			
Baseline	-3	0	3	6
100m	-11.6	-14.6	-18.5	-21.8
1000m	-13.9	-16.5	-19.7	-22.8
5000m	-15.0	-18.0	-21.0	-23.9

1.8.4 *Interference Detection*

Finally, the interference detection performance is shown. Similarly to the satellite signal CC detection, the following probabilities are evaluated:

- probability of false alarm P_{fa}, which is the probability of detecting an interference signal when no interferers are present.
- probability of correct rejection P_{cr}, which is the probability of avoiding the detection of any signal, given that no interferers are present.
- probability of missed detection P_{md}, defined as the probability of missing the detection of any signal given that one interferer is present.
- probability of detection P_d, defined as the probability of detecting the correct interference CC peak, that is a CC peak corresponding to a lag $\hat{\zeta}$ belonging to the H_1 region $H_1 = \{\zeta : |\hat{\zeta_I} - \zeta_I|T_s < \xi_\zeta\}$, with ζ_I the actual lag of the interference CC. In particular, the threshold $\xi_\zeta = 0.5 \cdot 10^{-6}$ sec is chosen.
- probability of error P_e, defined as the probability of detecting a wrong interference CC peak, that is an CC peak corresponding to a lag $\hat{\zeta}$ belonging to the H_0 region $H_0 = \{\zeta : |\hat{\zeta_I} - \zeta_I|T_s > \xi_\zeta\}$.

Since $P_{fa} + P_{cr} = 1$ and $P_{md} + P_e + P_d = 1$, in the following only the P_{fa}, P_{md} and P_e probabilities are evaluated. In Fig. 15 the Receiver

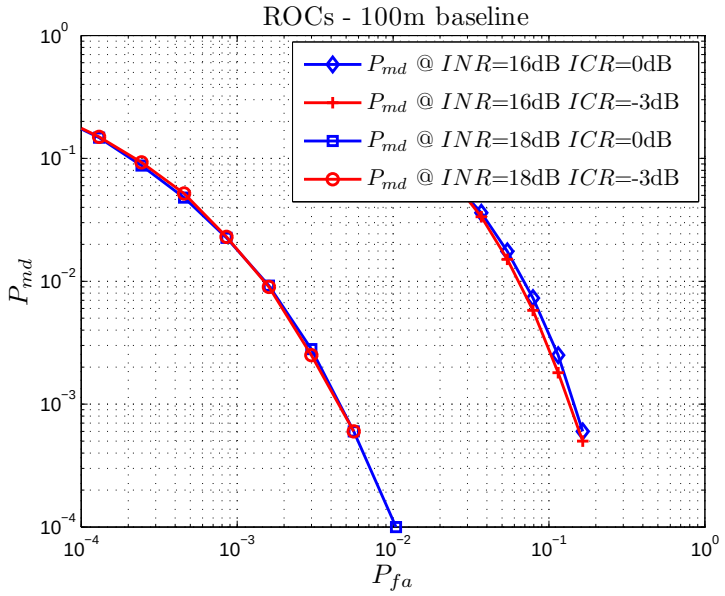

Figure 15: Interference Detection ROCs. 100m baseline

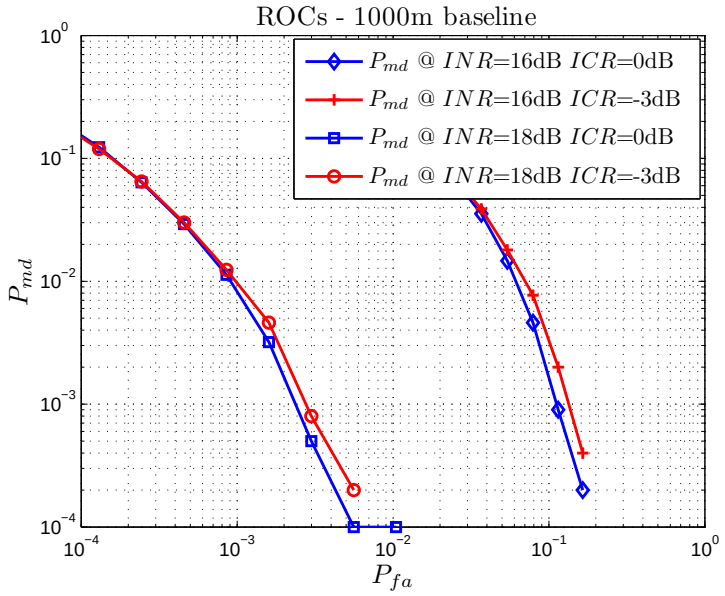

Figure 16: Interference Detection ROCs. 1000m baseline

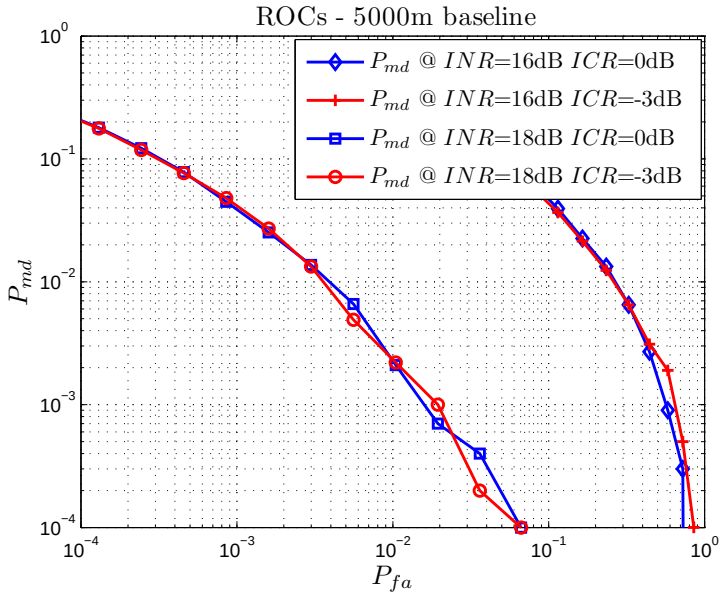

Figure 17: Interference Detection ROCs. 5000m baseline

Operating Characteristics (ROC) are shown for the 100m baseline, for the case of INR = 16dB and ICR = 0dB and 3dB. As can be seen, the P_{md} and P_{fa} probabilities are both limited to less than $2 \cdot 10^{-2}$. The curves also demonstrate that the cancelation performs very well since the curves are practically identical, meaning that the effect of the residual on the interference detection is very limited. A similar behavior is also shown in Fig. 16 and 17, for the 1000m and 5000m baselines. In these cases the curves obtained under the ICR = 0dB and ICR = −3dB are practically identical. However, it is also possible to observe that for longer baselines the P_{fa} and P_{md} probabilities increase, mainly due to the fact that given reduced sampling frequency f_s, the number of samples belonging to the H_1 region is also reduced, hence resulting in increased the detection capability.

It must be noted that these probabilities are obtained after the removal of the satellites signal CC components, which otherwise would be as large as the interference CC peak itself (in the ICR = 0 dB), or even larger (in the ICR = −3 dB), thus making the detection practically not possible and clearly demonstrate the efficacy of the proposed approach.

1.9 CONCLUSIONS

In this chapter, we analyzed the behavior of the cross-correlation between the signals received at spatially-separated time-synchronized sensor nodes in case GNSS satellite signals and an interference signal are received embedded in noise. We described the behavior of the GNSS signals CC function through a closed form expression.The accuracy of the GNSS model has also been proved by comparing the numerically evaluated CC function and the corresponding analytical expression. We detailed a technique for enhancing the interference detection and TDOA localization based on the analysis of the CC of

signals received at spatially separated, time-synchronized nodes, and analyzed its performance. The algorithm is performed in successive steps and consists of first detecting the GNSS CC contributions, then estimating their characteristic parameters and finally removing the estimated components. The aim is reducing the minimum detectable interference power which is generally limited by level of the GNSS CC itself. The effectiveness of the proposed approach is demonstrated by a complete analysis carried out by means of simulations for three realistic scenarios characterized by receivers separated by different baselines. The most critical aspect is due to the correlation between the GNSS CC components, which can reduce the detection performance and the accuracy of the estimations/cancellation phase. This aspect is mostly visible for short baselines, for which the different satellite components are strongly correlated, and reduces with increasing distances between the sensor nodes. The detection performance guarantees good results, also for low signal to noise ratios, thus correctly enabling the estimation phase. The proposed estimator is highly accurate, allowing proper cancellation of the GNSS contributions. The level of the minimum detectable interference can be strongly reduced, and results to be practically independent on the level of the GNSS CC components before the removal.

2

GNSS INTERFERENCE CANCELLATION

2.1 INTRODUCTION

As discussed in the previous chapter, a major threat for GNSS systems is represented by attacks from jamming devices, i.e., devices which aim at interfering and disrupting GNSS services. In most of the cases, this is achieved by means of so-called personal privacy devices, i.e., jamming devices which attempt to obscure the satellite signal(s) [6], [22]. In order to guarantee the reliability of GNSS-based applications against jamming devices, advanced interference management techniques need to be designed.

The vast majority of the previous work on the subject focuses on the detection/localization of interfering signals, while their mitigation/-cancellation are still in their infancy. Recently, several measurement campaigns have been performed to gain knowledge on the nature of jamming signals [36], [22]. The outcomes of these studies clearly show that most of the interfering signals exhibit quasi-periodic waveforms with particular autocorrelation functions, resulting from their generation by frequency/phase modulation through periodic signals (in the following these interferers will be identified as structured). Such a structure can be efficiently exploited in order to properly design procedures for interfering signals cancellation [9].

So far, the approaches proposed in the literature sporadically exploit the knowledge of the structure of interfering signals. In [47], [4] and [35] techniques are presented, based on time pulse blanking and on wavelet decomposition, adapted to the particular case of pulsed interference. In [21][23][52], a ML approach is proposed, where the likelihood of the received signal with respect to a given template depending on a set of parameters is computed. However, a signal template is often unlikely to be available. In order to circumvent this problem, the received signal might be projected onto a set of base vectors, allowing to select the most significant signal components. In this category, notable approaches rely on Short-Time Fourier Transform (STFT) [3] , and Wavelet Transform (WT) [37], [17]. The drawback of this approach is related to the sparseness of the signal in the analyzed domains, i.e., the signal energy is uniformly distributed over the considered domain. Thus, more complex approaches can be envisaged, as Principal Component Analysis (PCA) [25] and Cyclic Autocorrelation Feature Analysis [44]. However, these approaches are computationally extensive.

In this chapter, we try to move away from the above cited limitations, and propose a solution which allows us to cope with all the interfering signals generated by carrier modulation through periodic signals. The same algorithm is also presented in [P4].

The rest of this chapter is organized as follows. In Section 2.2, the system model is introduced. In Section 2.3, the proposed algorithm is presented. In Section 2.4, the numerical results are shown. Concluding remarks are provided in Section 2.5.

2.2 SYSTEM MODEL

We consider a received signal given by $r(t) = s(t) + n(t)$, where $s(t)$ is the received interfering signal and $n(t)$ is the AWGN (in this section we neglect the GNSS signals and focus the attention of interference). The interference signal can be represented according to the following general model:

$$s(t) = A(t)\exp\left[j(2\pi f_0 t + \phi(t))\right] \tag{39}$$

with

$$\phi(t) = 2\pi \int_0^t z(\xi)d\xi \tag{40}$$

for Frequency Modulated (FM) signals and

$$\phi(t) = z(t) \tag{41}$$

for Phase Modulated (PM) signals. The peculiarity of jammer interference signals is that they are generated by modulating the frequency/phase of a sinusoidal carrier signal by a generic periodic signal $z(t)$, with repetition period denoted by T [36]

$$z(t) = \sum_{k=-\infty}^{+\infty} z_0(t - kT) \tag{42}$$

with $z(t) \neq 0$ only for $t \in [0, T]$. Assuming that the signal amplitude is constant inside each repetition period, we can write:

$$A(t) = A_k \text{for} \quad t \in [kT, (k+1)T[\tag{43}$$

and thus the signal can be rewritten as:

$$s(t) = \sum_{k=-\infty}^{+\infty} A_k s_0(t - kT) e^{j\Phi_k} \tag{44}$$

with

$$s_0(t) = \begin{cases} \exp\left\{j2\pi\left[f_0 t + \int_0^t z_0(\xi)d\xi\right]\right\} & t \in [0, T[\\ 0 & \text{oth.} \end{cases} \tag{45}$$

and

$$\Phi_k = 2\pi\left[f_0 kT + k\int_0^T z_0(\xi)d\xi\right] \tag{46}$$

for the FM case, and

$$s_0(t) = \begin{cases} \exp\{j2\pi[f_0 t + z_0(t)]\} & t \in [0, T[\\ 0 & \text{oth.} \end{cases} \tag{47}$$

and

$$\Phi_k = 2\pi f_0 kT \tag{48}$$

for the PM case. This property basically states that structured interferers have a characteristic waveform which is repeated in time. Thus, an estimation of the signal waveform can be performed by exploiting information on this structure, as shown in the following sections.

2.3 ALGORITHM DESCRIPTION

2.3.1 *Waveform Acquisition*

In this first stage the repetition period T of the modulating signal is estimated exploiting the autocorrelation properties of the structured interferes, and a snapshot of duration equal to the estimated period is selected and exploited as local signal replica.

Let us denote by $r(k)$ the time-discrete received signal at the output of the sampler. The algorithm is performed according to the pseudo-code reported in Algorithm 1. In order to correctly estimate the repetition period T, an observation period longer than T must be considered. Accordingly, after interference detection, a signal trace $r(k) \quad (k = 1, \ldots, M)$ is stored. Then, the autocorrelation function $R(m)$ for the stored signal is calculated, for a discrete set of lags $m \in \{0, \ldots, M_{lag}\}$, with $M_{lag}T_s > T$, and the period of the interfering signal is estimated selecting the value $\hat{T} = \hat{m}T_s$, corresponding to the maximum of the absolute value of the real part of $R(m)$. Using the estimated period, the local signal replica $\mathbf{l}$ is built, by storing a track of signal of length equal to the estimated repetition period $\hat{l}$:

$$\bar{\mathbf{l}} = \left\{ r(k) : 0 < kT_s < \hat{T} \right\} \tag{49}$$

Interference Signal Waveform Acquisition;
$R(m) = \frac{1}{M} \sum_{n=1}^{M} r(n) r(n+m)^*$;
$\hat{m} = \max_m |R(m)|$;
$\mathbf{l} = [r(1), r(2), \ldots, r(\hat{m})]$;
Algorithmus 3 : Interference Signal Waveform Acquisition

2.3.2 *Waveform Tracking and Cancellation*

After the selection of the repetition period and the construction of the local signal replica, the interfering signal is tracked with an open-loop like tracking circuit, which operates according to the ML criterion; successively the local signal replica is updated, in order to eliminate the contribution of both thermal noise and of the GNSS signals, and cancellation is performed. These tasks are performed according to the pseudo-code reported in Algorithm 4. At each repetition period, delay $D = kT$, phase Φ and amplitude A, are first estimated. In order to perform this task, N_D delayed versions of the received signal (in the

shown algorithm, we consider the $N_D = 5$ very-Early, Early, Prompt, Late and very-Late versions $[\mathbf{R}_{EE}, \mathbf{R}_E, \mathbf{R}_P, \mathbf{R}_L, \mathbf{R}_{LL}]$), with a time spacing of one sample, are considered. Accordingly, indicating with $\langle \cdot, \cdot \rangle$ the scalar product of two complex vectors, the ML phase estimates

$$[\Phi_{EE}, \Phi_E, \Phi_P, \Phi_L, \Phi_{LL}]$$

are carried out, according to

$$\Phi_i = \angle\langle \mathbf{r}_i, \mathbf{l} \rangle \qquad i \in \{EE, E, P, L, LL\} \tag{50}$$

thus using the previously calculated local signal replica $\mathbf{l}$. Then, the likelihood function $\mathbf{\Lambda}$ for the joint delay and phase hypotheses is evaluated; by maximizing $\mathbf{\Lambda}$, the delay D, and the phase Φ estimates are carried out, and the time aligned received signal $\mathbf{r}$ is selected. Successively, the estimation of the amplitude A is performed according to the ML criterion. Once these parameters are available at each repetition period, the basic waveform $s_0(n)$ can be estimated. Finally, the local signal replica $\mathbf{l}$ is updated, by averaging the last L successive estimations of the basic waveform . At each repetition period, the estimated interfering signal $\hat{\mathbf{s}} = [\hat{s}(1), \ldots, \hat{s}(\hat{m})]$ can be represented as:

$$\hat{\mathbf{s}} = A\mathbf{l}e^{j\Phi} \tag{51}$$

Thus, cancellation can be performed by simply subtracting the estimated signal from the received signal, in order to obtain the interference-free signal :

$$\hat{\mathbf{r}} = \mathbf{r} - \hat{\mathbf{s}} \tag{52}$$

The choice of limiting the number L of successive estimations to be considered for the local replica estimation is due to the fact that, in this way, signals with parameters which are slowly variable in time can be tracked as well (for example, a change of the transmitter or receiver temperature might cause oscillators to modify the generated frequency). By canceling the interferer signal, and thus reducing the jamming power, the reliability of the GNSS transmissions is obviously increased.

2.4 NUMERICAL RESULTS

The proposed algorithm has been tested by means of both numerical simulations carried out considering synthesized signals generated according to the model of equations (1)-(4), and emulations with real jamming signals registered within a controlled environment. Since GNSS signals are in general much weaker than the thermal noise, and consequently of the interfering signals as well, in the proposed framework performance has been evaluated taking into account the interfering signal embedded in thermal noise only. The results can be easily shown to be equivalent.

Interference Signal Waveform Tracking and Cancellation;
$D = \hat{m}$;
while *1* **do**
$\mathbf{r}_{EE} = [r(D-2), r(D-1), \ldots, r(D+\hat{m}-2)]$;
$\mathbf{r}_{E} = [r(D-1), r(D), \ldots, r(D+\hat{m}-1)]$;
$\mathbf{r}_{P} = [r(D), r(D+1), \ldots, r(D+\hat{m})]$;
$\mathbf{r}_{L} = [r(D+1), r(D+2), \ldots, r(D+\hat{m}+1)]$;
$\mathbf{r}_{LL} = [r(D+2), r(D+3), \ldots, r(D+\hat{m}+2)]$;

$$\mathbf{p} = \begin{bmatrix} \Phi_{EE} \\ \Phi_{E} \\ \Phi_{P} \\ \Phi_{L} \\ \Phi_{LL} \end{bmatrix} = \begin{bmatrix} \angle\langle \mathbf{r}_{EE}, \mathbf{l} \rangle \\ \angle\langle \mathbf{r}_{E}, \mathbf{l} \rangle \\ \angle\langle \mathbf{r}_{P}, \mathbf{l} \rangle \\ \angle\langle \mathbf{r}_{L}, \mathbf{l} \rangle \\ \angle\langle \mathbf{r}_{LL}, \mathbf{l} \rangle \end{bmatrix} ;$$

$$\boldsymbol{\Lambda} = \begin{bmatrix} \Lambda_{EE} \\ \Lambda_{E} \\ \Lambda_{P} \\ \Lambda_{L} \\ \Lambda_{LL} \end{bmatrix} = \begin{bmatrix} \Re\left\{ \langle \mathbf{r}_{EE}, \mathbf{l} \rangle \, e^{-j\Phi_{EE}} \right\} \\ \Re\left\{ \langle \mathbf{r}_{E}, \mathbf{l} \rangle \, e^{-j\Phi_{E}} \right\} \\ \Re\left\{ \langle \mathbf{r}_{P}, \mathbf{l} \rangle \, e^{-j\Phi_{P}} \right\} \\ \Re\left\{ \langle \mathbf{r}_{L}, \mathbf{l} \rangle \, e^{-j\Phi_{L}} \right\} \\ \Re\left\{ \langle \mathbf{r}_{LL}, \mathbf{l} \rangle \, e^{-j\Phi_{LL}} \right\} \end{bmatrix} ;$$

$$(D, \phi) = \begin{bmatrix} (D+M-2, \Phi_{EE}) & \textbf{if} & \max(\boldsymbol{\Lambda}) = \Lambda_{EE} \\ (D+M-1, \Phi_{E}) & \textbf{if} & \max(\boldsymbol{\Lambda}) = \Lambda_{E} \\ (D+M, \Phi_{P}) & \textbf{if} & \max(\boldsymbol{\Lambda}) = \Lambda_{P} \\ (D+M+1, \Phi_{L}) & \textbf{if} & \max(\boldsymbol{\Lambda}) = \Lambda_{L} \\ (D+M+2, \Phi_{LL}) & \textbf{if} & \max(\boldsymbol{\Lambda}) = \Lambda_{LL} \end{bmatrix} ;$$

$$\mathbf{r} = \begin{bmatrix} \mathbf{r}_{EE} & \textbf{if} & \max(\boldsymbol{\Lambda}) = \Lambda_{EE} \\ \mathbf{r}_{E} & \textbf{if} & \max(\boldsymbol{\Lambda}) = \Lambda_{E} \\ \mathbf{r}_{P} & \textbf{if} & \max(\boldsymbol{\Lambda}) = \Lambda_{P} \\ \mathbf{r}_{L} & \textbf{if} & \max(\boldsymbol{\Lambda}) = \Lambda_{L} \\ \mathbf{r}_{LL} & \textbf{if} & \max(\boldsymbol{\Lambda}) = \Lambda_{LL} \end{bmatrix} ;$$

$A = \frac{\Re\{\langle \mathbf{r}, \mathbf{l} \rangle e^{-j\Phi}\}}{\langle \mathbf{l}, \mathbf{l} \rangle}$;
$\mathbf{l} = \text{mean}(\mathbf{l}, \mathbf{r}, L)$;
end

Algorithmus 4 : Interference Signal Waveform Tracking and Cancellation

2.4.1 *Simulations*

In the simulations setup, interfering signals of different types have been considered. In particular: chirp, single-tone and Direct Sequence Spread Spectrum (DS-SS) signals. The characteristic parameters are listed in Table 6. The considered interference to noise power ratio J/N has been considered equal to 0 dB.

Table 6: Interfering Signal Parameters

Chirp Jammer		
Repetition Period	T	10 µs
Min/Max frequencies	(f_{min}, f_{max})	$(f_{LI} - 10, f_{LI} + 10)$ MHz
Single Tone Jammer		
Carrier Frequency	$f_c(T)$	$f_{LI} + 0.5$MHz (2µs)
Spread Spectrum Jammer		
Repetition Period	T	50,500 [chips]
Intermediate Frequency	f_c	f_{LI}
Chirp Rate	R_c	1.023 Mchip/s

2.4.1.1 *WA: Probability of Detection*

The performance of the detection algorithm has been expressed in terms of probability of detection P_d, which is defined as:

$$P_d = Pr\left\{|\hat{T} - T| < T_s\right\} \tag{53}$$

i.e., as the probability that the difference between the estimated and the actual repetition period is lower than the sampling period. The performance depends on the characteristics of the incoming signals, on the values of the sampling frequency f_s, and of the maximum value of the correlation lags M_{lag} Waveform Acquisition (WA). The considered values are listed in Table 7. Due to the length of the obser-

Table 7: Acquisition Algorithm Parameters

Sampling frequency	f_s	20 MHz
Maximum Correlation lag	M_{lag}	$f_s \cdot 10^{-3}$
Observation window duration	M	$2 \cdot M_{lag}$

vation window duration M, for the previously described incoming signals and algorithm parameters, the probability of detection results to be always equal to 1. This is due to the fact that the autocorrelation function $R(m)$ converges to the jamming signal power J for (whit $K \in \mathbb{N}$), and it is proportional to N/M when the interference signal autocorrelation is null. Adopting large values of M (in the considered case we assume), the auto-correlation peaks are clearly distinguishable, thus resulting in probability of detection practically always equal to 1.

2.4.1.2 *WTC: Residual after Cancellation*

The performance of the tracking and cancellation algorithm depends on the number L of successive basic waveforms used for the calculation of the local replica. As indicated in Table 3, we considered two different values for L, i.e. L=10 and L=100.

Table 8: Tracking Algorithm Parameters

Sampling frequency	f_s	20 MHz
Averaging length	L	10, 100

The performance has been evaluated in terms of the relative residual power after cancellation, given by:

$$\mathbf{e} = \frac{|\mathbf{s} - \hat{\mathbf{s}}|^2}{|\mathbf{s}|^2} \tag{54}$$

In Figure 18-Figure 20 the relative residual power after cancellation is plotted versus time, in the case of chirp, single-tone and SS signals respectively, and considering an interference to noise ratio equal to 1 (J/N =0 dB). These results show that in all the analyzed cases the

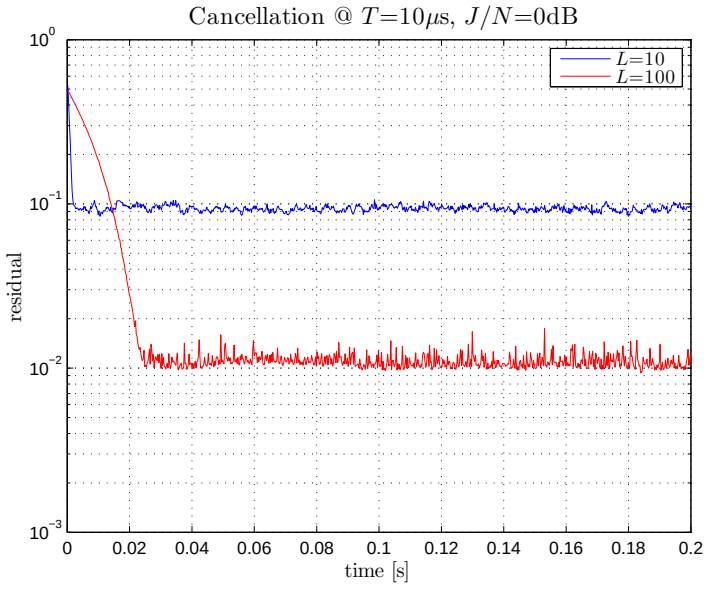

Figure 18: Chirp Signal: residual power after cancellation

interfering signal is strongly attenuated, thus substantiating the effectiveness of the approach both for narrow-band and for wide band signals. The residual power rapidly decreases and converges to 10^{-1} and 10^{-2} with L=10 and L=100 respectively, showing the performance improvements due to the adoption of a larger number of repetitions L for the estimation of the local replica. The convergence towards these values is faster as the estimated repetition period decreases: in the case of a single tone interfering signal, the period is equal to 2µs, and this leads to the very rapid convergence to the stationary behavior.

However, the length of the repetition period also affects the performance of the parameter estimations: in the case of longer repetition

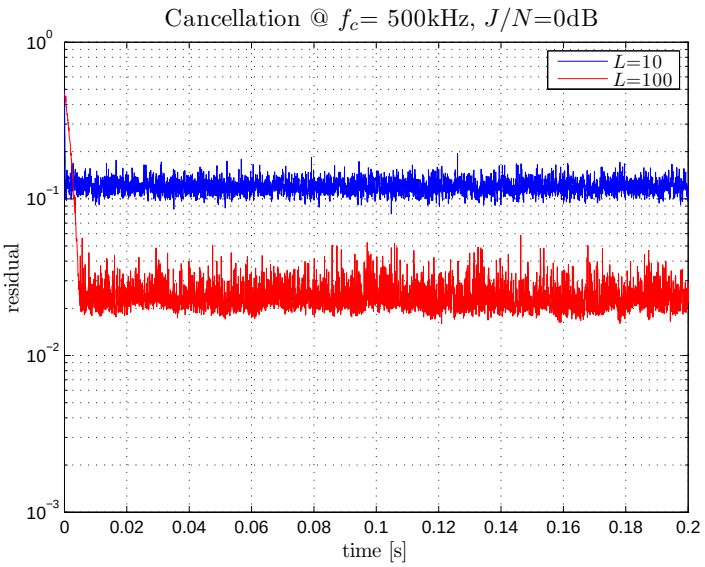

Figure 19: Single-tone: residual power after cancellation

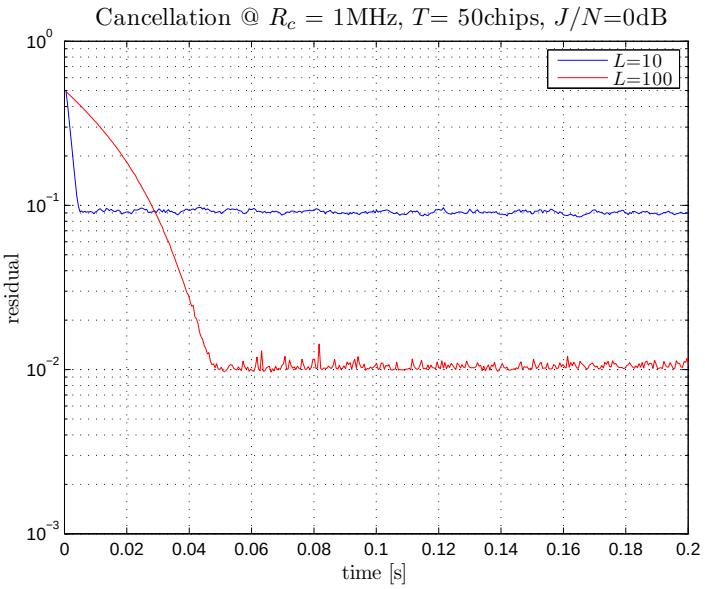

Figure 20: Spread Spectrum Signal: residual power after cancellation

periods parameters are more accurately estimated, and the relative residual power for the chirp and the SS signals, is slightly lower than in the case of a single tone interferer.

2.4.2 *Emulation*

The results provided in the previous Sections have been obtained by testing the algorithm with synthesized interfering signals. In the following, results calculated by testing the proposed algorithm with real jammer signals will be presented. These signals have been registered within an anechoic chamber: signals in the L1, L2 and L5 bands have been registered, with an instrument sampling the signals at 16 MHz. In Figure 21-Figure 23 the spectra of the received estimated and residual signals are shown, for interferers in the L1, L2 and L5 bands respectively. It is possible to observe that the estimated signals (green lines) tightly follow the spectrum of the received signals (blue lines); the residual signal spectra (red lines) clearly show that an attenuation of the interfering signal of at least 10 dB over the whole interfered band is guaranteed.

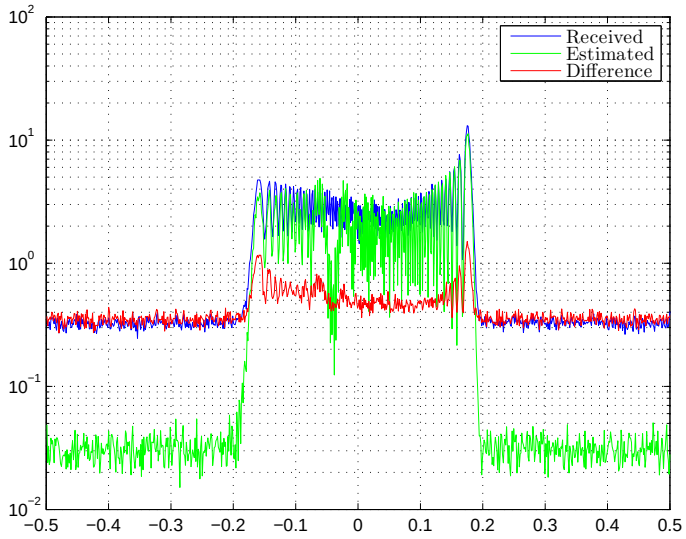

Figure 21: L1 band: received, estimated and residual signal spectra

2.4.3 *Complexity Evaluations*

In this Section, the complexity evaluation for the proposed WTC algorithm is provided. In particular, complexity is estimated in terms of number of operations (sums and products) to be performed during each repetition period as follows:

1. phase estimation for each signal delay hypothesis: this task requires the calculation of the correlation between complex sequences of length $\hat{m}$. Considering N_D delay hypotheses, this calculation needs: $\hat{m}N_D$ complex products, $\hat{m}N_D$ complex sums,

Figure 22: L2 band: received, estimated and residual signal spectra

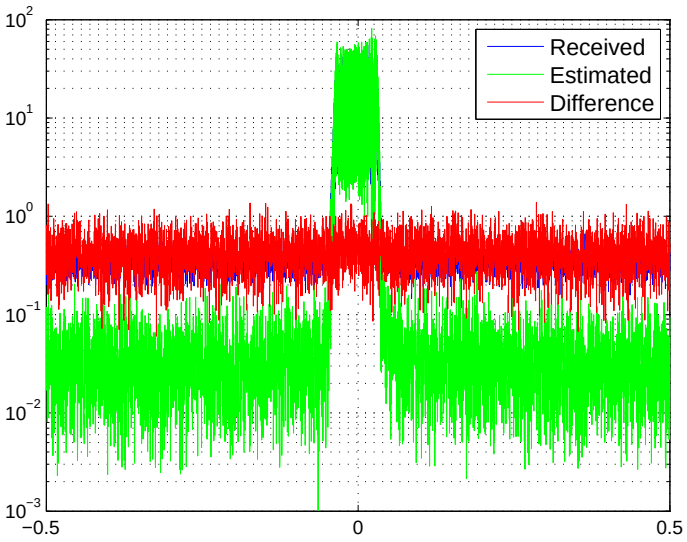

Figure 23: L5 band: received, estimated and residual signal spectra

and the calculation of N_D angles (this can be easily implemented numerically by means of known routines, the complexity of which depends on the specific choice);

2. calculation of the likelihood function for the joint delay and phase hypotheses: once the correlations have been calculated, only N_D de-rotations need to be implemented, which require N_D complex products.

3. amplitude estimation: since the correlation between the local replica and the incoming signal has already been calculated, only the local replica energy must be evaluated, with $\hat{m}$ complex products and $\hat{m}$ complex sums.

4. local replica update: L sequences of length must be averaged: it requires $\hat{m}L$ complex sums and $\hat{m}$ products. The total number of complex sums N_{sum} and complex products N_{prod} needed for the algorithm implementation is equal to:

$$N_{sum} = \hat{m}(N_D + 1 + L) \quad (55)$$

$$N_{prod} = \hat{m}(N_D + 1 + 1) \quad (56)$$

which demonstrates that the computational complexity is proportional to the estimated period $\hat{m}$. This result demonstrates that also in case of long repetition periods, the rate of the operations does not need to be increased, thus limiting the receiver complexity.

2.5 CONCLUSIONS

In this chapter, a simple and general approach for the interference mitigation/cancellation is proposed. Simulation results have substantiated the effectiveness of the proposed approach for a wide set of jammer signals: narrow-band single-tone, chirp and SS signals. The validity of the algorithm has been demonstrated also taking into account signals registered from real jammers within a controlled scenario. The jamming signals suppression is always larger than 10 dB, over the entire interfered bandwidth. It has also been demonstrated that the computational complexity is kept limited, thus making the proposed algorithm efficiently implementable. Further developments must take into account also the presence of the GNSS signals which could affect with the interference detection and parameter estimation processes.

INTERFERENCE MANAGEMENT TECHNIQUES: FURTHER DEVELOPMENTS

There are various possible developments for the work presented in part I of this thesis. This final chapter recollects some of the future directions in which the research in the field of GNSS interference detection, localization and cancellation will continue.

GNSS interference detection and localization techniques, although deeply investigated and mature, have further room for improvements. The presented work has shown how critical can be dealing with weak interference, due to the inherent presence of the useful signals, which limit the sensitivity level of the system performing detection and localization, even if based on CC. However, weak interference should not completely avoid the demodulation of the useful signals. Accordingly, further developments of the proposed cancellation method could be envisaged, which exploit information obtained from the detected signals. Furthermore, additional information regarding satellite signal CC could be available considering that the trajectories of the satellites repeat almost periodically; we expect that such information could be easily exploited in order to separate the GNSS and the interference signals contributions.

On the other hand interference cancellation is still an open topic. In particular, in the presented work it has been shown how exploiting a simple repetitive characteristic of the interference signals it has been possible to obtain very encouraging results for jammer signals, but further developments are still required in order to cope with spoofing. Due to the fact that spoofers are becoming and increasing problem for the reliability of the GNSSs, interesting challenges are taking place.

Part II

CODE SYNCHRONIZATION TECHNIQUES

Code synchronization is notoriously one of the most critical operations to be performed at the receiver. Its objective is to provide for each visible satellite a coarse estimation of the code phase and carrier Doppler [31]. Due to the wide uncertainty region and to the low SNR values characterizing this process, code synchronization requires strong computation resources and complex algorithms. To enable code synchronization and to improve receiver performance in terms of probability of detection and consequently in terms of Mean Acquisition Time (MAT), advanced techniques must be designed.

The aim of part II of this thesis is to extend the code synchronization capabilities of SS receivers to particularly harsh scenarios characterized by a large frequency uncertainty and strong frequency dynamics, and to optimize code epoch synchronization techniques for pairs and networks of cooperating receivers.

3

CODE-SYNCHRONIZATION FOR COMMUNICATIONS: THE CASE OF TT&C

3.1 INTRODUCTION

TT&C subsystems of telecommunication satellites operating in the LEOP have relied on the use of standard FM/PM modulations. However, the considerable increase in the number of satellites to be located in geostationary orbits has generated congestion problems and the impossibility to guarantee the proper spatial/frequency separation necessary for reliable TT&C operation in standard mode. This is why, in order to minimize the effect of interference and assure reliable operations, new SS modes are being introduced [29] [28]. In fact, SS modulations enable Code Division Multiple Access (CDMA) operations with frequency reuse thus allowing different spacecrafts in the same ground station beam-width to work at the same TT&C receiver frequency.

Nonetheless, as known, the advantages possessed by SS transmission can only be exploited after code synchronization is successfully achieved. The alignment between the transmitted spreading code and the locally generated sequence is in fact the necessary prerequisite for correct data demodulation and decoding.

In particular, for satellite TT&C subsystems, the presence of carrier frequency errors, due to oscillators instabilities with respect to the nominal operation and the relative motion between the transmitter and the receiver, yields Doppler and Doppler rate effects which can become seriously large especially during LEOP, constituting an additional issue that has to be taken into account during acquisition.

In the conventional approach, the frequency uncertainty domain is discretized such that the residual frequency offset affecting the correct hypothesis results to be small enough to allow code detection exploiting a totally coherent correlation over the code length. Nonetheless, in the presence of large frequency uncertainty this would reflect in excessive complexity, and the use of different approaches becomes necessary. In this work a technique is introduced, which consists in splitting the frequency uncertainty region in smaller sub-regions and then scanning the subregions by means of shorter FFTs. This is accomplished by first splitting the integration period in several sub-periods, over which coherent correlations with the local replica is performed, and then by taking the FFT of the sequence of correlation results. Moreover a post-processing stage is added, in order to estimate the Doppler variation rate, since it could lead to failure the subsequent tracking system. The algorithm is also presented in [P5].

3.2 SYSTEM MODEL

In the contest of this work, we focus on the up-link SS modulated signal described in [29], which represents the most challenging signal to be acquired due to complexity and energy consumption constraints at the receiver and to the presence of Multiple Access Interference (MAI) [7].

The usable chip rates in up-link are 1 Mchip/s and 4 Mchip/s; although a higher chip rate would improve the spreading factor and the global rejection performance, in order to take into account satellite operators' concern with bandwidth occupation, the chip rate selected for this study is 1.023 Mchip/s. The specific value 1.023 Mchip/s instead of 1 Mchip/s has been considered in order to enable code and data synchronism when using $\mathcal{L}$ =1023 chips long sequences and 1kb/s data rate.

Under these assumptions, defining the operators $|i|_A = i \bmod A$ and $\lfloor i \rfloor_B = \lfloor i/B \rfloor$, the baseband equivalent of the transmitted signal can be written as:

$$s_T(t) = \sqrt{E_c} \sum_{n=-\infty}^{+\infty} d_{\lfloor n \rfloor_{\mathcal{L}}} a_{|n|_{\mathcal{L}}} g(t - nT_c) \tag{57}$$

where E_c is the energy per chip, T_c is the chip period, d_n is the n-th data symbol, a_n is the n-th chip of the spreading sequence, and $\mathcal{L}$ is the sequence length. Considering the AWGN channel and the presence of MAI the baseband of the received signal can be written as:

$$s_R(t) = s_T(t - \tau) \exp\{j[2\pi(\Delta f t + \frac{r_D}{2} t^2) + \phi]\} + i(t) + \zeta(t) \tag{58}$$

where τ is the code delay introduced by the channel, Δf is the Doppler radian frequency shift, r_D is the Doppler rate shift, ϕ is the unknown initial phase, and $i(t)$ and $\zeta(t)$ are respectively the low-pass equivalent of the received MAI, and the wide sense stationary AWGN process with two sided Power Spectral Density (PSD) N_0.

Without loss of generality, it is possible to decompose the time delay τ as the sum of an integer multiple of T_c and of a residual fractional delay. In the following analysis only the fractional delay is considered (i.e. $\tau \in [0, T_c)$), and the integer part is assigned to the integer m.

3.2.1 *Working scenario: Launch and Early Orbit Phase*

In the following we will focus on the design of code acquisition algorithms able to work during the LEOP. Here the scenario characteristic parameters, taken from [7], are listed and described:

1. Carrier frequency f_0: the use of signals in the K_a band is foreseen for the next generation of TT&C systems. Since in the following the worst case scenario is considered, we assume $f_0 = 30$ GHz.

2. Frequency offset: the frequency offset Δf can be found by summing the contributions of the Carrier Doppler shift Δf_D and of the local oscillator Δf_{LO}:

$$\Delta f = \Delta f_D + \Delta f_{LO} = \pm(750 + 150)\text{KHz} = \pm 900\text{KHz}$$

3. Doppler variation rate: a variation rate of ± 1.7 ppm/s for carrier Doppler is foreseen, which corresponds to

$$r_D = 1.7 \cdot 10^{-6} \cdot 30 \cdot 10^9 = 51\text{KHz/s}$$

4. Chip pulse waveform: the transmitted signal is assumed to be SRRC filtered with roll-off factor equal to 0.5

5. Signal-to-noise plus interference ratio: an equivalent C/N_0 value, taking into account both the thermal noise and the interference contributions is used. Considering the presence of a Continuous Wave (CW) interferer with interference-to-useful power ratio $J/S = 20$ dB and the presence of up to 10 asynchronous CDMA interferers, 10 dBc above the useful signal, the resulting equivalent signal to noise ratio can be considered equal to [7]:

$$C/N_0 = 37\,\text{dBHz}$$

Under this assumption both interference and noise contributions are included in the equivalent noise process $\zeta(t)$ and the term $i(t)$ is discarded in the following. At the considered transmission rate, the SNR in terms of ratio between the energy per chip and the AWGN one-sided power spectral density is equal to:

$$E_c/N_0[\text{dB}] = C/N_0[\text{dBHz}] - 10\text{Log}R_c[\text{Hz}] = -23[\text{dB}]$$

6. Data values: it is assumed that during code acquisition no data are present and the transmitted signal is modulated only by the spreading sequence. Under this assumption $d_n = 1, \quad \forall n$.

3.3 SYNCHRONIZATION SUBSYSTEM

Synchronization represents a very critical task for TT&C during LEOP due to the very large Doppler uncertainty and dynamics affecting the received signal, but also to the very low signal-to-noise ratio. In fact in order to obtain satisfactory acquisition statistics long correlations must be performed (in this work we consider 4 and 8 ms long correlations). However, such long correlation periods affect tracking circuit responsiveness, and due to the rapid frequency shifts, loss of lock events may be generated. Thus, during the code acquisition phase, a preliminary estimation of the Doppler rate affecting the incoming signal becomes necessary.

Code acquisition can be accomplished directly by adopting a detection scheme able to search the time, frequency and Doppler rate

domains, or by post-processing data obtained during acquisition. In this work, the design of a code acquisition scheme that performs coarse code synchronization in the time and frequency domains and in post-processing evaluates Doppler rate and refines frequency measurements is presented. The block diagram of the code acquisition subsystem is reported in Figure 24: the received signal is processed by the front-end which downconverts the RF signal to baseband; the signal is then sampled by the Analog to Digital Converter Analog to Digital Converter (ADC) and sent to the detector block, whose goal is to calculate the Likelihood Ratio (LR) $\ell(\tau, \Delta f, r_D)$ for all time, frequency and Doppler rate hypotheses. Finally, the detector output is sent to the decision strategy block which determines the coarse estimates, accordingly to a defined decision criterion; data processed by the detector block are also sent to the frequency and Doppler-rate estimation block where the joint estimation of the two parameters is carried out.

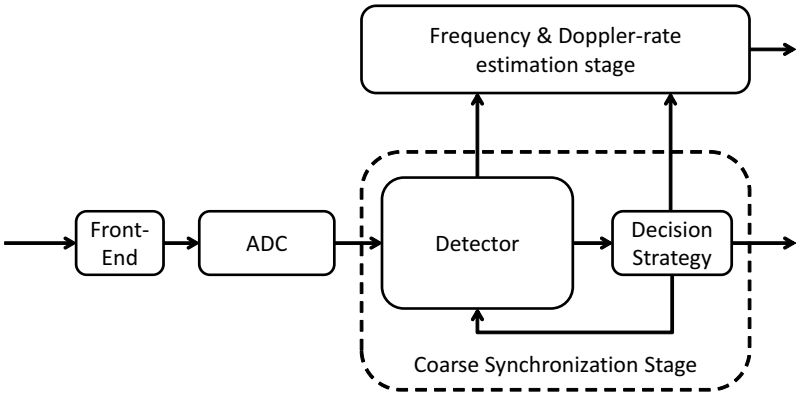

Figure 24: General receiver code acquisition sub-system block diagram

3.3.1 *Code acquisition: coarse synchronization*

The coarse synchronization stage has the objective of carrying out the initial estimation of the time delay and of the frequency offset. To do this, frequency windowing, which consists in testing different frequency macro-hypotheses identified in the following as Frequency Window (FW), is exploited: since the matched filter and the detector have limited bandwidth, N_{FW} frequency hypotheses are tested by de-rotating the input signal with different frequency hypotheses $f_{FW,i}$ ($i = 1, \ldots, N_{FW}$) (see Figure 25). The de-rotated signals can be processed either in parallel or serially, according to the receiver computational resources; in order to perform parallel computation a bank of N_{FW} detector blocks is needed, while to perform serial computation only one detector block is needed, but N_{FW} iterations must be carried out. Note that the two implementations do not change the behavior of the designed algorithm.

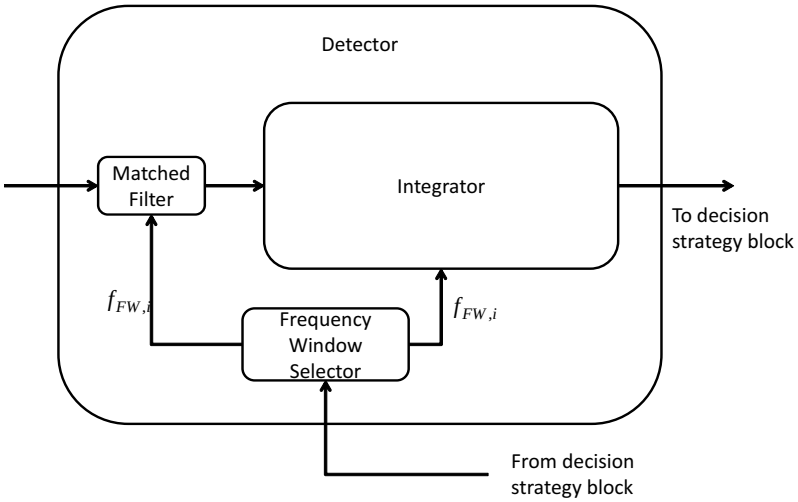

Figure 25: Detector block diagram

For the i-th FW the n-th sample of the time discrete derotated signal is:

$$\begin{aligned} s_{R,i}(nT_s) &= s_R(nT_s)\exp\{-j2\pi f_{FW,i}(nT_s)\} \\ &= s_T(t-\tau)\cdot \\ &\quad \cdot \exp\{j[2\pi(\Delta f_i nT_s + \frac{r_D}{2}(nT_s)^2) + \phi]\} + \\ &\quad +\zeta_i(nT_s) \end{aligned} \tag{59}$$

where $\Delta f_i = (\Delta f - f_{FW,i})$, T_s is the sampling rate after the ADC, and $\zeta_i(nT_s)$ is noise process rotated by the $f_{FW,i}$ frequency. The de-rotated signal is sent to the matched filter, adapted to the chip waveform, and then to the integrator block, that performs the calculation of the likelihood ratios by despreading the input signal. For the purpose of code acquisition the integrator block is assumed comprised of two complex correlators, with interleaved sampling times $1/2$ chip apart (called respectively on-time and late correlators): this results in two cells per chip with a total number of cells equal to $N_c = 2\mathcal{L}$. Nyquist-rate sampling is then applied at time instant $t_k = (k+\Delta)T_c$, where Δ is equal to 0 for the on-time correlator, and equal to $1/2$ for the late correlator.

For the i-th FW, after the matched filter the Nyquist-rate sampled signal has the form:

$$v_i(k) = s_{R,i}(nT_s) * g(nT_s)\Big|_{nT_s=t_k} \tag{60}$$

where the second term of the equation is the convolution of $s_{R,i}(nT_s)$ and $g(nT_s)$ sampled at time t_k. Note that in $v_i(k)$ and in the following the explicit dependance on time is neglected for simplicity of notation. It must be observed that in general this term can be expressed as:

$$\begin{aligned} v_i(k) &\simeq \sqrt{E_c}\sum_{n=-\infty}^{+\infty} a_{|k+n|_{\mathcal{L}}} R_{g,i}(nT_c+\tau_\Delta)\cdot \\ &\quad \cdot \exp\{j[2\pi(\Delta f_i kT_c + \frac{r_D}{2}(kT_c)^2 + \phi_\Delta)]\} + \\ &\quad +u_i(k) \end{aligned} \tag{61}$$

where $R_{g,i}(\tau)$ is the filtered frequency-shifted transmitted pulse, $u_i(k)$ is the noise sample that is distributed as a Gaussian random variable with 0 mean and variance equal to N_0, $\tau_\Delta = \tau - \Delta T_c$ and $\phi_\Delta \simeq \phi + 2\pi\Delta f_i(\Delta T_c)$. Note that the $n = 0$ element is the desired term, while the $n \neq 0$ tags indicate the Inter-Chip Interference (ICI) terms. It is worth noting that, if $\Delta f_i T_c \ll 1$, then $R_{g,i}(\tau)$ is approximately equal to the transmitted pulse autocorrelation function, whose expression is known in closed form; on the other hand, if the previous condition is not satisfied, $R_{g,i}(\tau)$ cannot be expressed in closed form. However, it should be noted that since the filter cuts off part of the input signal energy, the amplitude of $R_{g,i}(\tau)$ decreases with increasing Δf_i.

Inside each integrator block the swiveling filter algorithm [56] is enforced for the calculation of the likelihood ratios: the input signal is first despread, by multiplying the input sequence with the local replica, and then coherently correlated over L successive subperiods of M chips, and finally processed by a FFT processor (see Figure 26).

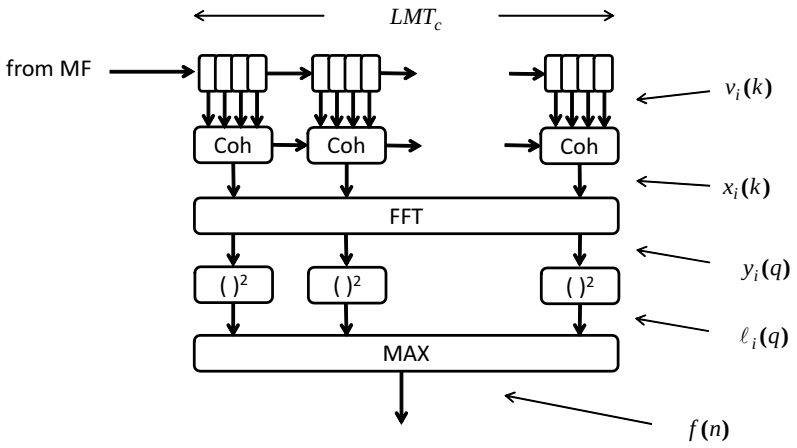

Figure 26: Swiveling filter block diagram

Performing despreading, summing the corresponding contributions, accumulating over M samples and normalizing by $\sqrt{M}$, under the H_1 hypothesis ($|mT_c + \tau_\Delta| < T_c/2$) and under the assumption that the Doppler rate effect on coherent accumulations is negligible, it is possible to approximate [65] as:

$$\begin{aligned} x_i(k) \simeq\ & R_{g,i}(\tau_\Delta)A(\Delta f)\cdot \\ & \cdot\exp\{j[2\pi(\Delta f_i k T_C + \frac{r_D}{2}(kT_C)^2) + \phi_\Delta]\} \\ & + \eta(k) \end{aligned} \tag{62}$$

for $k = 1, \ldots, L$, where $T_C = MT_c$, $\eta(k)$ is a noise sample distributed as a complex Gaussian random variable with 0 mean and variance equal to N_0, and

$$A(\Delta f_i) = \sqrt{E_c}\,\mathrm{sinc}(\Delta f_i T_C) \tag{63}$$

It is possible to observe that $A(\Delta f_i)$ takes into account the frequency offset and that with increasing M the accumulated energy decreases. On the other hand, under the H_0 hypothesis ($|mT_c + \tau_\Delta| > T_c/2$), ne-

glecting the Pseudo-Noise (PN) sequence out-of-synch autocorrelation the coherent correlations can be expressed as:

$$x_i(k) = \eta(k) \tag{64}$$

for $k = 1, \ldots, L$, i.e. the useful energy gives no contribution and only the noise component is observed.

Finally, the likelihood ratio, for the i-th FW, is calculated by means of the FFT algorithm as [56][57]:

$$\ell_i(q) = |y_i(q)|^2 \tag{65}$$

$$y_i(q) = \frac{1}{\sqrt{L}} \sum_{k=1}^{L} x_i(k) e^{-j2\pi k q \Delta f_{FFT} T_C} \tag{66}$$

It is possible to observe that $y_i(q)$ is the Fourier transform of the $x_i(k)$ sequence calculated in $q\Delta f_{FFT}$ ($q \in \mathcal{F} = \{-L_{FFT}/2, \ldots, L_{FFT/2} - 1\}$), where $\Delta f_{FFT} = f_C/L_{FFT}$ is the FFT frequency step, being L_{FFT} the FFT length. This solution leads to the architecture represented in Figure 26 composed of an array of L coherent integrators of length M, resulting in an integration time $T_I = LMT_c$, and a following FFT block of length $L_{FFT} \geqslant L$; in case L_{FFT} is strictly larger than L, the FFT can be computed by zero padding the FFT input vector.

It is worth noting that the FFT frequency range is determined only by the coherent correlation period, and could also be larger than Δf_{FW}. However, due to equation (63), for each i-th FW, frequencies far from $f_{FW,i}$ are strongly attenuated by coherent correlation; for this reason, for the i-th FW only the a subset $\mathcal{F}_0$ of $\mathcal{F}$ comprised of N_{FFT} frequency points is considered:

$$\mathcal{F}_0 = \{-F, \ldots, 0, \ldots, F\} \tag{67}$$

with $F = \left\lfloor \frac{N_{FFT}}{2} \right\rfloor$.

3.3.2 *Decision criterion*

In literature, a multitude of decision criteria are available [49][13][16][48]. Both single and multi-dwell strategies, based on the MAX criterion and/or the Threshold Crossing (TC) criterion, can be used for the problem at hand. The choice of the most suited criterion is not straightforward and needs to take into account the specific cost function to be minimized.

Due to the bandwidth of the tracking correlators, the frequency estimations must be very accurate; in order to enhance their accuracy the best choice is to increase the number of dwells N_d.

In this work we considered the MAX criterion for the selection of the frequency hypothesis and the TC criterion for the selection of the time delay hypothesis. Let us indicate with $\mathcal{C}^{(j)}$, ($j = 1, \ldots, N_c$) the i-th time hypothesis composing the time delay uncertainty region; the

sets of likelihood ratios $\ell_i(q)$ ($i = 1, \ldots, N_{FW}$) calculated for $\mathcal{C}^{(j)}$ are sent to a block which implements the MAX criterion, that is, selects the frequency value $(\hat{i}_{FW}, \hat{q})$ corresponding to the largest likelihood ratio:

$$(\hat{i}_{FW}, \hat{q}) = \arg \max_{(i,q)} (\ell_i(q)) \tag{68}$$

The corresponding test variable $\ell_{\hat{i}}(\hat{q})$ is then used to detect the time delay according to the TC criterion. Let $\ell_{\hat{i}}(\hat{q})$ be the likelihood ratio calculated for $\mathcal{C}^{(j)}$, for the $\hat{i}$-th FW for frequency $\hat{q}$; the following test is performed: $\ell_{\hat{i}}(\hat{q})$ is compared with a threshold ξ; if $\mathcal{C}^{(j)}$ is the H_1 cell then two events are possible:

- *Missed detection:* the test variable $\ell_{\hat{i}}(\hat{q})$ is under the threshold;
- *Correct detection:* the test variable $\ell_{\hat{i}}(\hat{q})$ is above the threshold;

On the other hand, if $\mathcal{C}^{(j)}$ is a H_0 cell, then the possible events are:

- *False alarm:* the test variable $\ell_{\hat{i}}(\hat{q})$ is above the threshold;
- *Correct rejection:* the test variable $\ell_{\hat{i}}(\hat{q})$ is under the threshold;

The use of the TC criterion allows to limit the complexity of the acquisition process, as it does not require the calculation of the likelihood ratios for all the N_c code delay hypotheses $\mathcal{C}^{(j)}$.

3.3.3 *Frequency and Doppler rate estimation*

In order to obtain a Doppler rate estimate and a refinement of the frequency offset measurements, a post-processing stage has been designed. In our proposed scheme, the information coming from the code acquisition logic is exploited in order to limit the complexity of the estimation process.

For this purpose we propose two different algorithms: a Maximum Likelihood Estimator (MLE) exploiting the Fourier transform samples shown in equation (66); a Least Square Estimator (LSE) based on the frequency estimations of equation (68).

3.3.3.1 *Maximum Likelihood Estimator*

Let us assume that the algorithm starts working after code acquisition has been declared, that is under the assumption that the H_1 cell has been identified. The Fourier transform samples calculated at the n-th dwell can thus be written, by generalizing equation (66), as:

$$y_i^n(q) = \frac{1}{\sqrt{L}} \sum_{k=nL+1}^{nL+L} x_i(k) e^{-j2\pi k q \Delta f_{FFT} T_C} \tag{69}$$

Let us rewrite last expression as:

$$y_i^n(q) = z_i^n(q, \Delta f, r_D, \phi) + \nu_i^n(q) \tag{70}$$

where we divided the useful signal $z_i^n(q, \Delta f, r_D, \phi)$, dependent on the unknown parameters $\Delta f, r_D, \phi$, from the noise $\nu_i^n(q)$, with $q \in \mathcal{F}_0$. The MLE jointly estimates the frequency offset Δf and the Doppler rate r_D by choosing the the couple $(\Delta f, r_D)$ that maximizes the Average Log-Likelihood Function (A-LLF) $\Lambda(\Delta f, r_D)$:

$$(\hat{\Delta f}, \hat{r}_D)_{\mathbf{MLE}} = \arg \max_{\Delta f, r_D} \Lambda(\Delta f, r_D) \tag{71}$$

where

$$\begin{aligned} \Lambda(\Delta f, r_D) = & -\frac{1}{N_0} \|\mathbf{Z}(\Delta f, r_D)\|^2 + \\ & + \ln \left\{ I_0 \left[\frac{2}{N_0} \left(\mathbf{Y} \times \mathbf{Z}^*(\Delta f, r_D) \right) \right] \right\} \end{aligned} \tag{72}$$

with

$$\|\mathbf{Z}(\Delta f, r_D)\|^2 = \sum_{n=1}^{N_d} \sum_{i=1}^{N_{FW}} \sum_{q \in \mathcal{F}_0} |z_i^n(q, \Delta f, r_D)|^2 \tag{73}$$

$$\mathbf{Y} \times \mathbf{Z}^*(\Delta f, r_D) = \sum_{n=1}^{N_d} \sum_{i=1}^{N_{FW}} \sum_{q \in \mathcal{F}_0} y_i^n(q) z_i^{n*}(q, \Delta f, r_D) \tag{74}$$

It is worth noting that eq. (72) is based on the modified Bessel function. The Bessel function approximation for small arguments, which could be exploited due to the low SNR values typical of this scenario, is not considered here since our purpose is to present the performance in the optimal case. The presented solution is very resource consuming, since for each joint $(\Delta f, r_D)$ hypothesis, the calculation of the A-LLF requires very complex calculations. In order to reduce the complexity of the algorithm, a sub-optimal solution has been proposed that exploits the property of the energy distribution of the incoming signal in the frequency domain. The despread signal is in fact a narrow band signal whose energy is distributed over a very limited number of FFT output samples. The index $i_{max}^n(\Delta f, r_D), q_{max}^n(\Delta f, r_D)$ corresponding to the maximum of the energy distribution can be explicitly found as [15]:

$$i_{max}^n(\Delta f, r_D) = \text{round} \left[\frac{f_c^n(\Delta f, r_D)}{\Delta f_{FW}} \right] \tag{75}$$

$$\begin{aligned} q_{max}^n(\Delta f, r_D) = & \ \text{round} \left[f_c^n(\Delta f, r_D) + \right. \\ & \left. - i_{max}^n(\Delta f, r_D) \Delta f_{FW} \right] \end{aligned} \tag{76}$$

where

$$f_c^n(\Delta f, r_D) = \Delta f + r_D \left(n - \frac{1}{2} \right) T_I \tag{77}$$

Limiting the sum to the previous terms the following suboptimal estimation algorithm (Reduced MLE (RMLE)) has been identified:

$$(\hat{\Delta f}, \hat{r}_D)_{\mathbf{RMLE}} = \arg \left[\max_{\Delta f, r_D} \left(\Lambda'(\Delta f, r_D) \right) \right] \tag{78}$$

with

$$\Lambda'(\Delta f, r_D) = \\ -\sum_{n=1}^{N_d} z^n_{i^n_{max}}(q^n_{max}, \Delta f, r_D) z^{n*}_{i^n_{max}}(q^n_{max}, \Delta f, r_D) \\ + \ln\left\{ I_0\left[\frac{2}{N_0}\left(\sum_{n=1}^{N_d} y^n_{i^n_{max}}(q^n_{max}) z^n_{i^n_{max}}{}^*(q^n_{max}, \Delta f, r_D)\right)\right]\right\} \tag{79}$$

According to this suboptimal solution, for the test of each joint $(\Delta f, r_D)$ hypothesis, only one sample per dwell is needed, thus complexity is dramatically reduced.

3.3.3.2 *LSE algorithm*

The LSE approach consists in minimizing the distance between the vector of the frequency estimations.

$$\mathbf{f} = \begin{bmatrix} f(1) \\ f(2) \\ \vdots \\ f(N_d) \end{bmatrix} = \begin{bmatrix} i^1_{FW}\Delta f_{FW} + q^1 \Delta f_{FFT} \\ i^2_{FW}\Delta f_{FW} + q^2 \Delta f_{FFT} \\ \vdots \\ i^{N_d}_{FW}\Delta f_{FW} + q^{N_d} \Delta f_{FFT} \end{bmatrix} \tag{80}$$

being i^n_{FW} and q^n the index estimated according to (68), and a frequency hypotheses vector $\mathbf{w} = [w(1), \ldots, w(N_d)]^T$ [32]. By defining the hypotheses array $„ = [\Delta f, r_D]^T$, under the assumption that the frequency evolves linearly, the frequency array $\mathbf{w}$ can be written as:

$$\mathbf{w} = \mathbf{H}„ \tag{81}$$

where

$$\mathbf{H} = \begin{bmatrix} 1 & \frac{T_I}{2} \\ 1 & \frac{3}{2}T_I \\ \vdots & \vdots \\ 1 & (N_d - \frac{1}{2})\,T_I \end{bmatrix} \tag{82}$$

The LS estimates are found according to [32]:

$$(\hat{\Delta f}, \hat{r}_D)_{\mathbf{LSE}} = (\mathbf{H^T H})^{-1}\mathbf{H^T f} \tag{83}$$

It is worth observing that this solution is very simple, thus it can be implemented without a complexity increase of the acquisition engine.

3.4 NUMERICAL RESULTS

To evaluate the performance of the proposed 2D+post processing scheme, the algorithm numerical characterization has been carried out. Results will be presented and discussed in this section.

Table 9: Parameters used in numerical simulations

Code length $\mathcal{L}$	1023 chips
Coherent correlation length M	11 chips
Number of coherent integrators L	372, 744
Integration period T_I	4, 8 ms
FFT length L_{FFT}	512, 1024
Number of frequency windows N_{FW}	37
Number of dwells N_d	2,4,8

3.4.1 *System Optimization*

System performance strongly depends on several parameters: the coherent correlation length M, the FFT length L_{FFT}, the number of FWs N_{FW}, the number of dwells N_d and the adopted thresholds. Due to the number of parameters to be considered and on the metrics to be optimized, the optimization of the parameters is not straightforward. As shown in [15], several parameter configurations can be proposed. Here, the performance of the solutions with parameters shown in Table 9 is shown.

3.4.2 *Performance Evaluation*

Taking into account that the approach aims to achieve optimal solutions without considering mathematical approximations, performance evaluations have been carried out in terms of ROCs, MAT, which gives an average measure of the time needed to acquire time synchronism, and frequency and Doppler rate Root Mean Square Error (RMSE), which express the estimation accuracy.

To derive the MAT a semi-analytical tool, based on the solution of a Markov chain is exploited [49][13]. The code acquisition process is modeled as a Markov chain whose transition gains are function of the probability of False Alarm P_{fa}, of the probability of Missed Detection P_{md}, and of the dwell times. We derive the P_{fa} and P_{md} values by means of numerical simulations, and we exploit the solution of the associated code acquisition to evaluate the MAT according to:

$$T_A = \frac{1}{P_D}\left\{T_d\left[1+\frac{Q}{2}(2-P_D)\right]+T_p\frac{Q}{2}P_{fa}(2-P_D)\right\} \tag{84}$$

being $P_D = P_d(2-P_d)$, T_d the cell duration, equal to half the chip duration, $Q = N_c - 2$, and T_p the penalty time equal to 16 ms.

The ROCs are shown in Figure 27: it is possible to observe that, in general, the integration time $T_I = 8$ ms guarantees better performance with respect to the $T_I = 4$ ms case; this is due to the fact that longer integrations periods allow to get larger SNR values. With increasing C/N_0, P_{fa} and P_{md} metrics rapidly decrease, but in the $C/N_0 =$ 37dBHz case probabilities are quite large: this is due to the fact that

the Doppler rate is not counteracted in the swiveling filter which introduces significant energy losses.

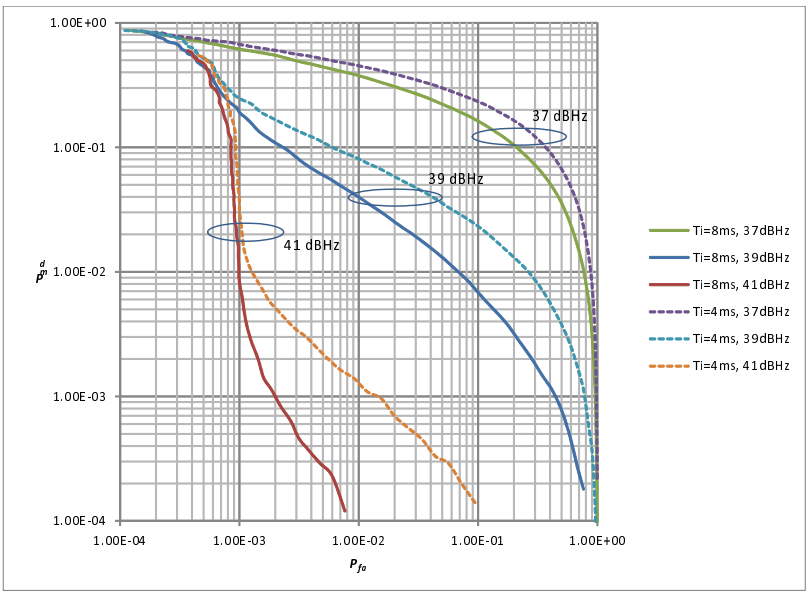

Figure 27: Receiver operating characteristics

Finally, in Figure 28, the MAT for the $C/N_0 = 37$ dBHz case are shown: it is possible to observe that the integrator performing longer correlations leads to the best results with a MAT of about 20ms for very low P_{fa} values. This result thus suggest to use a large threshold in order to reduce the probability of false alarm events that strongly reduce the performance of the acquisition system.

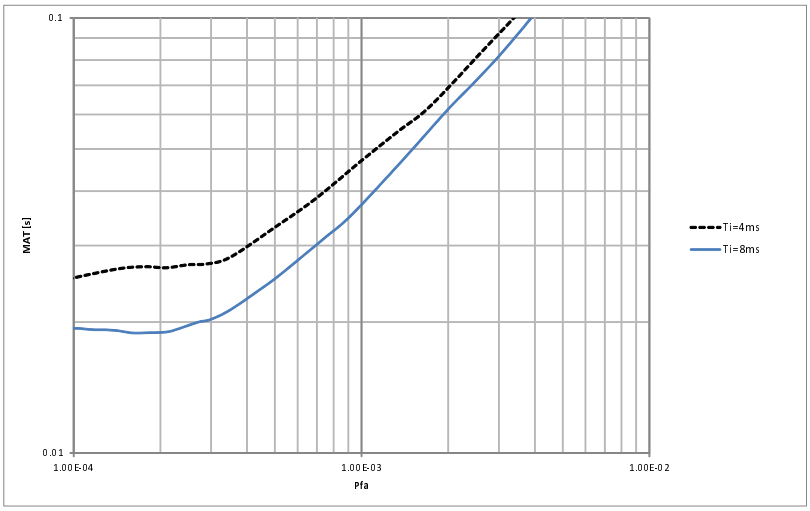

Figure 28: Mean Acquisition Time, $C/N_0 = 37$dBHz

In Table 10 the RMSEs of the frequency estimation carried out by the swiveling filter with different integration periods T_I at different SNRs are reported; it is possible to observe that at the $C/N_0 = 37$dBHz, due both to the very low SNR and to the effect of the Doppler rate that introduces a bias in the frequency estimation, the RMSE is very high. Given that the tracking pull-in range is generally limited to several tens or hundred Hz, depending on the correlator and loop

Table 10: Swiveling Filter: Frequency estimation RMSE

C/N_0 [dBHz]	T_I [ms]	RMSE [kHz]
37	4	58.9
37	8	43.9
39	4	16.2
39	8	8.4
41	4	0.71
41	8	0.57

Table 11: LSE: Frequency estimation RMSE (C/N_0 =37 dBHz)

T_I [ms]	N_d	Δf RMSE [kHz]	r_D RMSE [MHz/s]
4	2	58.1	21.2
4	4	50.7	7.2
4	8	40.2	2.3
8	2	42.9	7.6
8	4	35.9	2.4

filter schemes, these results clearly show why frequency refinement and Doppler rate estimation become mandatory in the scenario under consideration. In Table 11 and 12, the performance in terms of RMSE for the frequency and Doppler rate estimates carried out according to the LSE and the Reduced MLE algorithms is shown for $T_I = 4$ and 8 ms and $N_d = 2, 4, 8$. It is possible to observe that for $N_d = 2$ both for the case of $T_I = 4$ms and the case of $T_I = 8$ms the frequency estimates RMSE reduces very slightly with respect to the single estimation case: this behavior demonstrates that most of the frequency estimates RMSE is due to the bias introduced by the Doppler rate. With increasing numbers of dwells the RMSE decreases, but the best result is still in the order of several kHz, which may be too large for the tracking circuits pull-in ranges. Regarding the Doppler rate estimates RMSE, it is possible to observe that very large errors are obtained, which make these estimates practically un-useful. Considerably better performance is obtained considering the Reduced MLE algorithm: the frequency errors are practically always limited to less than hundred Hz, thus guaranteeing very reliable estimates; also the Doppler rate measurements are very accurate, resulting in the order of several kHz/s, and can be efficiently exploited by the tracking circuits. This performance enhancement with respect to the LSE algorithm is obtained at the cost of a very large complexity increase, since the MLE needs to test sequentially a large number of frequency and Doppler rate hypotheses; however, since the LSE algorithm limits the frequency error to several kHz, it is possible to envisage a solution consisting in applying both the LSE algorithm, in order to perform a coarse estimation of the frequency, and the Reduced MLE in order to estimate Doppler rate and refine frequency offset.

Table 12: Reduced MLE: Frequency estimation RMSE (C/N_0 =37 dBHz)

T_I [ms]	N_d	Δf RMSE [Hz]	r_D RMSE [Hz/s]
4	2	68	11.7e3
4	4	17	2.1e3
4	8	13	2.2e2
8	2	119	13.7e3
8	4	42	2.4e3

Table 13: Complexity Evaluation: Coarse Code Synchronization

T_I [ms]	N_{prod}	N_{sum}
4	643 k	814 k
8	1363 k	1742 k

3.4.3 *Complexity Evaluation*

As mentioned, the synchronization of SS codes in low SNR and high frequency uncertainty scenario involves complex signal processing and very high resource consumption. In this section, a brief analysis of the complexity of the presented algorithms in terms of number of operations (additions and multiplications) is presented.

In the coarse code synchronization algorithm the number of operations is obtained taking into account that the signal must be rotated according to each FW central frequency and must be correlated according to the swivelling filter architecture. Considering a radix-2 butterfly implementation of the FFT algorithm, the results of Table 13 can be obtained. The shown values identify the number of products N_{prod} and the number of sums N_{sum} needed to evaluate the likelihood ratio for each delay hypothesis. It is possible to observe that by doubling the duration of the integration period also the complexity of the correlation stage doubles, thus a trade-off between complexity and performance improvement must be achieved.

The coarse code synchronization stage is certainly the most demanding task from a computational point of view; nonetheless, in order to complete the algorithms characterization, it is interesting to analyze the resource demand of the frequency and Doppler-rate estimation algorithms. The complexity evaluations are summed in Table 14, where the values express the number of operations needed in order to perform the frequency and Doppler-rate estimations. Note that for the ML estimation the number of required operations depends on the number of joint frequency/Doppler-rate hypotheses N_{hyp} to be tested. By discretizing the frequency uncertainty range into 50 Hz frequency bins, and the Doppler-rate uncertainty range into hypotheses each separated by 1 kHz/s, a total number of hypotheses $N_{hyp} = 3.6e6$ is obtained. It is thus easy to understand that because of the high number of hypotheses this solution is not easy to implemented. However, due to the very low complexity of the LSE

Table 14: Complexity Evaluation: Frequency and Doppler rate estimation

Algorithm	Dwells Number	N_{prod}	N_{sum}
R-MLE	4	$N_{hyp} * 24$	$N_{hyp} * 24$
R-MLE	8	$N_{hyp} * 48$	$N_{hyp} * 48$
LSE	4	8	8
LSE	8	16	16

algorithm, the application of a joint LSE-MLE approach can still offer good performance and guarantee a considerable complexity reduction.

3.5 CONCLUSIONS

The aim of this chapter is to provide a feasible synchronization scheme for the new telecommunication satellite TT&C systems, which will operate in SS mode also during the very critical LEOP. This scenario is characterized by very large frequency offset and Doppler rate values, that if not taken into account may have a large impact on code synchronization. However, due the low SNR values, results have shown that frequency and Doppler rate estimation become very challenging operations to be performed. Therefore, with particular attention focused on providing accurate time, frequency and Doppler rate values to the tracking circuits, several new detector schemes have been designed and analyzed in this work. The numerical results show that the LSE estimation technique achieves good performance only at high SNR values, while the RMSE algorithm allows to provide accurate and usable estimations but at the cost of a higher computational complexity with respect to the LSE algorithm.

To limit complexity at the receiver side, the proposed RMSE and LSE algorithms rely on a post processing of the data available after 2D search to evaluate the Doppler rate and refine the frequency estimate. If complexity is no longer an issue, then a full 3D search approach remains to be analyzed. A 3D acquisition procedure could in fact constitute a good an innovative solution to the code acquisition problem in fast frequency varying scenarios. Indeed, with a 3D search, each hypothesis is a composition of the three sub-hypothesis in the delay, frequency and Doppler rate domains, and therefore the detection of the H_1 hypothesis is related to the ideal alignment in the all three domains, yielding optimal performance but at the cost of maximal complexity at the receiver.

4

DYADIC COOPERATION IN CODE-ACQUISITION

4.1 INTRODUCTION

In previous chapter the code synchronization problem in a harsh scenario is considered. In this chapter, a general framework for the performance analysis of a complex system composed of cooperating FSMs dedicated to the search for code epoch acquisition is proposed. This framework can be applied to every case in which two code epoch synchronization systems can cooperate:

- *P2P*: Considering a couple of nodes in a peer-to-peer network, the two FSMs correspond to the operations performed by the two receivers in trying to acquire synchronization to the same satellite or terrestrial ranging anchor;
- *Hierarchical codes*: In the case of a spreading code constructed as a hierarchy of two sub-codes, typically a short one superimposed periodically on a long and congruent one [1], the first FSM deals with the recovery of the short code, while the second FSM resolves the residual ambiguity on the long code;
- *Rake receiver*: Considering two fingers in a Rake receiver [8], which are looking for separate replicas of the same code which has undergone multipath propagation, the first FSM corresponds to the engine which finds the first code epoch, while the second FSM corresponds to the next subsequent search which works in an uncertainty region essentially tied to the delay spread in the propagation channel;
- *Multiple navigation signals*: Several GNSS systems foresee the delivery of multiple services with different quality in the same GNSS bands, multiplexed through the use of different spreading codes, with different chip rates and/or period [1][31]. Then, the two FSM correspond to the search for synchronization on two of these services in a cooperative fashion;
- *Assisted GNSS*: The case where a ground station provide differential information to those receivers which are present in its coverage area can also be seen as a particular case of this general framework. In fact, in this case the first FSM corresponds to the very precise functionality of the ground station, while the second represents the operations of the receiver with assistance information to reduce its uncertainty region. In this case, there is no need for a feedback to the ground station, so this is exemplary of what we call unidirectional flow between FSMs, as opposed to the bidirectional flow which can be foreseen in the previous cases;

- *Acquisition of GNSS constellation*: Finally, in some cases it could be possible to reduce the uncertainty region in the search of a navigation satellite once a previous satellite has been acquired, based for example on the knowledge of the constellation ephemeris. When this applies, then our framework can still be used in the analysis of code acquisition performance.

The fundamental common idea is that once an FSM has reached an H_1 decision (i.e., a decision in favor of a cell where the code epoch is assumed to be found), then this information is immediately passed on to the other FSM, which uses this information to reduce its own uncertainty region. In case the exchanged information is found to be invalid by the second FSM, then feedback can occur, in order to help the first FSM in recovering from its own error.

The problem of FSMs performing code acquisition has been widely investigated and a very comprehensive literature exists [49][50][13][16]. In these works general frameworks considering detection performed according to the MAX/TC criterion is proposed, providing effective tools for the analysis of the performance of code acquisition. On the other hand, examples of the application of the aided approach for code acquisition of navigation signals has been presented in [20], [58],[39], [38] for the acquisition of GPS L1 and L2C signals and in [18] for the Galileo E1 and E5 signals. [18] in particular, introduces an uni-directional information flow technique that relies on the exchange of signal time alignment information. The detection problem in the two bands is solved according to the MAX criterion by proposing a simple and effective scheme. In the present work, we generalize the problem to two cooperating FSMs aiming to perform code epoch acquisition, by considering also MAX/TC detection strategies. The framework is also presented in [P6].

4.2 SINGLE FSM CODE ACQUISITION

For the sake of self-consistency, we review here briefly the main traits of code acquisition in a single FSM. As known, the objective of code acquisition is detecting the presence/absence of a signal, and determining its code delay and eventually its frequency offset. In order to accomplish this goal, the code acquisition engine performs different steps described in the following. Initially, it scans the uncertainty region composed of all the possible code delay (and frequency offset) hypotheses, in order to identify a correct test hypothesis H_1 (i.e. a cell with code delay and frequency offset within the pull-in range of the tracking circuit) and to discard all the incorrect hypotheses H_0 [64]. In general, for each cell, a likelihood function is evaluated, taking the correlation of the incoming signal with a local replica generated at the receiver; in order to perform this operation a number of implementation strategies have been proposed during the years, but for navigation satellite signals, a very efficient approach exploiting FFT and IFFT is often adopted [10][55], which allows to scan a number of code delay hypotheses equal to the length of the processed observ-

able in parallel. This approach results to be very efficient for code acquisition circuits implementation since the length (in chips) of the PN sequences is equal to the number of code delays to be tested. On the other hand, in case the length of the sequences is much larger than the number of cells to be tested, a scheme exploiting correlators (performing sum of products) could result more efficient. Given that in the absence of noise the likelihood function presents a peak in correspondence of the H_1 hypothesis, different decision criteria could be adopted: selecting the largest correlation value (MAX criterion), comparing the correlation outputs with a threshold (threshold crossing, TC criterion) [64], or adopting the MAX/TC hybrid option [13]. In the following, detection is performed selecting the cell corresponding to the largest likelihood value exceeding a certain threshold ξ, according to the general MAX-TC criterion. Finally, in case a H_1 cell has been selected, the tracking circuit starts correlating and tracking the signal, on the other hand, if an H_0 cell is selected, the tracking circuit cannot lock to the correlation peak and the search/detection operations need to be repeated.

It should be noted that in case the specific *searched* signal is not present, the search algorithm would be repeated infinite times, as neither detection nor tracking would succeed. In order to break this behaviour, different strategies can be envisaged: a simple approach consists in setting a time-out period T_{out}, so that the search operation for the *searched* signal terminates and code acquisition is started for a different signal.

The Signle FSM acquisition procedure, carried out according to the MAX/TC criterion, is detailed in Algorithm 5.

MAX-TC Single FSM Acquisition procedure;
while *1* **do**
  Search;
  Correlation is evaluated for all the possible code delays to be tested;
  The greatest correlation is compared with the threshold ξ ;
  The correspondent code delay is selected;

  if correlation is lower than the threshold ξ **then**
    Search is repeated;
  else
    if the selected code delay is an H_1 cell **then**
      Acquisition is completed;
    else
      Tracking circuit fails, and **Search** is restarted
    end
  end
end

Algorithmus 5 : Single FSM acquisition procedure

4.3 DYADIC CODE ACQUISITION STRATEGIES

The problem of code acquisition performed by two FSMs can surely be solved by considering each FSM independently and implementing for each FSM the procedure described above. However, this would result in a system with a doubled computational complexity with respect to the single FSM case (which would directly translate in twice the computation delay and, more in general, in twice the power consumption). As already observed in [18], in case the two FSMs are processing signals which are correlated, it is possible to exploit the mutual information carried by one of the two signals in order to simplify the synchronization operations performed to acquire the second.

More in particular, since in all the described cases we consider signals having correlated delays, it is possible to exploit the code delay estimation taken by the first FSM in order to reduce the uncertainty region scanned by the second, thus improving its detection performance. Using the same notation of [18], we identify as the Master FSM the FSM accomplishing the first code acquisition, which is characterized by the scan of its Complete Uncertainty Region (CUR), while we identify as the Slave FSM the FSM performing search operations over a Reduced Uncertainty Region (RUR), exploiting the time reference provided by the Master FSM.

For all the scenarios presented in the Introduction, in this chapter we propose a general framework for dyadic code acquisition by building on the procedure designed in [18] and by generalizing the proposed scheme taking into account the MAX-TC decision criterion. Furthermore, an analytic tool for the evaluation of the performance is also herein provided.

4.3.1 *Unidirectional Flow Dyadic Code Acquisition*

The procedure presented in [18] consists of a Master FSM operating with one Galileo signal and providing a code delay information to the Slave FSM operating on a different time aligned Galileo signal in order to reduce the dimension of its uncertainty region. We identify this approach as Unidirectional flow, since the aiding information goes from the Master FSM to the Slave FSM. It is interesting noting that this approach could perfectly fit all the envisaged scenarios and not only the dual band receiver case. Applying the MAX-TC criterion, we generalize the behavior of this approach in order to exploit the advantages given by the additional TC step, which allows to limit the probability of errors.

Accordingly, the Uni-Directional (UD) acquisition procedure has been updated to include the operations detailed in the following. Initially the Master FSM performs the search of the H_1 cell in the CUR with a procedure identical to the one described for the single FSM case. The detection is performed by selecting the cell corresponding to the largest likelihood value and by comparing it with a threshold ξ_M. If the likelihood is lower than the threshold the cell is discarded

and the search is repeated; conversely if the likelihood value is larger, the cell is selected and tracking can commence while the slave FSM starts its own scan. In case the cell selected by the Master FSM is a H_0 hypothesis, tracking breaks and the Master search is restarted, while if an H_1 hypothesis is selected, the Slave search procedure can continue. The Slave FSM performs the search for the H_1 cell in a similar fashion to the Master by selecting the cell corresponding to the largest correlation value and comparing it with a threshold ξ_S. If the selected value is lower than the threshold, the Slave search is repeated, while if larger it is selected. If an H_0 cell is selected, the search operations are restarted after tracking failure, while in case a H_1 cell is chosen, acquisition is completed. However, it should be noted that thanks to the exchange of information the Slave search is performed inside a RUR thus considerably limiting the number of H_0 cells. This procedure is detailed in Algorithm 6.

Also in this case, a time-out period T_{out} can be used in order to break the infinite repetition of the acquisition operations in case the specific satellite signals are not present.

4.3.2 *Bidirectional Flow Dyadic Code Acquisition*

The unidirectional approach does not address the fact that the Master FSM still needs to perform the search inside a very large uncertainty region, which can often lead to errors requiring a considerably long time (equal to the integration time of the tracking correlators) to recover from. In order to further improve the performance of the master FSM, a multi-dwell decision strategy could be adopted, by adding a further verification step after the first detection [16] and limiting the error probability. Given that we consider two FSMs, verification can be performed by exploiting the Slave FSM: this way, the Slave search acts both as the Master FSM verification stage and the Slave FSM detection operation. If the Slave FSM test fails, the Master FSM can restart scanning over the CUR again. This approach tightly couples the Master and the Slave code acquisition engines, further optimizing the efficiency of the synchronization engines. It is also worthwhile noting that this approach does not introduce any additional computation, thus keeping the complexity under control. We identify this approach as Bi-Directional (BD) flow code acquisition.

The Master FSM performs the search and the detection similarly to the UD case; if the maximum correlation is lower than the threshold ξ_M the scan is repeated, while if it is larger, in order to verify the correctness of the detection, the Slave FSM search starts running. Detection is performed at the Slave FSM, selecting within the RUR the cell corresponding to the largest correlation value, and comparing this value with a threshold ξ_S. If the selected value is lower than the threshold the Slave FSM execution breaks and the Master FSM is restarted; it is then evident that this solution allows to jointly accomplish a very fast verification of the Master decision cell and to execute the Slave FSM research. On the other hand, if the value surpasses the

Uni-directional CBA procedure;
while *1* **do**
  Master Search;
  Correlation is evaluated for all the possible CUR code delays to be tested;
  The greatest correlation is compared with the threshold ξ_M ;
  The correspondent code delay is selected;
  if the correlation is lower than the threshold ξ_M **then**
    Master Search is repeated;
  else
    if the selected code delay is an H_1 cell **then**
      the code delay information is sent to the Slave band acquisition engine;
      Slave Search is executed ;
    else
      an error occurs, and after tracking failure;
      Master Search is repeated;
    end
  end

  Slave Search;
  Correlation is evaluated for all the possible RUR code delays to be tested;
  The greatest correlation is compared with the threshold ξ_S ;
  The correspondent code delay is selected;
  if the correlation is lower than the threshold ξ_S **then**
    Slave Search is repeated;
  else
    if the selected code delay is an H_1 cell **then**
      Acquisition is completed;
    else
      an error occurs, and after the tracking failure;
      Slave Search is repeated;
    end
  end
end

Algorithmus 6 : Unidirectional acquisition procedure

threshold, the cell is selected. Whenever the chosen cell is an H_0 cell, tracking fails and the search needs to be restarted. Since it is not possible to know if the error is caused by the Master or the Slave FSM, the Master FSM is always restarted. Finally, when an H_1 cell is chosen, acquisition is completed. The described approach results in the algorithm detailed in Algorithm 7

Bi-directional CBA procedure;
while *1* **do**
  Master Search;
  Correlation is evaluated for all the possible CUR code delays to be tested;
  The greatest correlation is compared with the threshold ξ_M;
  The correspondent code delay is selected;
  if the correlation is lower than the threshold ξ_M **then**
    Master Search is repeated;
  else
    Slave Search is executed;
  end

  Slave Search;
  Correlation is evaluated for all the possible RUR code delays to be tested;
  The greatest correlation is compared with the threshold ξ_S;
  The correspondent code delay is selected;
  if the correlation is lower than the threshold ξ_S **then**
    Master Search is repeated;
  else
    if the selected code delay is an H_1 cell **then**
      Acquisition is completed;
    else
      an error occurs, and after the time needed for verification **Master Search** is repeated
    end
  end
end

Algorithmus 7 : Bidirectional acquisition procedure

It is interesting to note that the proposed approach is perfectly suitable for some of the problems described in the introduction. In particular it can be efficiently used for the hierarchical code acquisitions, in which the acquisition of the primary codes is carried out in the Master FSM, and the acquisition of the secondary codes is carried out in the Slave FSM, for the rake receiver detection problem and, again, for the multiple navigation satellite signal acquisition. On the other hand, the exploitation could result difficult in scenarios in which the two FSMs could be characterized by different conditions, e.g., different SNR conditions: as a matter of facts, since the two machines are

tightly coupled the FSM in the worst condition could afflict the behavior of both.

4.4 ANALYTICAL ACQUISITION TIME EVALUATION

The performance evaluation for the proposed dyadic FSM code acquisition approaches can be carried out by means of a semi-analytical tool based on flow-graphs. More in details, the described FSMs and synchronization procedures can be modeled as Markov chains and can be represented by associated flow-graphs, with nodes representing the states of the chain, and arcs representing the transitions between the states [49],[50],[13]. Each arc is characterized by a weight depending on the probability associated to the transition from one state to the other and on the time required for executing the starting state operations.

The analytical evaluation of the acquisition performance of the different proposed approaches can be carried out exploiting the concepts developed in [49],[50] and [13]. In particular, these frameworks provide the analytical tools which allow evaluating the MAT $\bar{T}_A$, on the basis of the probabilities of transition between one state to the other and of the associated transition times, as well as the Acquisition Time (T_A) and Cumulative Density Function (CDF). More in details, the MAT $\bar{T}_A$ and the acquisition time variance σ^2 can be evaluated by means of the flow-graph transfer function $P_A(z)$, according to:

$$\bar{T}_A = \left.\frac{\partial P_A(z)}{\partial z}\right|_{z=1} \tag{85}$$

$$\sigma^2 = \left[\frac{\partial^2 P_A(z)}{\partial z^2} + \frac{\partial P_A(z)}{\partial z} - \left(\frac{\partial P_A(z)}{\partial z}\right)^2\right]_{z=1} \tag{86}$$

Finally, the CDF can be effectively approximated according to the following:

$$\Pr\{T_A < T_{out}\} = \int_0^{T_{out}} \frac{t^{a-1} e^{-t/b}}{b^a \Gamma(a)} dt \tag{87}$$

with

$$a = \frac{\bar{T}_A^2}{\sigma^2_{T_A}} \tag{88}$$

$$b = \frac{\sigma^2}{\bar{T}_A} \tag{89}$$

Naturally, the analytical description provides results in a continuous domain, while being code-acquisition a discrete process, the actual domain of the acquisition time is discrete. However, it provides an accurate evaluation of the performance, thus granting a general tool suitable for the design of the acquisition sub-system.

In the following sections, the flow-graphs associated to the previously described procedures are derived and analyzed, and the analytical expressions of the MAT and of the acquisition time variance are provided.

4.4.1 *Single FSM Code Acquisition*

The single FSM acquisition associated with the procedure detailed in Section 4.2, can be described according to the flow-graph represented in Fig. 29:

- Initially the “Search" state is entered, during which the research of the H_1 cell in the CUR is performed. In order to perform this operation a time T_S is required.
- When an H_1 hypothesis is selected at the detection stage, with probability of detection P_D, then a transition from the search state (Search) to the correct acquisition state (ACQ) takes place.
- When a missed detection is obtained, with probability P_{md}, then the search state is re-entered.
- When the maximum decision is in correspondence of an H_0 cell, with probability of error $P_E = 1 - P_D - P_{md}$, then the transition is to the non-absorbing error state (ERROR), from which the detector exits after a penalty time T_P, which is the processing time spent before the tracking system fails.

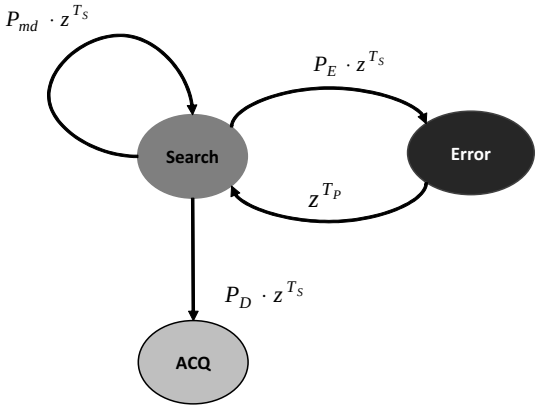

Figure 29: Flow graph of the overall acquisition procedure in the case of single FSM code acquisition.

The arcs connecting the nodes represent the costs due to the transition from one state to the following. By reducing the flow-graph, the following transfer function is obtained [49]:

$$P_A(z) = \frac{P_D z^{T_S}}{1 - P_{md} z^{T_S} - P_E z^{T_S + T_P}} \tag{90}$$

which translates into the following Mean Acquisition Time:

$$\bar{T}_{A,SB} = \frac{dP_A(z)}{dz}\Big|_{z=1} = \frac{T_S + P_E T_P}{P_D} \tag{91}$$

and the following variance

$$\begin{aligned}\sigma^2_{SB} &= \left[\frac{d^2P_A(z)}{dz^2}+\frac{dP_A(z)}{dz}-\left(\frac{dP_A(z)}{dz}\right)^2\right]_{z=1} \\ &= \frac{1}{P_D^3}\Big[(P_D-P_D^2)T_S^2+2P_EP_DT_ST_P+ \\ &\quad +P_ET_P^2\left((P_{md}-1)^2-P_E(P_D+P_E)\right)\Big]\end{aligned} \tag{92}$$

In case two FSM need to be executed to obtain two acquisition procedures, the overall required time is achieved as a combination of the times needed by each FSM. In particular, if the two acquisitions can be executed in parallel, the overall time required is equal to the maximum between the two acquisition times. On the other hand, in case the two FSMs are executed sequentially (e.g. with limited computational resources), the overall time would be equal to the sum of the times required for each FSM.

4.4.2 *Unidirectional Information Exchange*

The unidirectional procedure described in Section 4.3.1 can be represented by the flow-graph shown in Fig. 30.

- Code Acquisition commences when the Master FSM Search state is entered, during which the research of the H_1 cell is perfomed by scanning the CUR (Master Search). Also in this case a Master Search Time T_{SM} is required.
- When a maximum decision variable corresponding to a H_1 hypothesis occurs, with probability of detection P_{DM}, then a transition from the search state (Master Search) to the correct acquisition state (Master ACQ) takes place.
- When a missed detection is obtained, with probability $P_{md,M}$, then the Master search state is re-entered.
- In case an H_0 cell is selected, with probability of error $P_{EM} = 1 - P_{DM} - P_{md,M}$, then the non-absorbing error state (ERROR) is entered, from which the detector exits after the penalty time T_{PM}.
- After a time T_C, the control is passed to the Slave FSM, and the Slave Search state is entered. Similarly to the master FSM, a Slave Search Time T_{SS} is required.
- When an H_1 hypothesis occurs, with probability of detection P_{DS}, then a transition from the search state (Slave Search) to the correct acquisition state (Slave ACQ) takes place.
- When a missed detection is obtained, with probability $P_{md,S}$, then the Slave search state is re-entered.
- If an H_0 cell is selected, with probability of error $P_{ES} = 1 - P_{DS} - P_{md,S}$, then the error state (ERROR) first, and then the Slave search states are entered.

By reducing the flow-graph, the following transfer function results:

$$P_A(z) = \frac{A(z)}{B(z)C(z)} \tag{93}$$

with

$$\begin{aligned} A(z) &= P_{DM}P_{DS}z^{T_{SM}+T_{SS}+T_C} && (94)\\ B(z) &= 1-P_{EM}z^{T_{SM}+T_{PM}}-(1-P_{DM}-P_{EM})z^{T_{SM}} && (95)\\ C(z) &= 1-P_{ES}z^{T_{SS}+T_{PS}}-(1-P_{DS}-P_{ES})z^{T_{SS}} && (96) \end{aligned}$$

which translates into the following Mean Acquisition Time:

$$\bar{T}_{A,UD} = T_C + \frac{(T_{SM}+P_{EM}T_{PM})}{P_{DM}} + \frac{(T_{SS}+P_{ES}T_{PS})}{P_{DS}} \tag{97}$$

and the following variance

$$\begin{aligned} \sigma^2_{UD} = \frac{1}{P^2_{DM}P^2_{DS}}\Big[& P^2_{DS}\Big((1-P_{DM})T^2_{SM}+2P_{EM}T_{SM}T_{PM}+ \\ & +P_{EM}(P_{DM}+P_{EM})T^2_{PM}\Big)+ \\ & +P^2_{DM}(T_{SS}+P_{ES}T_{PS})^2+P^2_{DM}P_{DS}\left(-T^2_{SS}+P_{ES}T^2_{PS}\right)\Big] \end{aligned} \tag{98}$$

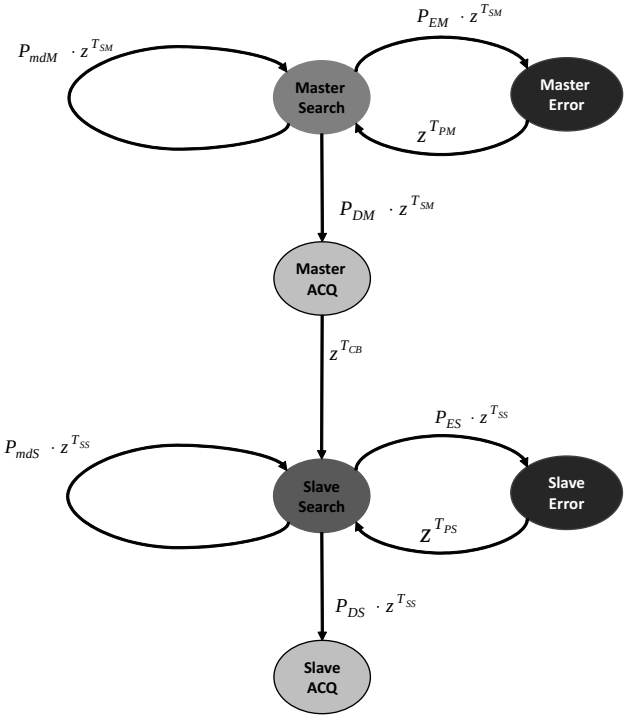

Figure 30: Flow graph of the overall acquisition procedure in the case of a fast Master

Equation (97) clearly shows that the MAT is equal to the sum of T_C and the MAT required by the Master FSM, searching the CUR, and by the Slave FSM, searching the RUR. Accordingly, it is possible to foresee that the MAT will reduce w.r.t. the sequential acquisition performed by two autonomous FSMs.

4.4.3 *Bi-directional Information Exchange*

Finally, the BD approach described in Section 4.3.2 can be represented by the flow-graph represented in Fig. 31:

- initially the Master search state is entered and the research of the H_1 hypothesis is carried out by scanning the CUR. Similarly to the previous cases, a Master Search Time T_{SM} is required to perform the operations.
- When an H_1 hypothesis occurs, with probability of detection P_{DM}, then a transition from the master search state to the slave search "Full" state takes place.
- In case missed detection is obtained, then the research is repeated.
- On the other hand, when an H_0 cell occurs, with probability of error $P_{EM} = 1 - P_{DM} - P_{md,M}$, then the transition is to the search state (Slave Search "Empty") happens.
- From the Slave Search "Empty" state, after scanning the RUR if the maximum decision variable is below the threshold, then transition to the Master Search state occurs, with correct rejection probability P_r. On the other hand, if the maximum decision variable surpasses the threshold, then the transition is to the non-absorbing error state (ERROR), with probability $(1 - P_r)$. From the ERROR state the detector exits after a penalty time T_{PS}, and the Master FSM restarts the search over the CUR.
- From the Slave Search "Full" state, after scanning the RUR, when the maximum decision variable is below the fixed threshold, then the Master Search state is re-entered, with missed detection probability $P_{md,S}$. On the other hand, if the maximum decision variable surpasses the threshold two transition can be envisaged: a transition to the correct acquisition state (Master/Slave ACQ) with probability P_{DS}, or a transition to the non-absorbing error state (ERROR) with probability $(1 - P_{DS} - P_{md,S})$, from which the detector exits after a penalty time T_{PS}.

The resulting transfer function is thus:

$$P_A(z) = \frac{A(z)}{1 - (B(z) + C(z) + D(z))} \tag{99}$$

where

$$\begin{aligned} A(z) &= P_{DM} P_{DS} z^{T_{SM} + T_{SS} + T_C} \\ B(z) &= (P_{EM}) z^{T_{SM} + T_C} [P_r z^{T_{SS}} + (1 - P_r) z^{T_{SS} + T_{PS}}] \\ C(z) &= P_{DM} z^{T_{SM} + T_C} \left[P_{mdS} z^{T_{SS}} + (1 - P_{DS} - P_{mdS}) z^{T_{SS} + T_{PS}}\right] \\ D(z) &= (1 - P_{DM} - P_{EM}) z^{(T_{SM})} \end{aligned} \tag{100}$$

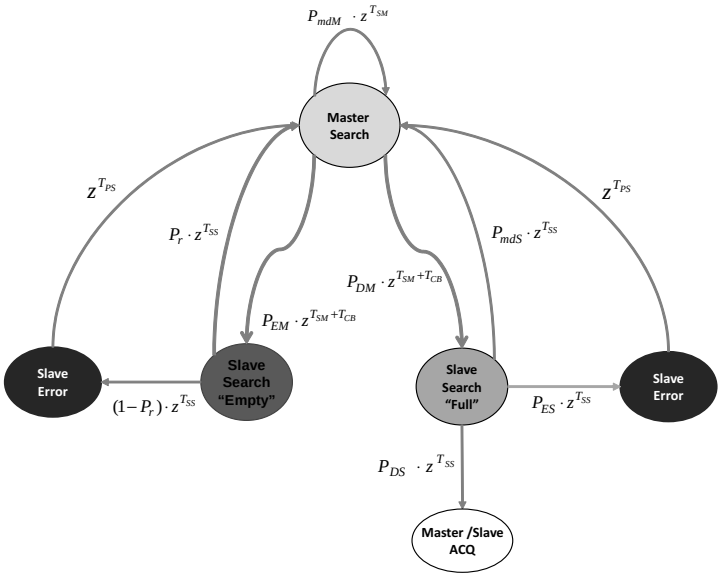

Figure 31: Flow graph of the overall acquisition procedure, in case of a slow Master case and MAX decision Slave.

which translates into the following Mean Acquisition Time:

$$\begin{aligned}\bar{T}_{BD} &= \frac{1}{P_{DM}P_{DS}}\Big[T_{SM}+P_{DM}\Big(T_C+(1-P_{DS}-P_{mdS})T_{PS}+T_{SS}\Big)+\\ &\quad +P_{EM}(T_C+T_{PS}-P_rT_{PS}+T_{SS})\Big] \qquad (101)\end{aligned}$$

and the following acquisition time variance

$$\begin{aligned}\sigma^2_{BD} &= \frac{1}{P^2_{DM}P^2_{DS}}\Big\{(T_{SM}+P_{EM}(T_C+T_{PS}-P_rT_{PS}+T_{SS}))^2+\\ &\quad P^2_{DM}\Big[(1-P_{DS})T^2_C+(-1+P_{mdS})(P_{DS}-1+P_{mdS})T^2_{PS}+\\ &\quad -2(P_{DS}-1+P_{mdS})T_{PS}T_{SS}-(P_{DS}-1)T^2_{SS}+\\ &\quad -2T_C((P_{DS}-1+P_{mdS})T_{PS}+(P_{DS}-1)T_{SS})\Big]+\\ &\quad -P_{DM}\Big[T_{SM}(2(P_{DS}-1)T_C+2(P_{DS}-1+P_{mdS})T_{PS}+\\ &\quad +P_{DS}T_{SM}+2(P_{DS}-1)T_{SS})+P_{EM}\Big((P_{DS}-2)T^2_C+\\ &\quad -(P_{DS}-2+2P_{mdS})(-1+P_r)T^2_{PS}+\\ &\quad +2(P_{DS}-2+P_{mdS}+P_r)T_{PS}T_{SS}+\\ &\quad +(P_{DS}-2)T^2_{SS}+2T_C((P_{DS}-2+P_{mdS}+P_r)T_{PS}+\\ &\quad +(P_{DS}-2)T_{SS})\Big)\Big]\Big\} \qquad (102)\end{aligned}$$

4.5 STUDY CASE: DUAL BAND GALILEO AIDED ACQUISITION

In order to demonstrate the efficacy of the proposed approach a practical application is presented in the following. As in [18], the focus of the study is on a dual-band receiver for the Galileo system [1], operating in the Open Service bands E1 (1575.42 MHz) and E5 (1191.795

MHz). In this case both the UD and the BD approaches can be usefully applied, thus it constitutes a perfect example to demonstrate the effectiveness of the proposed approaches and to compare their performance. Primary code acquisition is analyzed in this work, considering the pilot channels of both the E1 and E5 signals, i.e. E1c and E5aQ signals [1].

4.5.1 *Signal Structure*

Galileo E5 signal is designed to have a chip rate $R_{c,E5} = 10.23$ Mega chips per second (Mcps), which is equal to ten times the E1 signal chip-rate $R_{c,E1} = 1.023$ Mcps. The E5 signal primary code length is equal to 10230 chips, while the length of the E1 primary code is 4092. Accordingly the E5 code duration is equal to 1ms, and the E1 code duration is equal to 4 ms. This means that there are 4 E5 code repetitions every E1 code, and that the E1 chip duration $T_{c,E1}$ is exactly ten times longer than the E5 chip duration $T_{c,E5}$, as summarized in table 15 [1]. Being the E1 code duration a multiple of the E5 one, the signals

Table 15: Galileo E1 and E5 main signal characteristics

Primary Code	E1	E5
Code Length	4092	10230
Chip Rate R_c	1.023 Mcps	10.23 Mcps
Code Period T_{code}	4 ms	1 ms
Chip Period T_c	977.51 ns	97.75 ns

are always time aligned, hence the acquisition of one of the signals provides a useful information for the acquisition of the second. In particular two cases are possible:

- in case the Master FSM performs the acquisition of the E1 signal and the Slave FSM of the E5 signal (E1-E5 configuration), assuming the acquisition of the E1 signal to return an H_1 characterized by a code delay error $\delta_{E1} \in [-T_{c,E1}/2, T_{c,E1}/2]$, the Slave FSM uncertainty period is equal to one E1 chip period, corresponding to 10 E5 chip periods. Assuming to take one hypothesis per E5 chip period, the RUR consists of 10 code delay hypotheses, as illustrated in Figure 32
- in case the Master FSM performs the acquisition of the E5 signal and the Slave FSM of the E1 signal (E5-E1 configuration), since the E1 code period is four times longer than the E5 code period, the Slave FSM RUR consists of 4 code delay hypotheses, separated by 1 ms between each other, as illustrated in Figure 33

Finally, it is worth to observe that the Galileo Signal In Space Interface Control Document [1] indicates a Total Received Minimum Power (TRMP) for the entire E5 signal of -152 dBW. On the other hand, the

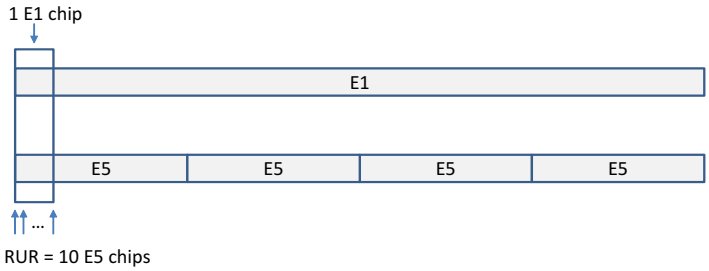

Figure 32: E1-E5 signal relation

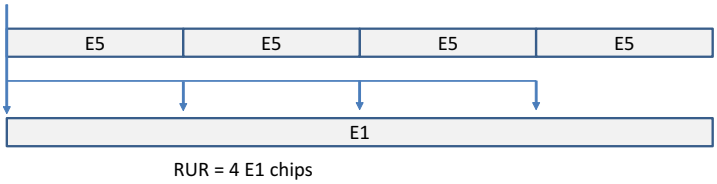

Figure 33: E5-E1 signal relation

E1 TRMP is equal to −157 dBW. Thus, the entire E5 signal is 5 dB more powerful than the E1 signal, resulting in a difference of 5 dBHz also in terms of signal power over noise power spectral density C/N_0.

4.5.2 *Receiver Architecture*

The models provided in Section 4.4 rely on the times needed to perform the procedures associated to each state of the FSMs. In the following we detail the operations needed to execute the different procedures, hence determining the relative minimum time requirements.

The dwell time T_{SM} spent by the Master code acquisition subsystem in order to perform the search in the CUR (which coincide with the time T_S of the single FSM code acquisition), comprises the time needed to load the buffer with L signal code periods T_{code}, to be used as observables in the correlation stage, and the additional time needed to complete the processing required to explore the UR T_{scan}:

$$T_{SM} = L_M T_{code} + T_{scan} \tag{103}$$

The actual delay due to computation can vary according to the architecture adopted for the implementation of the acquisition subsystem: parallel architectures can strongly limit the processing time, while in case only limited resources are available, the required time becomes much longer.

Similarly, the dwell time T_{SS} spent by the slave code acquisition subsystem to perform the search operations, comprises the time $L_S T_{code,S}$ needed to record L_S code periods of the incoming signal, the observables, and the additional time $T_{scan,S}$ needed to complete the operations.

When considering the search over the whole CUR (Master search, or single FSM search), we fix the number of observed codes $L_M = 1$, which maximizes the efficiency of the implementation by means of

FFT/IFFT [55]. As a matter of fact, the FFT/IFFT implementation efficiency is maximized when the number of correlations to be evaluated is equal to the number of samples of the FFT/IFFT: if $L > 1$ is used, the length of the FFT must be increased and the complexity increases, while the number of hypotheses to be tested does not change. On the other hand, the number of observed periods L_S can be increased when considering the slave band processing. Due to the small number of code delay hypotheses composing the RUR (4 or 10 hypotheses according to the model described in Section 4.5.1), correlations can be calculated by means of correlators and the computational load is lower w.r.t. the master FSM. Different values of L_S are considered in the following, ranging from 1 to 8, in order to solve the performance-complexity trade-off. Neglecting the additional time T_{scan}, the minimum times needed to perform the Master and Slave search operations are:

$$T_{SM,E1} = 4 \text{ ms} \quad (104)$$

$$T_{SM,E5} = 1 \text{ ms} \quad (105)$$

$$T_{SS,E1} = 4L_S \text{ ms} \quad (106)$$

$$T_{SS,E5} = L_S \text{ ms} \quad (107)$$

The penalty time T_P, needed to exit from the Error state, is equal to the time spent between the instant at which the detection is performed and the instant at which the tracking operations break: assuming the tracking subsystem to start correlating immediately after the detection, and that it breaks immediately after the prompt correlation has been calculated, T_P can be set equal to the integration time of the tracking prompt correlator. Accordingly, the penalty times $T_{P,E1}$, $T_{P,E1}$ are equal to:

$$T_{P,E1} = 25\ T_{code,E1} = 100 \text{ ms} \quad (108)$$

$$T_{P,E5} = 100\ T_{code,E5} = 100 \text{ ms} \quad (109)$$

The two period durations are evaluated considering the tiered Galileo code strcture [1], consisting of a primary and of a secondary code.

Finally, the time T_C, required to exchange information between the two acquisition engines, can be neglected due to the fact that the two FSMs should be executed in the same device and no delays are present due to information transmission.

4.6 NUMERICAL RESULTS

In the following the performance evaluation is carried out for the different approaches, and the MAT and acquisition time CDF are shown.

In order to optimize the system and choice the values of L_S leading to the best performance-complexity trade-off, the behavior of the MAT versus L_S is shown for different signal to noise ratios. In figure 34 the results obtained for the two approaches Bi-Directional and Uni-Directional, and for the two configurations, E1-E5 and E5-E1, are presented, considering $C/N_{o,E1}$ ranging from 35 to 45 dB, and, equivalently, $C/N_{o,E1}$ ranging from 40 to 50 dB. The figures show that for

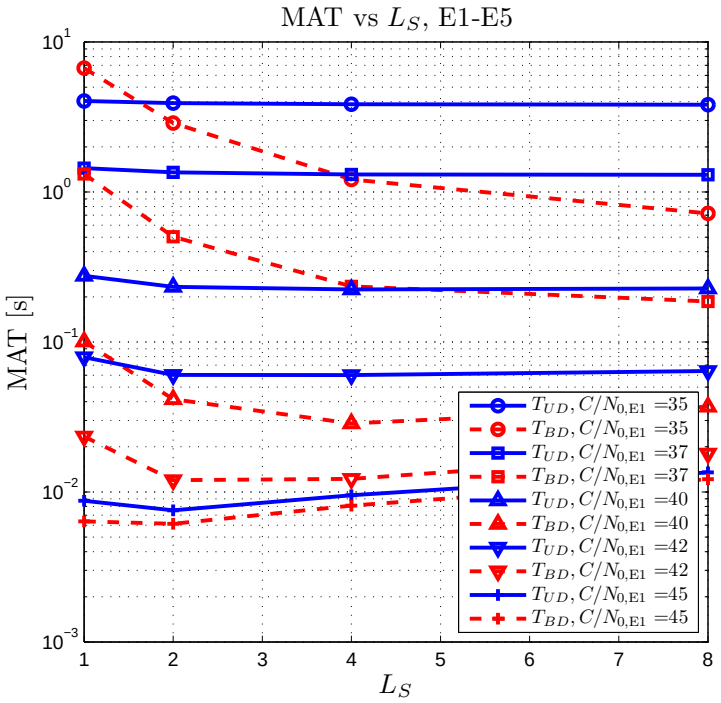

(a) E1-Master, E5-Slave

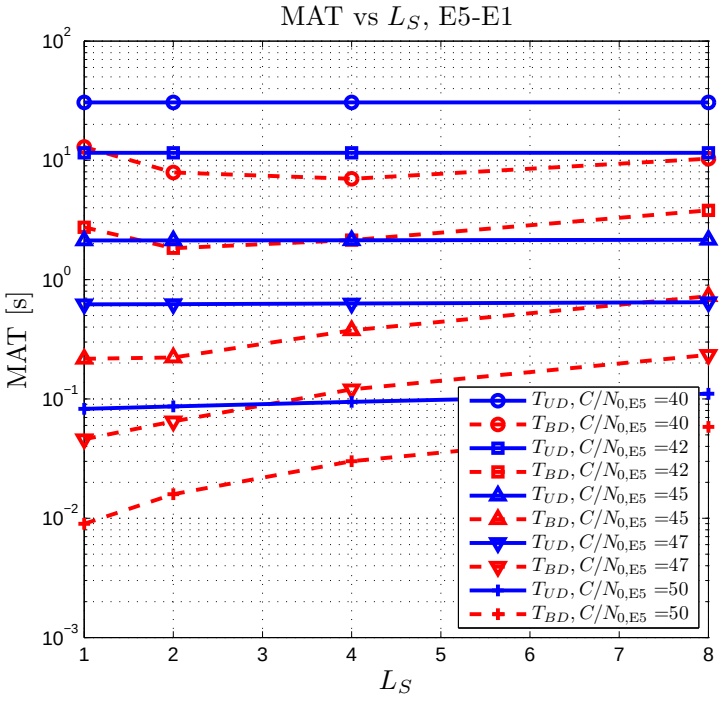

(b) E5-Master, E1-Slave

Figure 34: MAT vs L_S: system optimization

different C/N_0 the values of L_S leading to the best performance variate, for both the E1-E5 and the E5-E1 configurations. In particular, in the E5-E1 configuration the best performance is obtained for $L_S = 4$ or for $L_S = 8$, but in the high SNR case, when the $L_S = 2$ is optimum. Since for high SNR the loss is just in the order of some milliseconds, $L_S = 4$ is chosen. On the other hand, in the E5-E1 configuration, $L_S < 4$ leads to the best performance: in this case, we chose observation length $L_S = 2$. From these figures it is also possible to observe that the E1-E5 configuration clearly outperform the E5-E1 configuration, hence, in the following, only the E1-E5 is considered.

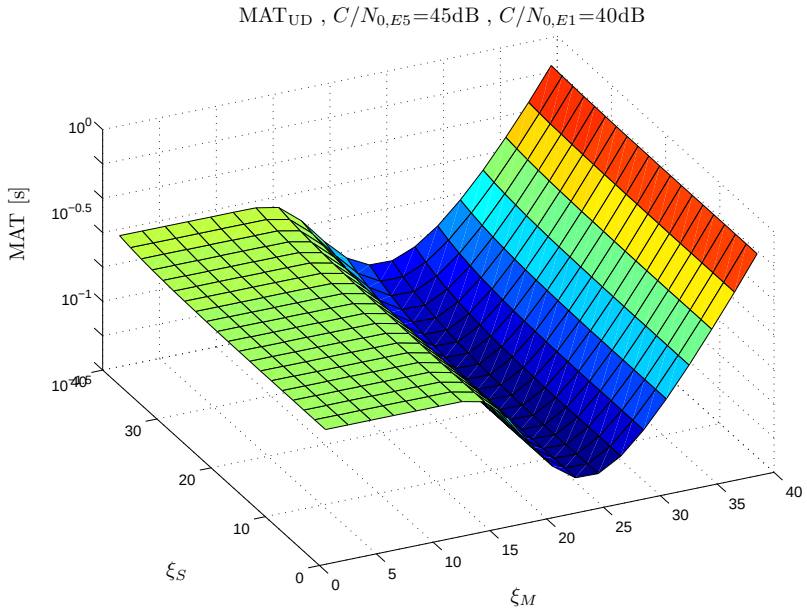

(a) UD MAT E1-Master, E5-Slave

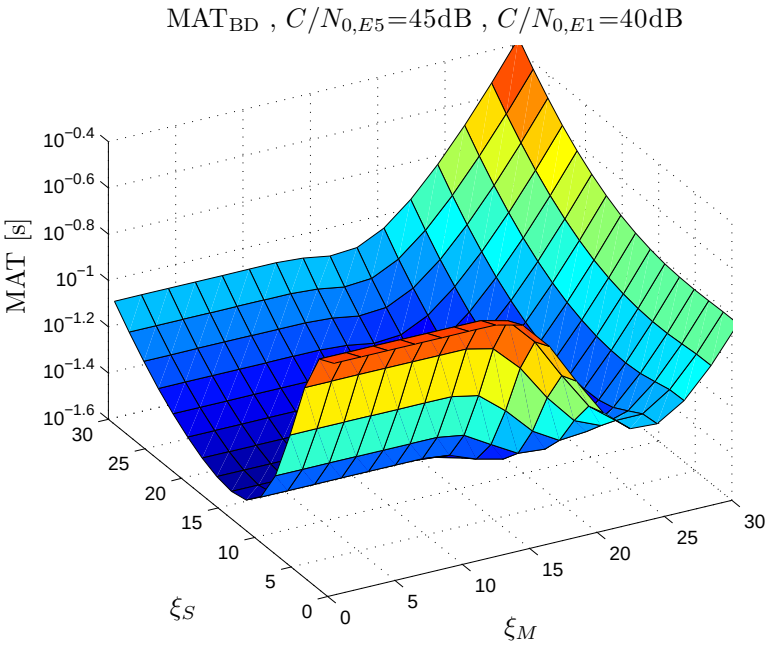

(b) BD MAT E1-Master, E5-Slave

Figure 35: MAT dependance on the ξ_M and ξ_S thresholds

Considering the selected L_S values, the qualitative behavior of the MAT with respect to the values of the thresholds ξ_M and ξ_S, for both the UD and the BD approaches, is presented in figures 35 (a) and (b), considering a fixed SNR value ($C/N_{0,E1} = 40dB$, $C/N_{0,E5} = 45dB$). From Fig. 35(a) it is possible to observe that the MAT strongly depends on the value of the Master threshold ξ_M, while the dependance on ξ_S is very weak: this means that for the UD approach, most of the algorithm complexity is solved in the Master FSM, without any feedback information from the Slave FSM, while in the BD approach, the Slave FSM actively contributes to the reduction of the acquisition performed searching the CUR. The optimum threshold values, for both the UD and the BD approaches, at different SNR levels, are reported in Table 16; for the sake of completeness also the E1 single band acquisition optimum thresholds are reported. It is possible to observe that the optimum ξ_M for the UD approach coincide with the optimum ξ for the E1 single band acquisition; on the other hand, the threshold values for the BD Master acquisition are lower,meaning that with the BD higher error probability is allowed, because errors are rapidly detected with the verification performed exploiting the Slave detection.

Table 16: Optimum thresholds

		E1	UD		BD	
$(C/N_{0,E1}$	$C/N_{0,E5})$	ξ	ξ_M	ξ_S	ξ_M	ξ_S
35	40	23	23	11	17	11
37	42	23	23	11	17	11
40	45	25	25	11	19	13
42	47	25	25	11	19	17
42	47	25	25	7	17	23

The best MAT values obtained using the threshold previously identified are shown in Fig. 36. From this figure it is possible to observe that:

- the slowest SB acquisition MAT (E5) and the sequential independent acquisition MAT (E1+E5) are always very similar: this means that the slowest FSM (the one acquiring the E5 signal), by itself, determines most of the acquisition time of the sequential approach;
- UD can strongly enhance the performance of the acquisition with respect to the single band acquisitions case: for all of the analyzed SNRs, the E1-E5 UD approach strongly reduces the MAT with respect to the E5 single band acquisition. This means that this approach could be effectively exploited also for the acquisition of the E5 signal alone.
- the BD approach allows to further improve the performance with respect to the UD approach, thanks to the feedback from

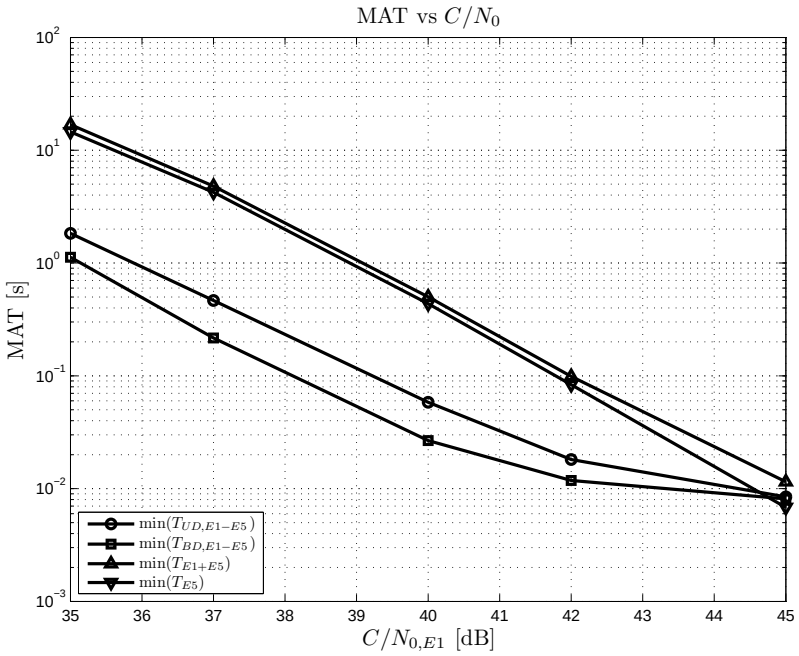

Figure 36: Mean Acquisition Time versus C/N_0 dB

the Slave FSM which rapidly allows to recover from erroneous detection performed by the Master FSM

The improvement results to be practically negligible in case of very high SNR, due to the fact that the classical acquisition probability of detection is almost equal to 1, hence, the error states are never entered.

Finally, assuming to stop the acquisition after a time T_{out}, in order to avoid deadlocks due to the actual absence of a determined satellite signal, it is useful to evaluate the probability that the overall acquisition is completed in less than T_{out}, i.e. the CDF of the acquisition time. The CDF for the different approaches are shown in figure 37, 38, and 39 for three different SNR (which are the lowest considered SNR), and still using the threshold previously identified. The results reflect the behaviors already observed for the MATs: also in this case the E1-E5 BD approach leads to the best performance, maximizing the CDF. It is possible to note that already at $C/N_{0,E1} = 37$ dBHz the CDF of the BD approach is equal to 0.98, and the CDF of the UD is equal to 0.84, which demonstrate that the two proposed approaches strongly enhance the performance with respect to the case of the two FSM executed independently. Since the BD approach does not introduce any additional complexity with respect to the UD approach, it constitutes the best candidate for the solution of the dual band acquisition problem. Furthermore, according to the results, the BD approach results to have better performance also with respect to the E5 single band acquisition, thus suggesting that it would be beneficial also for systems which need to acquire the only E5 signal.

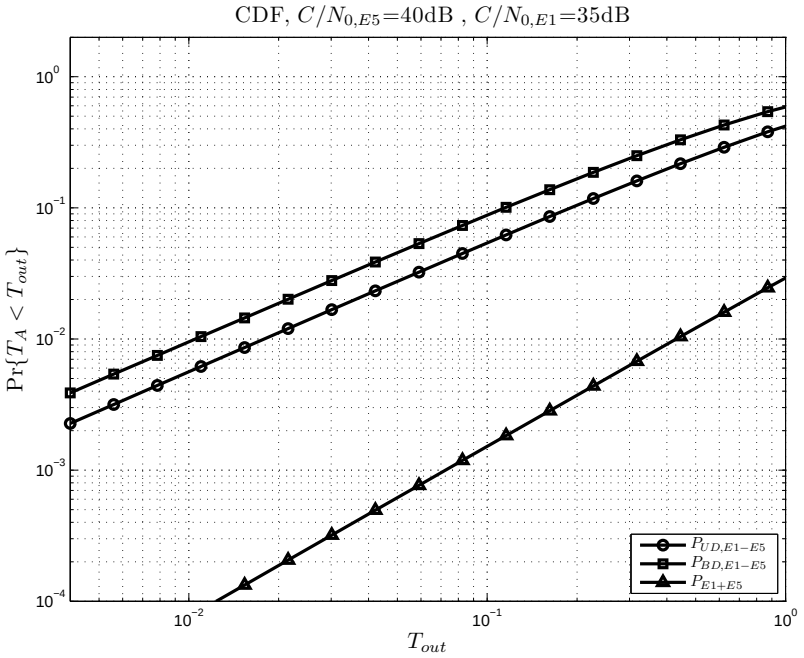

Figure 37: Cumulative Density Function: $C/N_{0,E5} = 40, C/N_{0,E1} = 35$

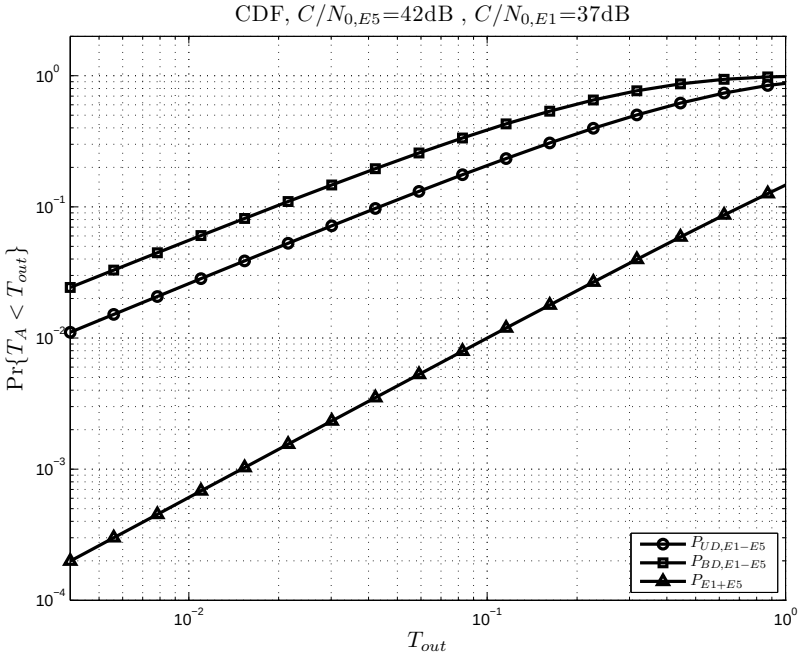

Figure 38: Cumulative Density Function: $C/N_{0,E5} = 42, C/N_{0,E1} = 37$

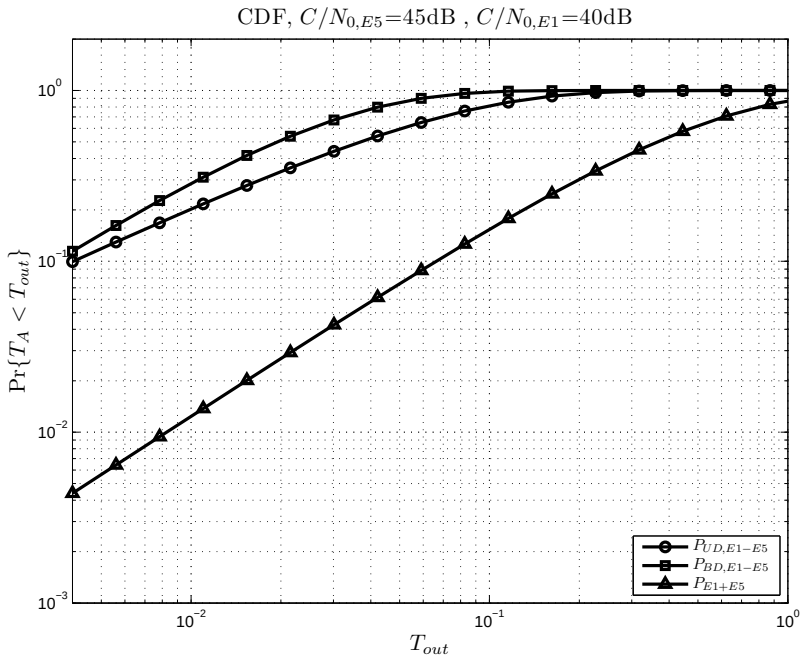

Figure 39: Cumulative Density Function: $C/N_{0,E5} = 45$, $C/N_{0,E1} = 40$

4.7 CONCLUSIONS

In this chapter an effective approach for pairs of FSMs performing code epoch synchronization is introduced. The algorithm relies on the exchange of timing information between the FSMs with the aim of improving the overall acquisition performance while limiting complexity. Different approaches have been presented, considering both unidirectional information flow from one FSM to the other, and bidirectional flow. We assessed the performance of these schemes analytically by exploiting the corresponding flow-graph representation. Furthermore, a realistic application has been analyzed, considering the scenario of a dual band Galileo receiver. The numerical results show that the proposed approaches allow to obtain strong advantages both with respect to the case of two FSMs performing acquisition separately, and even with respect to slowest FSM performing acquisition standalone. Moreover, all these results are obtained without the need of modifying the correlators and without increasing the computational complexity of the overall system.

5

CODE-ACQUISITION IN P2P NAVIGATION NETWORKS

5.1 INTRODUCTION

In previous chapter a method for the optimization of code synchronization for multiple FSMs is introduced, based on the optimization of the strategy carried out after detection. In this chapter, still considering a network of cooperating GNSS receivers, an optimized detection technique is proposed. The research is motivated considering wireless smart devices cooperating among each other.

The great diffusion of hybrid Navigation-Communication (NAV-COM) devices provides the means for developing new cooperation concepts that rely on the exploitation of the existing communication links among receivers and the exchange of assistance information. The concept of P2P cooperation relies in fact on the idea that receivers belonging to the same network have positions which are correlated to each other; thereby, satellite signals are received with similar time delays. The exchange of timing information and the sharing of resources can thus become essential also for GNSS receiver initial operations as for achieving increased acquisition capabilities in very low SNR scenarios.

In the present work an innovative CCA technique relying on the sharing of primary code phase information is introduced. Assuming that the peers in the network are aligned to a common time reference, the aim of this technique is to increase the probability of detection (P_d) with positive impacts on the MAT. The proposed CCA algorithm is performed in two consecutive stages: a Coarse Acquisition Stage Coarse Acquisition Stage (CAS), in which each peer computes locally its autocorrelation values and a Refinement Stage (RS) in which the results obtained by several receivers in the network are combined together yielding improved performance. The described algorithm is also presented in [P7]

5.2 INTRODUCTION

In this context, the Assisted-GNSS Assisted GNSS (A-GNSS) technique allows to reduce the uncertainty region by employing base station broadcasted information about visible satellites and Doppler frequency [63]. This assistance information, however, is provided to all the users in the coverage area and it is not tailored to the user position and it does not account for the local environment. On the other hand, the pervasive diffusion of GNSS users, and the even greater distribution of hybrid NAV-COM devices, have laid the foundations for developing innovative cooperation schemes based on the concept of P2P cooperation. The P2P paradigm is built on the idea that devices in a limited

area, can share very accurate assistance information exploiting existing available communication links. For the information exchange, data formats and communication protocols should be accurately chosen to best match the application scenario. Suitable protocols could be the 802.11p Wireless Access for Vehicular Environments (WAVE), ZigBee or others; on the other hand exchanged data format can rely either on the modification of existing standards, as the A-GNSS or the RTCM SC-104 v3, or on the definition of brand new ad-hoc standards.

The literature on P2P schemes based on GNSS data is rather scarce but in recent years many efforts are being devoted to the study of new cooperative techniques. In [40], [45] and [42] cooperative techniques operating at physical level with peers sharing Doppler shift, secondary code and Carrier to Noise density ratio (C/N_0) information are presented.

Differently from the cited techniques, in the present work an innovative CCA technique relying on the sharing of primary code phase information is introduced. Supposing that the peers in the network are aligned to a common time reference, the aim of this technique is to improve acquisition performance in terms of MAT and Pd by exploiting all available information in the network. In this work two different strategies have been proposed, yielding interesting results in terms of MAT and P_d.

5.3 SYSTEM MODEL

In the satellite navigation contest signals are transmitted according to a Code Division Multiplexing (CDM) approach, which allows to discriminate amongst different transmitting satellites through the use of orthogonal sequences. Every satellite transmits a fixed number of signals, which are multiplexed by exploiting frequency division.

Considering an AWGN channel the baseband equivalent of the signal transmitted by the i-th satellite and received by the k-th peer can be expressed as

$$\tilde{s}_R^{i,k}(t) = \tilde{s}_T^i(t-\tau_k)e^{j2\pi\Delta f_k t+\theta_k} + \eta_k(t) \tag{110}$$

where $\tau_k, \theta_k, \Delta f_k$ are respectively the time delay, phase rotation, and Doppler frequency offset introduced by the channel, and $\eta_k(t)$ is the AWGN with power spectral density equal to $N_{0,k}$.

Being time synchronization the objective of this work, in the following we will concentrate only on the time parameter estimation. The effect of phase rotation on synchronization can in fact be neglected by considering non-coherent detection schemes, while frequency effects can be eliminated by adopting a multiple frequency test approach. In the present work, a P2P network comprised of multiple receivers able to communicate between each other is considered.

In the following we will distinguish between the absolute time reference system and the k-th peer local reference system. The residual time delay of the signal in the k-th peer time reference τ_k is obtained considering the time delay introduced by the propagation and the

k-th peer time reference in the absolute reference system. τ_k can be expressed as:

$$\tau_k = |\tau_{S,R_k} - \tau_{0,k}|_{T_{code}} \tag{111}$$

where τ_{S,R_k} is the time delay introduced by the channel between the satellite and the k-th peer expressed in the absolute reference system, $\tau_{0,k}$ is the k-th peer time reference in the absolute reference system, and $T_{code} = LT_c$, where L is the length of the PN code in chips. Note that τ_{S,R_k} can be expressed as

$$\tau_{S,R_k} = \frac{\rho_{S,R_k}}{c} + T_{Iono} + T_{Tropo} + T_{e_k} \tag{112}$$

where we hypothesize that all signals are transmitted at time instant o of the absolute reference system, ρ_{S,R_k} is the geometrical range between the satellite and the k-th peer, c is the speed of light in vacuum, T_{Iono} is the delay introduced by the Ionosphere, T_{Tropo} is the delay introduced by the Troposphere, and T_{e_k} takes into account additional errors affecting the propagation delay (e.g multi-path). T_{Iono} and T_{Tropo} can be estimated according to models and coefficients broadcast in the navigation message, and can therefore be easily computed for all peers in the network. On the other hand ρ_{S,R_k} is not known at the receiver and differs slightly for each peer in the network. In fact, the receivers in the network occupy in general different positions and thus receive the transmitted signals with different delays that are nonetheless limited due to the reduced region of space in which the peers are dislocated. More in detail, since the distances between the peers are assumed to be less than several hundreds of meters, the difference between each τ_{S,R_k} is contained and limited to 1 us. Additional multi-path errors may differ between peers and impact on the computed propagation time. However, it is worthwhile noting that in indoor scenarios relative delays between received paths are in the order of a few ns while in outdoor environments it is reasonable to affirm that acquisition can be carried out considering the line of sight path only. Thus, during the code acquisition phase the effect of multipath can be neglected.

Moreover, in the following, the peers are assumed to have synchronized clocks, meaning that all the receivers share the same time reference with some accuracy. Different synchronization strategies can be adopted, yielding a final timing misalignment upper bounded by the latencies in exchanging synchronization messages in the network, as presented in [61], [62] and [34]. It is possible to envisage a synchronization strategy between the peers that relies on the transmission by a reference node (P_0) of a beacon signal to all neighboring devices. Substituting equation (112) into (111) it is possible to express τ_k as:

$$\tau_k = \left| \frac{\rho_{S,R_0}}{c} + T_{Iono} + T_{Tropo} - \tau_{0,0} - \epsilon_k \right|_{T_{Iono}} \tag{113}$$

where ρ_{S,R_0} is the distance between the satellite and P_0, $\tau_{0,0}$ is the time reference of peer P_0, and ϵ_k is introduced to take into account both the different distances between receivers and satellite and the

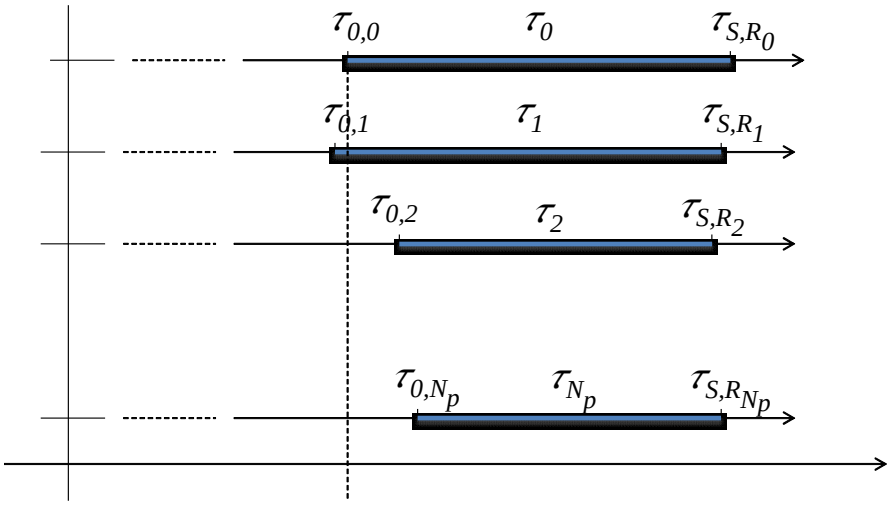

Figure 40: Graphic representation of time references and measures.

residual misalignment error caused by the imperfect clock synchronization procedure. The additional term ϵ_k is modeled as a Gaussian random variable with zero mean and variance σ_ϵ^2.

Therefore it is possible to write τ_k as

$$\tau_k = |(\tau_{S,R_0} - \tau_{0,0}) - \epsilon_k|_{T_{code}} \tag{114}$$

that is the difference between the unknown deterministic value $(\tau_{S,R_0} - \tau_{0,0})$, that can be treated as a random variable uniformly distributed between $[0, T_{code}]$, and the error ϵ_k.

It is important to note that τ_k can be expressed as the sum of an integer discrete delay and a fractional delay, that is:

$$\tau_k = \Delta_k T_c + \delta_k \tag{115}$$

5.4 CODE ACQUISITION IN A P2P NETWORK

5.4.1 *Rationale*

The purpose of code acquisition is to obtain a coarse estimation of the time delay τ_k, that is, the correct detection of the value Δ_k of the discrete time delay. Under the assumption of a network of peers able to synchronize between each other the τ_k values will be very similar and can be statistically characterized. This consideration leads to envisaging the estimation of the time delays of the different peers jointly by exploiting the information exchanges in the network.

The considered network is comprised of $N_P + 1$ peers, with a reference device P_0 and N_P neighboring devices that send aiding information.

The CCA procedure is performed in two successive stages, the CAS and the RS: during the CAS the peer performs local computations in order to identify a reduced set of possible code delay hypotheses; in the RS information regarding the code delay sets selected by the neighboring peers is exploited to identify the correct hypothesis. It is

worthwhile noting that the selected sets could be the results of either the aiding peer CAS, or its tracking phase.

5.4.2 *Maximum Likelihood Cooperative Delay Detection*

In the following we will consider time discrete signals, with sampling period equal to the chip period T_c. Let $\bar{s}_k^{(i)}(m)$ be the vector of samples of the signal received by the k-th peer shifted by mT_c seconds, with $m \in \Sigma = \{0, 1, 2, \ldots, L-1\}$. Let P_0 be the peer exploiting the CCA algorithm. During the CAS P_0 calculates the LR $\lambda_0^{(i)}(m)$ for the i-th signal, and selects the set Σ_0, sub-set of Σ, comprising the M_0 code delays m corresponding to the largest $\lambda_0^{(i)}(m)$. $\lambda_0^{(i)}(m)$ is calculated according to:

$$\lambda_0^{(i)}(m) = \frac{p(\bar{s}_0^{(i)}(m)|H_1)}{p(\bar{s}_0^{(i)}(m)|H_0)} \tag{116}$$

where $p(\bar{s}_0^{(i)}(m)|H_j)$, $j = 0, 1$ is the multivariate conditional probability of observing $\bar{s}_0^{(i)}(m)$ under H_j ($j = 0, 1$). Let us consider the sets Σ_k comprising the M_k largest $\lambda_k^{(i)}(m)$ collected by each peer P_k, and let Λ be the set of all the code delay identified by the peers,

$$\Lambda = \left[\Sigma_{M_0}, \Sigma_{M_1}, \Sigma_{M_2}, \ldots, \Sigma_{M_{N_p}}\right] \tag{117}$$

After collecting the sets Σ_k from the neighboring peers, Λ is exploited by P_0 to start the RS, during which the code delay $\hat{\Delta}_0$ that minimizes the error probability is selected. Since no a priori information is available for Δ_0, the optimal decision strategy operates according to the ML criterion that can be formally expressed as:

$$\hat{\Delta}_0 = \arg\max_{\Delta_0} p(\Lambda|\Delta_0) \tag{118}$$

where $p(\Lambda|\Delta_0)$ is the conditional probability density function (pdf) of the observation set given the effective delays Δ_0.

Characterization of the detection algorithm is obtained analyzing the probabilities $p(\Lambda|\Delta_0)$. Assuming the sets Σ_k to be statistically independent, it is possible to define:

$$p(\Lambda|\Delta_0) = \prod_{k=0}^{N_p} p(\Sigma_k|\Delta_0) \tag{119}$$

By exploiting the total probability theorem, every term of the sum can be rewritten as:

$$p(\Sigma_k|\Delta_0) = \sum_{\Delta_k=0}^{L-1} p(\Sigma_k|\Delta_0, \Delta_k) p(\Delta_k|\Delta_0) \tag{120}$$

It is worthwhile noting that:

$$p(\Sigma_k|\Delta_0, \Delta_k) = p(\Sigma_k|\Delta_k)$$

since the probability of selecting Σ_k only depends on the code delay at the k-th peer, and it is not affected by the code delay at P_0, equation (119) becomes:

$$p(\Sigma_k|\Delta_0) = \sum_{\Delta_k=0}^{L-1} p(\Sigma_k|\Delta_k)p(\Delta_k|\Delta_0) \tag{121}$$

Substituting equation (121) into (120) the conditional probability can finally be expressed as

$$p(\Lambda|\Delta_0) = \prod_{k=0}^{N_p} \sum_{\Delta_k=0}^{L-1} p(\Sigma_k|\Delta_k)p(\Delta_k|\Delta_0) \tag{122}$$

It is possible to note that $p(\Sigma_k|\Delta_k)$ takes into account the probability of obtaining the set Σ_k under the hypothesis that the code delay is equal to Δ_k, thus it is a probability totally determined by the realization of the signal at the k-th peer, while $p(\Delta_k|\Delta_0)$ is completely determined by the network configuration and the clock synchronization process between the peers. The detection criterion can thus be expressed as:

$$\hat{\Delta}_0 = \arg\max_{\Delta_0} \left(\prod_{k=0}^{N_p} \sum_{\Delta_k}^{L-1} p(\Sigma_k|\Delta_k)p(\Delta_k|\Delta_0) \right) \tag{123}$$

It is possible to observe that quite complex operations have to be performed in (123), since the sum of a large number of elements must be calculated. In order to reduce the complexity of the algorithm a simplification can be performed by limiting the inner sum to the terms belonging to Σ_k that leads to:

$$\hat{\Delta}_0 = \arg\max_{\Delta_0} \left(\prod_{k=0}^{N_p} \sum_{\Delta_k \in \Sigma_k} p(\Sigma_k|\Delta_k)p(\Delta_k|\Delta_0) \right) \tag{124}$$

This assumption is justified by the fact that in case $\Delta_k \in \Sigma_k$ the value of $p(\Sigma_k|\Delta_k)$ is much larger than when $\Delta_k \notin \Sigma_k$ which helps reducing the complexity of the algorithm.

Moreover, since the CCA combining is performed locally in the peer processing unit, the choice of M_k should be carried out in order to maximize the probability of detecting the correct peer code delay, while at the same time minimizing the complexity of the combining phase and the amount of exchanged information. Thus peer P_0 could use M_0 different from M_j ($j \neq 0$).

The probability $p(\Sigma_k|\Delta_k)$ cannot be calculated in closed form, but the problem can be tackled by considering a sub-optimal approach based on the Maximal Ratio Combining (MRC) approach [11]. In MRC the information collected from different paths is weighted proportionally to the signal amplitudes. In this case the probability $p(\Sigma_k|\Delta_k)$ can be assumed linearly proportional to the values $\lambda_k^{(i)}(m)$ of the LRs. With this approximation the problem reduces to:

$$\hat{\Delta}_0 = \arg\max_{\Delta_0} \left(\prod_{k=0}^{N_p} \sum_{\Delta_k \in \Sigma_k} \lambda_k^{(i)}(m)p(\Delta_k|\Delta_0) \right) \tag{125}$$

The algorithm described by equation (125) is identified as CCA-SC. It is worth noting that to implement SC the knowledge of the $\lambda_k^{(i)}(\Delta_k)$ values must be available to P_0. The SC algorithm can be tuned by choosing the M_k parameter in order to maximize the performance in different application scenarios.

A simpler but still effective approach can be obtained by neglecting the weights $\lambda_k^{(i)}(\Delta_k)$, and by deciding according to:

$$\hat{\Delta}_0 = \arg\max_{\Delta_0} \left(\prod_{k=0}^{N_p} \sum_{\Delta_k \in \Sigma_k} \lambda_k^{(i)}(m) p(\Delta_k|\Delta_0) \right) \tag{126}$$

Therefore all the information sent by the different peers are weighted in a uniform way, by not considering the measurements of the signal amplitude. The algorithm defined by equation (126) is identified as CCA-HC. Clearly this approach, which is derived from an ulterior approximation of the ML equation, will lead to a less reliable synchronization; this, however, can be justified by a reduction of the overall algorithm complexity and required data traffic on the network.

5.5 PERFORMANCE EVALUATION

The performance of the algorithms has been evaluated in terms of Probability of Detection (P_d), MAT and of Mean Complexity (MC). P_d is calculated by means of Monte Carlo simulations, while MAT and MC are derived in a semi-analytical way, through the solution of a Markov chain. The acquisition procedure can be in fact modeled as a FSM, as reported in Figure 41. State S is the Search state, in which

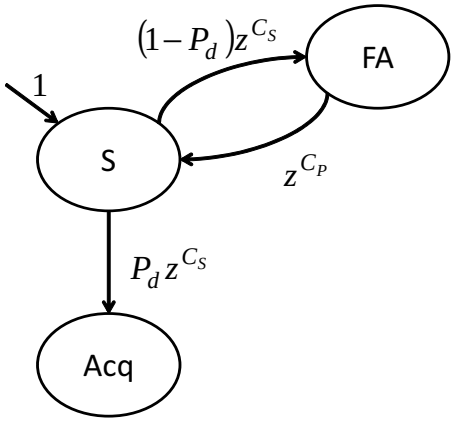

Figure 41: Markov Chain associated to the CCA procedure

the CCA procedure is performed, FA is the False Alarm State and Acq is the Acquisition state. The graph reports on the branches the costs C_S and C_P corresponding to the search and the penalty stages respectively. For the MAT computation the costs represent the time needed to perform the scan of the uncertainty region, while for the MC the costs take into account the number of operations.

When the receiver is initialized the S state is entered and after performing the acquisition a code delay hypothesis is chosen. If the correct code delay hypothesis is chosen the Acq state is entered; on the

Table 17: Arithmetic operation complexity in terms of basic operations

Arithmetic Operation	Basic Operations
real multiplication	1 op
real sum	1 op
complex sum	2 op
complex multiplication	6 op
FFT butterfly	10 op
$\max(a_1, \ldots, a_N)$	2(N-1) op

contrary, if a wrong hypothesis is chosen the transition is to the FA state. In the FA state a verification procedure is started to check if the chosen hypothesis is correct.

It is possible to show that the final cost (MAT or MC) can be derived as:

$$C = \frac{C_S + (1 - P_d)C_P}{P_d} \tag{127}$$

Substituting in equation (127) the values of P_d found through simulations and the costs C_S and C_P, it is possible to evaluate MAT and MC for both classical acquisition and CCA approaches. In the following sections, performance comparisons, in different scenarios and varying algorithm configurations will be carried out.

5.5.1 *Costs characterization*

The values considered for C_S and C_P in the classical and CCA procedures are reported in the following. For the MAT the costs $C_S = T_S$ and $C_P = T_P$ are considered, where T_S is the time needed to perform the search of the correct code delay hypothesis, and T_P is the time needed to recover from a false alarm event. Since the search between the L delay hypotheses requires the observation of at least a signal code period, T_S is set equal to T_{code}. Assuming that recovery from a false alarm state is performed by testing 5 times the same code delay hypothesis, T_P is set equal to $5T_{code}$. These values are considered both for the classical code acquisition procedure and the CCA.

For the computation of the MC, the number of arithmetical operations needed to perform the search and the verification stage has been derived. In the following the cost of every arithmetical operation has been expressed in terms of basic operations (op) according to the values listed in Table 17 and in [41]. Finally the overall MC has been derived in terms of basic operations. For the classical code acquisition procedure (carried out according to the MAX criterion), assuming a parallel search strategy, implemented using an L_2-points FFT, where L_2 is the minimum power of 2 larger than L, it is possible to show that the cost C_S, expressed in terms of number of operations due to the execution of the search operation is:

$$C_S = N^A_{op-S} = 10L_2 \log_2 L_2 + 6L_2 + 3L + 2(L-1) \tag{128}$$

On the other hand, still assuming that parallel search is performed, the cost C_S for the CCA implemented according to the SC strategy equals to:

$$C_S = N_{op-S}^{CCA-SC} = 10L_2 \log_2 L_2 + 6L_2 + 3L + 2M(L-1) + N_p M_0 M^2 \tag{129}$$

while for the HC strategy the cost is given by:

$$C_S = N_{op-S}^{CCA-HC} = 10L_2 \log_2 L_2 + 6L_2 + 3L + 2M(L-1) + N_p M_0 M \tag{130}$$

where N_p is the number of peers sharing aiding information, M_0 is the cardinality of the set Σ_0, and M the cardinality of the sets Σ_k ($k \neq 0$). Assuming a verification stage performed by testing 5 times the same code delay hypothesis, the cost C_P expressed in terms of number of operations needed to recover from the FA state can be expressed as:

$$C_P = N_{op-P} = 5(L(6+2)) \tag{131}$$

Note that this value is valid both for the classical code acquisition search procedure and the CCA procedure. The obtained expressions can thus be used in the following to derive the complexity evaluations.

5.5.2 *Simulation Scenario*

Code acquisition performance depends largely on the number of considered code delay hypotheses that have to be tested. In this work the E1B-C BOC modulated GALILEO signal has been taken into account, which is characterized by a primary code of length L=4092. The simulation scenario has been characterized by considering a variable number of aiding peers (N_p=1,3,5,10), different C/N_0 values ranging from 32 to 40 dB-Hz, and a clock synchronization variance equal to 10^{-10} s^2, which is a largely conservative value given that the clock synchronization procedure should guarantee an accuracy in the order of the propagation delay [62].

The HC and SC procedures have been tested in the different scenarios, testing varying M_k values. In particular we distinguished between the cardinality M_0 of peer Po, which is exploiting CCA to acquire the signal, and the cardinality M_k ($k = 1, \ldots, N_p$) of its neighboring peers, that has been set equal to M.

5.6 NUMERICAL RESULTS

The most typical scenario that can be envisaged is characterized by a receiver that needs to acquire a satellite signal, surrounded by peers that are already locked to the satellite. Figure 42 shows the comparison between the P_d obtained by a peer performing the search according to the classical code acquisition approach and to the CCA-SC strategy, when 5 aiding peers with signal to noise ratio after correlation

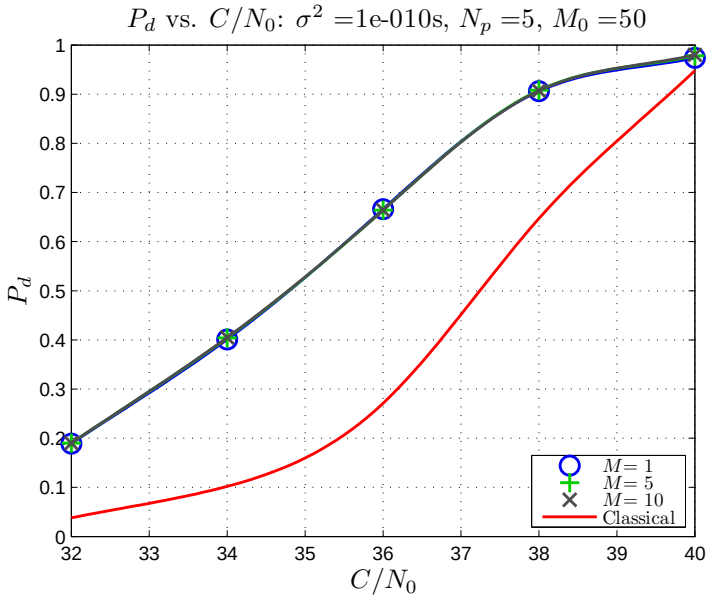

Figure 42: Comparison between classical acquisition and CCA-SC acquisition procedure with M0=50

equal to 16 dB are present. The variance of the clock synchronization process has been set equal to 10^{-10} s^2 and the CCA-SC is characterized by $M_0 = 50$, and $M = (1, 5, 10)$. It is possible to observe that a large improvement in terms of P_d is obtained in particular at low SNR values. By reducing the number of code delays identified during the CAS (M_0), the behaviors in Figure 43 with M=1, M=5 and M=10 (blue, green and grey curves respectively) are obtained. It is worthwhile noting that even if considerable improvements with respect to the classical procedure can be obtained, in this case the achievable values of P_d are smaller than in the previous configuration with M_0 =50. Larger M_0 values allow thus to increase the probability of selecting the correct time delay during the CAS. The strength of the CCA-SC procedure is evident in the rapid growth of the resulting P_d, that corroborates the effectiveness of its RS. It is worth noting that even if the number of aiding peers decreases the performance of the CCA-SC algorithm remains good, as demonstrated by the curves reported in Figure 44. This result is quite interesting as it demonstrates that also if the peer density in a certain area is low the algorithm is still effective. The performance of the CCA-HC procedure is shown in Figure 45. It is possible to observe that the CCA-HC strategy leads to less reliable synchronization with respect to the CCA-SC: in particular, the P_d achievable in case only one aiding peer is present (curve marked with circles) does not have a good behavior, but in case 5 aiding peers are present (cross marked curve) performance similar to the CCA-SC is still reachable. In fact, by collecting large M_0 sets the probability of selecting code delay hypotheses close to the correct delay increases, and since in the CCA-HC strategy all hypotheses are weighted the same, also the probability of error increases. On the other hand the presence of more peers allows to average out the presence of outliers. In order to completely characterize the algorithm the

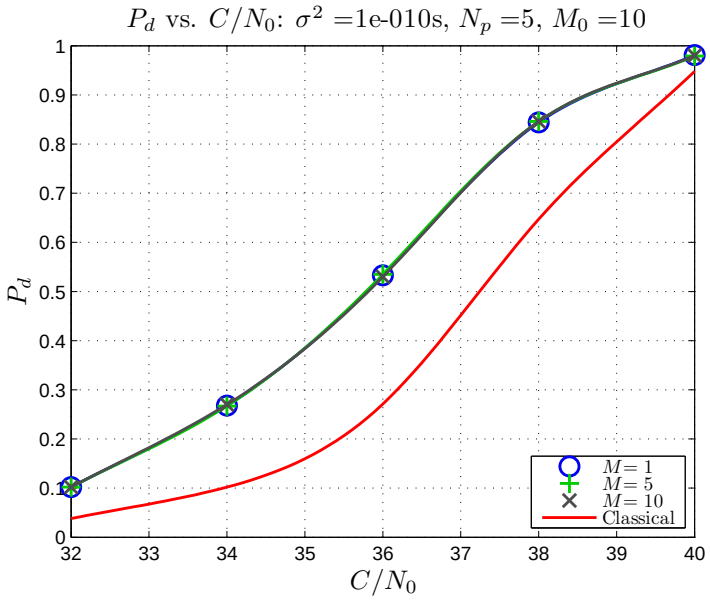

Figure 43: Comparison between classical acquisition and CCA-SC acquisition procedure with M0=10

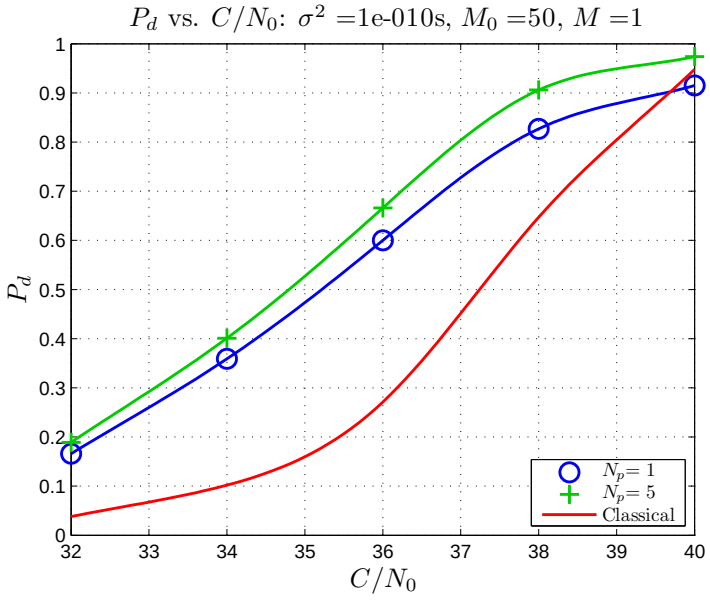

Figure 44: Comparison between classical and CCA-SC performance with varying numbers of aiding peers

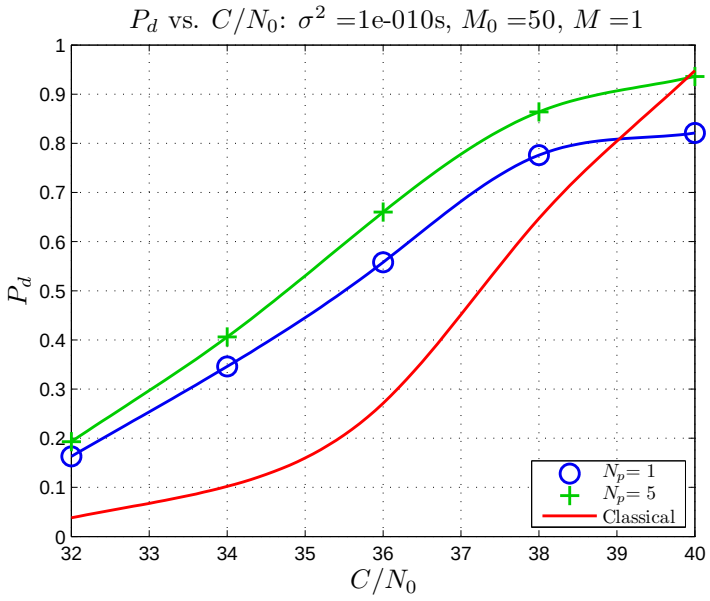

Figure 45: Comparison between classical acquisition and CCA-HC strategies

performance has been evaluated also in terms of MAT. In Figure 46 the comparison between the MAT obtained with the classical code acquisition procedure and the CCA-SC with M=1 is reported. At low SNR values the time needed to acquire the signal with the CCA-SC is almost an order of magnitude smaller than the time needed by the classical strategy; the gain decreases with increasing SNRs, converging to the same value for C/N_0 values greater than 40 dBHz. It is worth noting

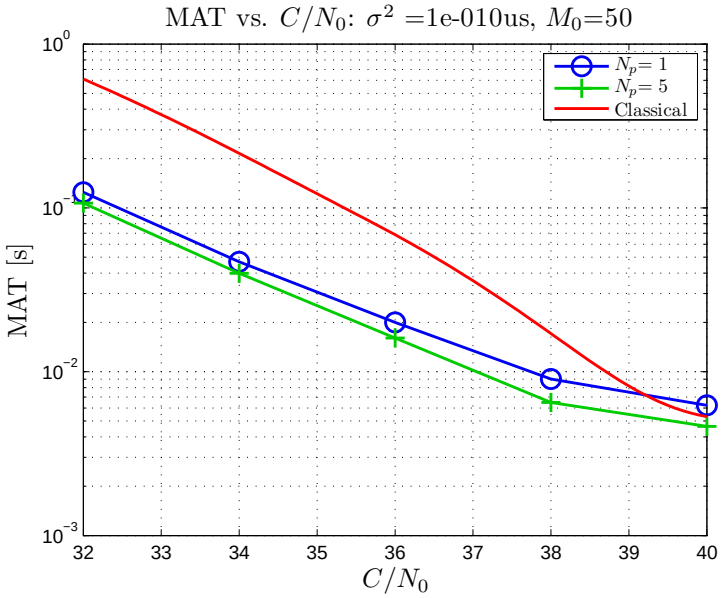

Figure 46: Comparison between classical acquisition and CCA-SC strategies MATs

that the performance for the $N_P = 1$ and $N_P = 5$ cases are very similar, this is due to the fact that, as reported in Figure 42, in both cases the similar P_d are achieved. The performance improvement in terms of MAT is achieved without requiring a corresponding complexity in-

crease at the receiver with the case M=1, as shown in Figure 47: in particular, for the N_P=1 and $N_P = 5$ cases the number of operations is smaller that needed for the classical acquisition. This demonstrates that by tuning the algorithm parameters it is possible to consistently improve the effectiveness of the code acquisition procedure, without a corresponding increase in the algorithm complexity.

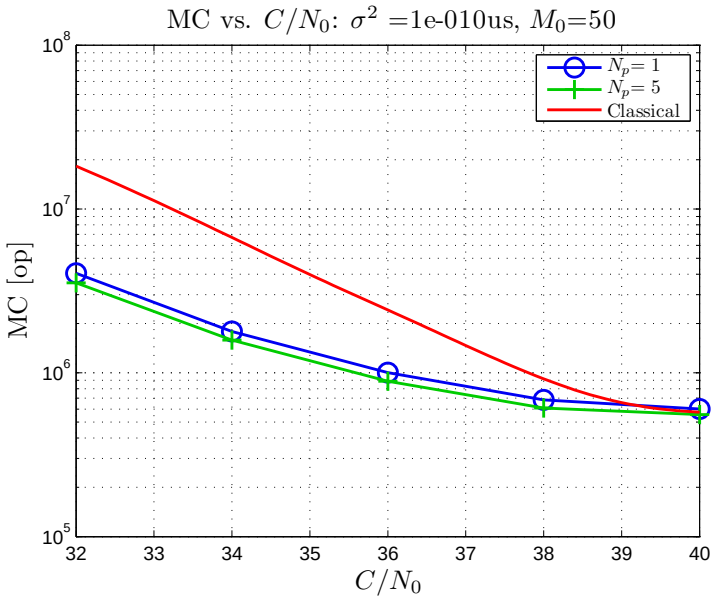

Figure 47: Comparison between classical acquisition and CCA-SC strategies MCs

5.7 CONCLUSIONS

In this work the novel CCA procedure has been introduced with the aim of improving receiver performance especially at low SNR values while limiting at the same time complexity. The concept relies on the exchange of information between neighboring peers, which is feasible due to the great diffusion of smart NAV-COM devices able to collaborate. The strong correlation of the satellite signal delays for the different peers, due to the closeness of the devices, has been exploited in order to maximize the useful information. It has been shown that compelling improvements can be achieved in terms of P_d, and consequently of MAT, without increasing the algorithm complexity. The CCA-SC consistently outperforms the classical approach, leading to good performance enhancements, in particular at low SNR. This approach constitutes an interesting alternative to receivers using longer integration times, but for real-time implementation several aspects must be taken into account: in particular the clock synchronization between the nodes must be sufficiently accurate to guarantee the significance of the exchanged information; moreover an effective protocol targeted to the transmission of GNSS physical layer information must be tailored, in order to optimize the data exchange. In the context of the future Internet of Things (IoTs) deployment, where it is easy

to envisage a pervasive presence of P2P networks, this strategy could constitute a compelling solution to the synchronization problem.

CODE SYNCHRONIZATION TECHNIQUES: FURTHER DEVELOPMENTS

Code synchronization will continue to be the basis for any SS system. It constitute the initial operation for any receiver, and research on this matter will continue to appear, every time that new scenarios or more complex systems will be taken into consideration.

In this work it has been shown as the scenario considered for TT&C systems gives origin to the new challenge of code synchronization in large frequency uncertainty and under strong frequency dynamics. Further solutions could be envisaged for the code synchronization scheme, performing the research of the signal parameters in the three-dimensional space of the code-epoch, frequency, and Doppler-rate parameters. We expect that the complexity increases, but it should lead to a very accurate solution in a single step. Furthermore, completely different schemes could be foreseen, considering differential integration techniques, which would strongly reduce the frequency uncertainty domain, at the cost of increased noise level.

Furthermore, we have shown how cooperation can improve the overall performance of a system consisting of multiple FSMs performing code synchronization. Two different cooperation techniques have been proposed, consisting in exchanging information regarding the detected cell, but further cooperation approaches could be invented.

In conclusion, different and increasingly complex systems will give origin to new challenges, which will need to be solved in different ways by a mixture of creativity and technical knowledge.

CONCLUDING REMARKS

We have studied methods for the enhancement and of the SS navigation and communication system capabilities. As a matter of fact, the development of techniques aimed to enable SS adoption is required, in order to exploit their advantages. The contribution of this thesis goes towards two directions:

- the design of interference management techniques, aimed to enhance the performance of an interference detection and localization system, and to perform interference cancellation from the signal observed at the receiver;
- the extension of code synchronization capabilities to particularly harsh scenarios characterized by a large frequency uncertainty and strong frequency dynamics, and the optimizion of code epoch synchronization techniques for cooperating receivers.

The first topic has been tackled in part I of this dissertation. In particular an interference detection and localization system based on the analysis of the CC of the signals received at different sensor nodes has been considered and analyzed. An analytical model for the GNSS signal CC has been proposed and its accuracy has been evaluated with respect to the correspondent function evaluated numerically. Starting from this model, an algorithm for the cancellation of the clutter generated by the presence of GNSS signals has been introduced, in order to improve the interference detection and localization capabilities. Furthermore, considering a receiver observing a signal affected by interference, an interference cancellation algorithm has been designed, and its effectiveness has been demonstrated by means of computer simulations and emulations.

The second important contribution of this dissertation, i.e., the design of code synchronization techniques, has been addressed in part II. The motivation behind the study of code synchronization schemes is the necessity of enabling the adoption SS transmission in new challenging scenarios, and of optimizing synchronization in complex systems consisting of pairs or networks of nodes. Since next generation TT&C systems will require SS transmission, a code synchronization scheme able to perform the coarse estimation of the code epoch, carrier frequency and Doppler rate during the satellite LEOP phase has been designed. The proposed scheme allows to perform the estimation of the parameters without excessively increasing the complexity of the algorithm. Furthermore, considering complex systems consisting of pairs of FSMs performing code acquisition, optimized schemes have been introduced aimed to enhance the performance in terms of MAT without modifying the correlation algorithms. It has been shown how this optimization can strongly improve the code acquisition capabilities of the overall system, reducing time and power consumption.

Finally, considering a network of cooperating P2P receivers, a code epoch synchronization method has been designed with the aim of improving receiver performance especially at low SNR values while limiting at the same time complexity. It has been shown how the proposed technique effectively improves the capabilities thus constituting an interesting solution for code synchronization in the next future.

BIBLIOGRAPHY

[1] Galileo open service signal in space interface control document. Technical report, 2011.

[2] H. Akaike. A new look at the statistical model identification. *Automatic Control, IEEE Transactions on*, 19(6):716–723, 1974.

[3] J.B. Allen and L. Rabiner. A unified approach to short-time fourier analysis and synthesis. *Proceedings of the IEEE*, 65(11): 1558–1564, 1977.

[4] E. Anyaegbu, G. Brodin, J. Cooper, E. Aguado, and S. Boussakta. An integrated pulsed interference mitigation for gnss receivers. *The Journal of Navigation*, 61:239–255, 4 2008.

[5] A.T. Balaei, B. Motella, and Dempster A.G. Gps interference detected in sydney-austalia. In *International Global Navigation Satellite Systems Society IGNSS Symposium 2007, Proceedings of*, 2007.

[6] R. Bauernfeind, I. Kramer, H. Beckmann, B. Eissfeller, and V. Vierroth. In-car jammer interference detection in automotive gnss receivers and localization by means of vehicular communication. In *Integrated and Sustainable Transportation System (FISTS), 2011 IEEE Forum on*, pages 376–381, 2011.

[7] P. Bellocq and L. Simone. Tcr-tas-sp-72: Ss codes suitable for mono-mode tt&c transponder ss codes specifications: Ss codes specifications. Technical report, 2011.

[8] A. Bilich and K.M. Larson. It's not all bad: Understanding and using gnss multipath. *GPS World*, 20(10):31–39, 2009.

[9] D. Borio and L. Lo Presti. Mathematical models and gnss interference. *INSIDE GNSS*, March/April 2008:25–27, 2008.

[10] K. Borre. *A Software-Defined GPS and Galileo Receiver: A Single-Frequency Approach*. Applied and numerical harmonic analysis. Birkhäuser, 2007.

[11] D.G. Brennan. Linear diversity combining techniques. *Proceedings of the IEEE*, 91(2):331–356, 2003.

[12] E. Cetin, R.J.R. Thompson, and A.G. Dempster. Interference localization within the gnss environmental monitoring system (gems). In *International Global Navigation Satellite Systems Society IGNSS Symposium 2011, Procedings of*, 2011.

[13] G.E. Corazza. On the max/tc criterion for code acquisition and its application to ds-ssma systems. *Communications, IEEE Transactions on*, 44(9):1173–1182, 1996.

[14] G.E. Corazza and R. Pedone. Generalized and average likelihood ratio testing for post detection integration. *Communications, IEEE Transactions on*, 55(11):2159–2171, 2007.

[15] G.E. Corazza and D. Potuaud. Tcr-tas-an-103: Ss codes suitable for mono-mode tt&c transponder ss codes specifications: Analysis and trade-off for commercial applications. Technical report, 2011.

[16] G.E. Corazza, C. Caini, A. Vanelli-Coralli, and A. Polydoros. Ds-cdma code acquisition in the presence of correlated fading - part i: theoretical aspects. *Communications, IEEE Transactions on*, 52(7): 1160–1168, 2004.

[17] I. Daubechies. The wavelet transform, time-frequency localization and signal analysis. *Information Theory, IEEE Transactions on*, 36(5):961–1005, 1990.

[18] L. Deambrogio, F. Bastia, C. Palestini, R. Perdone, M. Villanti, and G.E. Corazza. Cross-band aided code acquisition in dual-band gnss receivers. *Aerospace and Electronic Systems, IEEE Transactions on*, 49(4):2533–2545, 2013.

[19] W.A. Gardner and C.M. Spooner. Comparison of autocorrelation and cross-correlation methods for signal-selective tdoa estimation. *Signal Processing, IEEE Transactions on*, 40(10):2606–2608, 1992.

[20] C. Gernot, K. O'Keefe, and G. Lachapelle. Assessing three new gps combined l1/l2c acquisition methods. *Aerospace and Electronic Systems, IEEE Transactions on*, 47(3):2239–2247, 2011.

[21] F. Gini, M.S. Greco, and A. Farina. Radar detection and preclassification based on multiple hypothesis. *Aerospace and Electronic Systems, IEEE Transactions on*, 40(3):1046–1059, 2004.

[22] J. C. Grabowski. Field observations of personal privacy devices. In *2012 International Technical Meeting of The Institute of Navigation, Proceedings of*, pages 689–741, 2012.

[23] M. Greco, F. Gini, and A. Farina. Radar detection and classification of jamming signals belonging to a cone class. *Signal Processing, IEEE Transactions on*, 56(5):1984–1993, 2008.

[24] K. Gromov, D. Akos, D. Pullen, and P. Enge. Gidl: Generalized interference detection and localization system. In *13th International Technical Meeting of the Satellite Division of The Institute of Navigation (ION GPS 2000), Proceedings of*, pages 447–457, 2000.

[25] L. Gupta, S. Kota, S. Murali, D.L. Molfese, and R. Vaidyanathan. A feature ranking strategy to facilitate multivariate signal classification. *Systems, Man, and Cybernetics, Part C: Applications and Reviews, IEEE Transactions on*, 40(1):98–108, 2010.

[26] J.K. Hwang and Y.C. Chen. A combined detection-estimation algorithm for the harmonic-retrieval problem. *Signal Processing*, 30(2):177 – 197, 1993.

[27] J.K. Hwang and Y.C. Chen. Superresolution frequency estimation by alternating notch periodogram. *Signal Processing, IEEE Transactions on*, 41(2):727–741, 1993.

[28] European Telecommunications Standards Institute. *ETSI TR 101 956 - V1.1.1, Satellite Earth Stations and Systems (SES); Technical Analysis of Spread Spectrum Solutions for Telemetry, Command and Ranging (TCR) of Geostationary Communications Satellites*. 2001-2009.

[29] European Telecommunications Standards Institute. *ETSI EN 301 926 - V1.2.1, Satellite Earth Stations and Systems (SES); Radio Frequency and Modulation Standard for Telemetry, Command and Ranging (TCR) of Geostationary Communications Satellites*. 2002-2006.

[30] O. Isoz and D. Akos. Development of a deployable low cost interference detection and localization system for the gnss l1/e1 band. In *Satellite Navigation Technologies and European Workshop on GNSS Signals and Signal Processing (NAVITEC), 2010 5th ESA Workshop on*, pages 1–4, 2010.

[31] E.D. Kaplan and C.J. Hegarty. *Understanding GPS: Principles and Applications*. Artech House mobile communications series. Artech House, 2005.

[32] S.M. Kay. *Fundamentals of Statistical Signal Processing: estimation theory. Volume 1*. Fundamentals of Statistical Signal Processing. PTR Prentice-Hall, 1993.

[33] S.M. Kay. *Fundamentals of Statistical Signal Processing: Detection theory*. Prentice Hall Signal Processing Series. Prentice-Hall PTR, 1998.

[34] H. Khaleel, M. Franceschinis, R. Tomasi, and M. Mondin. Accuracy-driven synchronization protocol:implementation and experimental evaluation. In *Proceedings of the International ACM Conference on Management of Emergent Digital EcoSystems (MEDES 2009)*, pages 369–376, 10/2009 2009.

[35] A. Konovaltsev, D. De Lorenzo, A. Hornbostel, and P. Enge. Mitigation of continuous and pulsed radio interference with gnss antenna arrays. In *Proceedings of the 21st International Technical Meeting of the Satellite Division of The Institute of Navigation (ION GNSS 2008)*, pages 2786–2795, September 2008.

[36] T. Kraus, R. Bauernfeind, and B. Eissfeller. Survey of in-car jammers-analysis and modeling of the rf signals and if samples (suitable for active signal cancellation). In *24th International Technical Meeting of The Satellite Division of the Institute of Navigation (ION GNSS 2011), Proceedings of*, pages 430–435, 2011.

[37] S. Kumar, J. Ghosh, and M.M. Crawford. Best-bases feature extraction algorithms for classification of hyperspectral data. *Geoscience and Remote Sensing, IEEE Transactions on*, 39(7):1368–1379, 2001.

[38] K.C. Kwon and D.S. Shim. Fast acquisition method for gps l1/l2c software receivers. In *Control, Automation and Systems (ICCAS), 2011 11th International Conference on*, pages 1612–1615, 2011.

[39] D.W. Lim, S. W. Moon, C. Park, and S. J. Lee. L1/l2cs gps receiver implementation with fast acquisition scheme. In *Position, Location, And Navigation Symposium, 2006 IEEE/ION*, pages 840–844, 2006.

[40] L. Lo Presti, D. Margaria, and J. Samson. A novel peer to peer aided acquisition strategy tailored to galileo e1 receivers. In *ELMAR, 2010 PROCEEDINGS*, pages 417–424, 2010.

[41] L. Lo Presti, M. Spirito, R. Garello, and G.E. Corazza. Tn6: Simulation performance report. Technical report, ESA Contract Number No: 22868/09/NL/AT, 2010.

[42] P. Luo and M.G. Petovello. Collaborative acquisition of weak gps signals. In *Position Location and Navigation Symposium (PLANS), 2010 IEEE/ION*, pages 787–795, 2010.

[43] M.D. Macleod. Joint detection and high resolution ml estimation of multiple sinusoids in noise. In *Acoustics, Speech, and Signal Processing, 2001. Proceedings. (ICASSP '01). 2001 IEEE International Conference on*, volume 5, pages 3065–3068 vol.5, 2001.

[44] M. Marey, O.A. Dobre, and R. Inkol. Classification of space-time block codes based on second-order cyclostationarity with transmission impairments. *Wireless Communications, IEEE Transactions on*, 11(7):2574–2584, 2012.

[45] D. Margaria, L. Lo Presti, N. Kassabian, and J. Samson. A new peer-to-peer aided acquisition approach exploiting c/no aiding. In *Satellite Navigation Technologies and European Workshop on GNSS Signals and Signal Processing (NAVITEC), 2010 5th ESA Workshop on*, pages 1–10, 2010.

[46] L.M. Marti. *Global Positioning System Interference and Satellite Anomalous Event Monitor*. PhD thesis, Ohio University, 2004.

[47] L. Musumeci and F. Dovis. A comparison of transformed-domain techniques for pulsed interference removal on gnss signals. In *Localization and GNSS (ICL-GNSS), 2012 International Conference on*, pages 1–6, June 2012.

[48] N. O'Mahony, C. O'Driscoll, and C.C. Murphy. Performance of sequential probability ratio test for gps acquisition. In *Communications, 2009. ICC '09. IEEE International Conference on*, pages 1–6, 2009.

[49] A. Polydoros and C.L. Weber. A unified approach to serial search spread-spectrum code acquisition–part i: General theory. *Communications, IEEE Transactions on*, 32(5):542–549, 1984.

[50] A. Polydoros and C.L. Weber. A unified approach to serial search spread-spectrum code acquisition–part i: Part ii: A matched-filter receiver. *Communications, IEEE Transactions on*, 32(5):550–560, 1984.

[51] J. Rissanen. Modeling by shortest data description. *Automatica*, 14(5):465 – 471, 1978.

[52] G. Roberts, A.M. Zoubir, and B. Boashash. Non-stationary gaussian signal classification. In *TENCON '96. Proceedings., 1996 IEEE TENCON. Digital Signal Processing Applications*, volume 2, pages 526–529 vol.2, 1996.

[53] G. Schwarz. Estimating the dimension of a model. *The Annals of Statistics*, 6(2):461 – 464, 1978.

[54] K. Sheridan, Y. Ying, and T. Whitworth. Pre- and post- correlation interference detection within software defined radio. In *25th International Technical Meeting of The Satellite Division of the Institute of Navigation (ION GNSS 2012), Proceedings of*, pages 3542–3548, 2012.

[55] N.C. Shivaramaiah, A.G. Dempster, and C. Rizos. Application of mixed-radix fft algorithms in multi-band gnss signal acquisition engines. *Journal of Global Positioning Systems*, 8:174–186, 2009.

[56] C.L. Spillard, S.M. Spangenberg, and G. J R Povey. A serial-parallel fft correlator for pn code acquisition from leo satellites. In *Spread Spectrum Techniques and Applications, 1998. Proceedings., 1998 IEEE 5th International Symposium on*, volume 2, pages 446–448 vol.2, 1998.

[57] M.K. Sust, R.F. Kaufmann, F. Molitor, and G.A. Bjornstrom. Rapid acquisition concept for voice activated cdma communication. In *Global Telecommunications Conference, 1990, and Exhibition. 'Communications: Connecting the Future', GLOBECOM '90., IEEE*, pages 1820–1826 vol.3, 1990.

[58] T.H. Ta, M. Pini, and L. Lo Presti. Generalized differential signal processing for combined l1 l2c acquisition. In *ION GNSS 2010 conference*, page 3080–3089, 09/2010 2010.

[59] R.J.R. Thompson, E. Cetin, and A.G. Dempster. Influence of gps satellites cross-correlation on the tdoa measurements within the gnss environmental monitoring system (gems). In *International Global Navigation Satellite Systems Society IGNSS Symposium 2011, Proceedings of*, 2011.

[60] M. Trinkle, E. Cetin, R.J.R. Thompson, and A.G. Dempster. Interference localisation within the gnss environmental monitoring

system (gems) - initial field test results. In *25th International Technical Meeting of The Satellite Division of the Institute of Navigation (ION GNSS 2012), Proceedings of*, pages 2930–2939, 2012.

[61] A. Tyrrell, G. Auer, and C. Bettstetter. Fireflies as role models for synchronization in ad hoc networks. In *Bio-Inspired Models of Network, Information and Computing Systems, 2006. 1st*, pages 1–7, 2006.

[62] A. Tyrrell, G. Auer, and C. Bettstetter. On the accuracy of firefly synchronization with delays. In *Applied Sciences on Biomedical and Communication Technologies, 2008. ISABEL '08. First International Symposium on*, pages 1–5, 2008.

[63] F.S.T. Van Diggelen. *A-GPS: Assisted GPS, GNSS, and SBAS*. GNSS technology and applications series. Artech House, 2009.

[64] H.L. Van Trees. *Detection, Estimation, and Modulation Theory*. Number pt. 1 in Detection, Estimation, and Modulation Theory. Wiley, 2004.

[65] A.J. Viterbi. *CDMA: Principles of Spread Spectrum Communication*. Addison-Wesley Wireless Communications Series. Addison Wesley Publishing Company Incorporated, 1995.

[66] L.C. Zhao, P.R. Krishnaiah, and Z.D. Bai. On detection of the number of signals in presence of white noise. *Journal of Multivariate Analysis*, 20(1):1 – 25, 1986.

ACKNOWLEDGMENTS

Questa tesi segna la conclusione di un percorso durato quattro anni, durante i quali ho avuto l'onore e il piacere di lavorare, vivere e condividere il mio tempo con persone per me molto importanti. È quindi un piacere citare e ringraziare queste persone, che mi hanno accompagnato e che hanno contribuito a farmi diventare quello che sono oggi.

Primo tra tutti, devo ringraziare Giovanni, che è stato una guida fissa durante questo periodo, e che è stato per me un esempio di professionalità e di dedizione, di carisma e di coraggio. Lo ringrazio per avermi accolto nel suo gruppo e per avermi dato l'opportunità di fare un percorso a volte tanto difficile per me, quanto interessante.

Restando a Bologna, devo ringraziare tutti i miei colleghi del gruppo Digicomm, passati e presenti, con i quali ho condiviso i momenti faticosi e le tante soddisfazioni. Anche se alcuni di loro hanno preso una strada che li ha portati lontani da me, l'amicizia che si è creata resta intatta. Ringrazio quindi Claudio, Alberto, Chicco, Lina, Vale, Ale, Valeria, Francesco, Roberta, Stefano e Sergio.

A special thanks goes to Prof. Dempster and to Dr. Ediz Cetin, who hosted me at the University of New South Wales, Sydney. It has been really an honor to work with them, and it has been a wonderful opportunity of growth.

Infine devo ringraziare tutte quelle persone che hanno contribuito a dare un valore a quello che ho fatto e faccio ogni giorno, quelle persone con cui ho condiviso tanto e che mi hanno reso la persona che sono oggi. Ringrazio gli amici, vecchi e nuovi, per il supporto che mi hanno sempre dato, per il conforto nei momenti difficili, per il confronto di fronte alle immense domande della vita. Ringrazio una persona veramente speciale per me, Francesca. La ringrazio per la sua dolcezza e per la sua vivacità, per la sua voglia di sognare e di far sognare, per la sua comprensione e per la sua pazienza. Infine, ringrazio i miei genitori, che hanno sempre creduto in me, che mi hanno sempre supportato e sostenuto, li ringrazio per la loro semplicità e per il loro affetto.

Grazie a tutti ...